

**CHARACTERIZATION OF PLANAR  
GLASS WAVEGUIDES  
BY  $K^+ - Na^+$  ION-EXCHANGE**

**by  
Peter C. Noutsios, B.Eng.(Hon.)**

Department of Electrical Engineering  
McGill University  
Montreal, Quebec  
July 1990

A Thesis submitted to the Faculty of Graduate Studies and  
Research in partial fulfillment of the requirements for the  
degree of Master of Engineering

© Peter C. Noutsios 1990

## Abstract

Planar optical waveguides made by purely thermal and electric field-assisted  $K^+ - Na^+$  ion-exchange in soda-lime glass substrates are investigated.

Buried waveguides fabricated by a purely thermal backdiffusion process have been demonstrated, for the first time, on soda-lime glass. The diffusion properties, such as the potassium-ion concentration, are determined experimentally using a scanning electron microscope (SEM) and electron probe microanalyzer (EPMA). These properties are then compared to the numerical modeling of the non-linear ion-exchange process and correlated to the waveguide propagation characteristics, such as the refractive index profile. The single-mode dispersion curves are computed by a simple Runge-Kutta procedure and compared to the measured effective mode indices.

An experimental characterization of surface waveguides made by an electric field-assisted process with respect to a wide range of fabrication conditions are studied, including measurements of polarization-dependent propagation characteristics. Parallel to this, the diffusion properties are numerically simulated and correlated to the SEM data, providing an accurate description of the refractive index profile.

## Resumé

La fabrication de guides optiques planaires par un échange thermal et assisté d'un champ électrique d'ions potassium-sodium dans un substrat de verre soda-calcique est étudiée.

La fabrication par échange-arrière thermal de guides optiques ensevelis dans un verre soda-calcique a été démontrée pour la première fois. Les propriétés diffusives, comme la concentration d'ions potassium, sont déterminées expérimentalement en utilisant un microscope électronique balayant (SEM) et un micro-analyseur à sonde électronique (EPMA). Ces propriétés sont comparées avec le modelage numérique des équations non-linéaires de diffusion décrivant l'échange d'ions et sont mises en corrélation avec les caractéristiques de propagation, comme le profil d'indice. Les courbes de dispersion de guides monomodes ont été analysés à l'aide d'un modèle simple Runge-Kutta et sont comparés avec les indices mesurés.

On a effectué une caractérisation expérimentale des guides fabriqués par un échange assisté d'un champ électrique dans une gamme de conditions de fabrication, incluant des mesures de caractéristiques de propagation dépendants de la polarisation. Parallèlement, les propriétés diffusives ont été résolues numériquement et comparées avec les données du SEM pour fournir une description précise du profil d'indice.

## ACKNOWLEDGEMENTS

I would like to thank my supervisor, Professor Gar Lam Yip, for his guidance and encouragement during the course of my studies and also for his thorough revision of the first draft of this thesis. Our many stimulating discussions about research, politics, ethics, and personal relationships have inspired me and provided plenty of food for thought.

I am also very grateful to Dr. Kiyoshi Kishioka, now with Osaka Electro Communication University, Japan, for his technical expertise in the experimental work described in this thesis. His encouragement and brotherly advice has given me great inspiration in the pursuit of my academic endeavors. In addition, thank Dr. Nobuo Goto, now with Toyohashi University, Japan, for his help and many fruitful discussions about integrated optics technology.

I also have greatly benefited from the technical assistance of Helen Campbell and Moyra McKinnon of the Department of Mining and Metallurgical Engineering for the SEM and EPMA analysis, respectively. In addition, I thank Diane Pilley for her suggestions in the polishing stages. The guidance of John Foldvari of the Electrical Engineering Workshop is also acknowledged in the construction of the electric field-assisted ion-exchange apparatus.

I must express my gratitude to my fellow colleagues for their many stimulating discussions. In particular, the contributions from John Nikolopoulos, Arthur Vartanian, Michael Sekerka-Bajbus, now with the Canadian Armed Forces, Feng Xiang, Jian-Yao Chen, Jacques Albert, now working at the Communication Research Center, and Michel Bélanger, presently at the National Institute of Optics, are acknowledged.

This research was supported financially by the Natural Sciences and Engineering Research Council of Canada (NSERC) through a post-graduate scholarship, an operating grant, and a strategic grant.

*To my parents, Costas and Calliope,  
and my sister, Helen,  
with love, gratitude, and admiration*

# Contents

<b>1</b>	<b>Introduction</b>	<b>1</b>
1.1	Historical overview and motivation . . . . .	1
1.2	Ion-exchange technology . . . . .	2
1.3	Methodology of the characterization . . . . .	4
1.4	Original contributions . . . . .	5
<b>2</b>	<b>Ion-exchange Theory and Modeling</b>	<b>6</b>
2.1	Introduction . . . . .	6
2.1.1	Glass structure . . . . .	6
2.1.2	Ion-exchange kinetics . . . . .	7
2.2	Derivation of the ion-exchange equations . . . . .	8
2.3	Solutions of the purely thermal ion-exchange equation . . . . .	12
2.3.1	Initial and boundary conditions . . . . .	12
2.3.2	Numerical solutions . . . . .	14
2.3.3	The backdiffusion process . . . . .	18
2.4	Solutions of the field-assisted ion-exchange equation . . . . .	20
2.4.1	Approximate analytical solutions . . . . .	20
2.4.2	Accurate numerical solutions . . . . .	23
2.5	Appendix 2A . . . . .	25
2.6	Appendix 2B . . . . .	26
<b>3</b>	<b>Waveguide modeling and design</b>	<b>33</b>

3.1	Introduction . . . . .	33
3.2	Basic principles . . . . .	33
3.2.1	Planar structure . . . . .	33
3.2.2	Scalar wave equations . . . . .	34
3.2.3	Exact solutions for step-index profiles . . . . .	35
3.2.4	Approximate solutions for graded-index profiles . . . . .	36
3.3	Numerical solutions of the scalar Helmholtz equation . . . . .	37
3.3.1	Background . . . . .	37
3.3.2	Computation of the effective mode indices . . . . .	38
3.3.3	$TE_0$ and $TM_0$ modal fields . . . . .	39
3.3.4	Numerical methodology . . . . .	40
3.4	Design of single and multi-mode waveguides . . . . .	41
3.4.1	Introduction . . . . .	41
3.4.2	Step-index profiles . . . . .	42
3.4.3	Graded-index profiles . . . . .	42
3.5	Appendix 3A . . . . .	41
<b>4</b>	<b>Fabrication and Measurement</b>	<b>46</b>
4.1	Introduction . . . . .	46
4.2	Purely thermal waveguide fabrication . . . . .	46
4.2.1	Preliminary considerations . . . . .	46
4.2.2	Substrate cleaning . . . . .	47
4.2.3	The ion-exchange environment . . . . .	48
4.2.4	Fabrication procedures . . . . .	49
4.3	Electric field-assisted waveguide fabrication . . . . .	49
4.3.1	Experimental setup . . . . .	49
4.4	Fabrication procedures . . . . .	51
4.5	Ion concentration measurement . . . . .	53

4.5.1	Introduction . . . . .	53
4.5.2	Waveguide preparation . . . . .	53
4.5.3	Scanning electron microscopy (SEM) . . . . .	54
4.5.4	Electron probe microanalysis (EPMA) . . . . .	55
4.6	Measurement of propagation characteristics . . . . .	56
4.6.1	Preliminary considerations . . . . .	56
4.6.2	Modal spectroscopy . . . . .	56
4.6.3	Propagation loss . . . . .	57
<b>5</b>	<b>Purely thermal buried waveguide characterization</b>	<b>68</b>
5.1	Introduction . . . . .	68
5.2	SEM and EPMA results . . . . .	69
5.3	Diffusion characteristics . . . . .	70
5.4	Curve fitting . . . . .	71
5.5	Dispersion curves and modal fields . . . . .	72
5.6	Single-mode design . . . . .	74
5.7	Propagation losses . . . . .	75
<b>6</b>	<b>Field-assisted surface waveguide characterization</b>	<b>89</b>
6.1	Introduction . . . . .	89
6.2	Propagation characteristics . . . . .	89
6.2.1	Background . . . . .	89
6.2.2	Experimental observations . . . . .	91
6.2.3	Data reduction and dispersion curves . . . . .	91
6.2.4	Modeling $(E_a^T, t)$ vs $(\Delta n_s, d, a)$ . . . . .	94
6.2.5	Number of guided modes . . . . .	95
6.2.6	Discussion of errors . . . . .	96
6.3	Diffusion characteristics . . . . .	96
6.3.1	Introduction . . . . .	96

6.3.2	Determination of $\alpha$ . . . . .	97
6.3.3	Ionic current-time variation . . . . .	98
6.3.4	Concentration profiles . . . . .	99
<b>7</b>	<b>Discussion and conclusion</b>	<b>114</b>

# List of Figures

2.1	Structure of a typical soda-lime glass (see [24]) . . . . .	28
2.2	Diagram showing the ion-exchange process for (a) purely thermal exchange (b) field-assisted exchange . . . . .	29
2.3	Computational grid for the numerical solution . . . . .	30
2.4	Numerical solution for a purely thermal surface waveguide . . . . .	31
2.5	Numerical solution for a purely thermal buried waveguide . . . . .	31
2.6	Analytical solution for a constant electric field-assisted surface guide . . . . .	32
2.7	Numerical solution for a constant electric field-assisted surface guide . . . . .	32
3.1	Planar waveguide structure . . . . .	45
3.2	Step-index waveguide profile . . . . .	45
4.1	Diagram showing (a) half-cell configuration and (b) Teflon seals . . . . .	60
4.2	Complete electrode configuration . . . . .	61
4.3	Schematic of (a) T-section and (b) wire levels . . . . .	62
4.4	Schematic of the electric field-assisted apparatus . . . . .	63
4.5	Electric field-assisted diffusion process . . . . .	64
4.6	Diagram showing SEM method used to determine potassium concentration profile in ion-exchanged waveguides . . . . .	65
4.7	Experimental setup for measuring the effective mode indices . . . . .	66
4.8	Photograph of the m-lines from a multi-mode waveguide . . . . .	66
4.9	Prism position measurement for measuring the propagation losses . . . . .	67
4.10	Experimental setup for measuring the propagation losses . . . . .	67

5.1	SEM photographs of (a) surface waveguide (10,000 $\times$ ), $t_1 = 2.0$ hr , $T_1 = 360^\circ C$ and (b) buried waveguide (5000 $\times$ ), $t_1 = 2.0$ hr., $T_1 =$ $360^\circ C$ , $t_2 = 0.5$ hr., $T_2 = 440^\circ C$ . . . . .	77
5.2	Comparison of the numerical solution to the scaled SEM data of the buried guide in Fig. 5.1(b) . . . . .	78
5.3	Comparison of the numerical simulation of the diffusion equation to the measured mode indices using $\hat{\alpha} = 0.898$ at $T = 440^\circ C$ . . . . .	79
5.4	Square root dependence of $x_{peak}$ with $t_2$ for $t_1 = 2$ and 4 hr. . . . .	80
5.5	Variation of $n_{peak}$ vs. $t_2$ for $t_1 = 2$ and 4 hr . . . . .	80
5.6	Rayleigh profile fitted to the numerical simulation of diffusion equa- tion with superimposed SEM data for ( $t_1 = 2$ hr . $t_2 = 30$ min.) . . . . .	81
5.7	Plot of (a) $A$ and (b) $\gamma$ vs. $t_2$ for $t_1 = 2$ and 4 hr . . . . .	82
5.8	Theoretical dispersion curves (WKB and exact) of the guided modes compared with measured indices for samples prepared at $T = 360^\circ C$ for a Gaussian profile (times in hrs.) (a) $TE_0$ (b) $TM_0$ . . . . .	83
5.9	Theoretical dispersion curves (Rayleigh profile) of the guided $TE_0$ and $TM_0$ modes compared with measured indices for (a) $t_1 = 2$ hr (b) $t_1 = 4$ hr. . . . .	84
5.10	Plots of normalized field amplitude as a function of $\xi$ for $TE_0$ and $TM_0$ modes for a (a) Gaussian profile ( $\xi = x/d$ ) . ( $t_1 = 4$ hr ) (b) Rayleigh profile ( $\xi = x/x_{peak}$ ) . ( $t_1 = 4$ hr , $t_2 = 15$ min ) . . . . .	85
5.11	Square root dependence of modal field width $W_f$ with $t_2$ . . . . .	86
5.12	SEM photos of microdeformations in $K^+$ -ion exchanged glass sur- faces after backdiffusion in $NaN_3$ ( $t_1 = 4$ hr ) (a) $t_2 = 0$ min. (b) $t_2 = 45$ min . . . . .	88
6.1	Dependence of the shape of the modified Fermi profile on $a$ . . . . .	103

6.2	Theoretical dispersion curves (modified Fermi profile) compared with measured mode indices for waveguides prepared at $E_a = 21.1 V/mm$ (diffusion time in minutes) (a) TE modes (b) TM modes . . . . .	104
6.3	Effective guide depths vs. the diffusion time (applied field in $V/mm$ ) for (a) TE modes (b) TM modes . . . . .	107
6.4	Variation of coefficient $F_e$ with applied field $E_a$ for (a) TE modes and (b) TM modes . . . . .	108
6.5	Comparison of the theoretical dispersion curves of a modified Fermi profile (solid curve) with the step profile (dashed curve) together with the experimental data of Fig. 6.2(a) . . . . .	111
6.6	Typical example of ionic current-time variation . . . . .	112
6.7	SEM photograph of a surface waveguide ( $3500 \times$ ) fabricated at $E_a = 21.1 V/mm$ , $t = 20$ min. and $T = 385^\circ C$ . . . . .	113
6.8	Comparison of the numerical solution to the scaled SEM data of the surface waveguide in Fig. 6.5 . . . . .	113
7.1	A flowchart of the characterization procedure for buried waveguides made by purely thermal migration . . . . .	117
7.2	A flowchart of the characterization procedure for surface waveguides made by electromigration . . . . .	113

# List of Tables

2.1	Chemical composition of a soda-lime substrate . . . . .	28
2.2	Typical values of diffusion parameters yielding numerical stability . .	30
4.1	Bill of materials . . . . .	64
5.1	Quantitative electron microprobe analysis of a soda-lime glass substrate, a surface waveguide, and a buried waveguide . . . . .	78
5.2	Fitting parameters $A$ and $\gamma$ related to $t_2$ . . . . .	81
5.3	Measured TE and TM single mode effective indices . . . . .	86
5.4	Single-mode design parameters . . . . .	87
5.5	$TE_0$ propagation loss measurements ( $t_1 = 4$ hr.) . . . . .	87
6.1	Measured effective TE mode indices . . . . .	101
6.2	Measured effective TM mode indices . . . . .	102
6.3	Calculated TE mode modified Fermi profile parameters . . . . .	105
6.4	Calculated TM mode modified Fermi profile parameters . . . . .	105
6.5	Calculated TE mode step profile parameters . . . . .	106
6.6	Calculated TM mode step profile parameters . . . . .	106
6.7	Measured $\Delta n_s$ and profile parameters for various $E_a$ . . . . .	109
3.8	Diffusion coefficients and depth parameters for various applied fields	109
6.9	Comparison between the calculated and actual number of TE modes	110
6.10	Comparison between the calculated and actual number of TM modes	110
6.11	Comparison of two waveguides fabricated under identical conditions	111
6.12	Mobility measurements and other process parameters . . . . .	112

# Chapter 1

## Introduction

### 1.1 Historical overview and motivation

The rapid development of advanced optical fiber communication systems has established a need for guided wave optical circuits. These circuits are designed to control the various parameters of the lightwave propagating in the fiber. The functional performance of these devices in high speed photonic switching, filtering, modulation and wavelength division (de-)multiplexing would add great benefits to optical communications, signal processing and optical computer applications.

Integrated optics promises to provide such compact active and passive devices integrated on a substrate [1]. In active devices, such as modulators [2] and switches [3], an externally controlled parameter is used to modify the desired function. In passive devices, such as power splitters and directional couplers [4], the function can not be controlled externally. Therefore, the fabrication process control and characterization of passive waveguide devices with good reproducibility within specific tolerances is a must [5].

In order to apply integrated optical circuits to fiber communication systems, one of the most important challenges involves the coupling of waveguide channels to glass fibers [6]. This alignment and attachment, known as fiber 'pig-tailing', has received considerable attention for the development of a viable packaging technology. This is crucial for the future commercialization of integrated optical devices

in real world instruments and systems [7].

In this thesis, we will focus our attention on the characterization of optical waveguides made by a planar technology in glass. This is necessary in the design and fabrication of passive devices optimized for efficient coupling with optical fibers.

## 1.2 Ion-exchange technology

Glass is an excellent material as a planar substrate in which to fabricate passive waveguides. Due to its compatibility with optical fibers in material properties, Fresnel losses can be minimized, leading eventually to lower insertion loss [8,9]. It is also an inexpensive, physically stable material under a wide range of processing and operating conditions. More importantly, it is an ideal medium for a simple diffusion process known as ion-exchange.

The ion-exchange technique, which has been used for more than a century to produce tinted and chemically strengthened glass, has received attention as it creates a higher refractive index waveguiding region. The diffusion process is simple and easily amenable to economical batch fabrication on a large scale. Purely thermal and electric field-assisted exchange from a molten ionic bath and a metallic film have led to the fabrication of multimode and single-mode waveguide devices [5]. However, due to the limitation in their information carrying capacity (bandwidth), multimode optical fibers and waveguide devices have been gradually replaced by their single-mode equivalents. Hence, an ion-exchange technology has been developed for this purpose.

The  $K^+ - Na^+$  ion-exchange process has by far been the most used for single-mode device fabrication [5]. This preference is attributed to four main factors

1. The small refractive index change  $\Delta n$ , with a pure  $KNO_3$  melt is highly compatible with single-mode fibers
2. Owing to its small diffusion coefficient, it is a slower process, making it more

controllable. This is important for good reproducibility of devices.

3. It has proven to provide low propagation losses [10] because  $K^+$  ions do not reduce to a metallic form in the glass which are the major cause of scattering and absorption centers [5]. This has occurred for pure  $AgNO_3$  melts, requiring concentration control (dilution) of  $Ag^+$  ions in the melt.
4. Unlike  $Ag^+ - Na^+$  exchange, no concentration control of the melt is necessary thus simplifying the fabrication procedure.

Yip and Albert [11,12,13] have reported an exhaustive study of purely thermal  $K^+ - Na^+$  exchange in soda-lime glass. It includes the determination of the refractive index profile, measurement of the potassium diffusion coefficient and its temperature dependence, the surface index change, and birefringence. Since then, this characterization procedure was repeated by another group to study  $K^+ - Na^+$  exchange in BK7 glass [14].

Although surface waveguides have been characterized using potassium, there has been recent interest in fabricating graded-index planar buried waveguides [5]. There are two main reasons for this. The first is that burying a surface waveguide considerably improves the index profile symmetry so as to match that of an optical fiber. The other is that lower propagation losses are attainable because the guided wave does not interact with the surface irregularities which invariably contribute to losses via scattering. The characterization of such devices is necessary in the design and fabrication of passive devices for efficient coupling with optical fibers to minimize the insertion loss [8].

The electric field-assisted ion-exchange process is a valuable technology for integrated optics. It has been shown to have advantages over the purely thermal exchange for many reasons. Firstly, the application of an electric field across the substrate during ion-exchange considerably speeds up the diffusion time needed to fabricate single and multimode waveguides [15,16]. This is valuable for the rather

slow process of purely thermal  $K^+ - Na^+$  exchange. In addition, the shape of the index profile can be made more step-like for both planar and channel waveguides [16]. This is advantageous in transforming the elliptical two-dimensional index profile of purely thermal channel waveguides to a more desirable rectangular shape. Such a profile improves the confinement of the optical fields in waveguide devices and hence, reduces device cross-talk. Finally, this process can be applied in the fabrication of deep, buried waveguides with the electric field enhancing the backdiffusion process [9].

When this work was undertaken, the  $K^+$ -ion buried waveguide fabrication remained to be demonstrated. Since then, buried waveguides using electric field-assisted  $K^+$ -ion exchange have led to low loss buried channel waveguides [9]. However, a detailed characterization of this process was still lacking. In addition, buried waveguides without an applied field were not demonstrated. Attempts to bury the waveguides by purely thermal exchange were not successful [17]. These two challenges provided motivation for the undertaking of this work.

### 1.3 Methodology of the characterization

The objective of a planar waveguide characterization is to establish a correlation between the propagation characteristics and the ion-exchange process. A systematic study entails these following ideas which are described in detail in the subsequent chapters:

1. Analysis of the ion-exchange equation with appropriate initial and boundary conditions to predict the diffusion properties, such as the dopant concentration profile, for given fabrication conditions (see Chapter 2).
2. Determination of a simple analytical function  $f(x)$  to express the concentration (refractive index) profile accurately. This will simplify its use in the design stages of integrated optical devices which use buried and surface waveg-

guides as basic structures (see Chapters 5 and 6).

3. Calculating the waveguide propagation characteristics such as the effective index, the modal field profile, and subsequent dispersion curves for the given index profile expressed conveniently as  $f(x)$ . In addition, the desired single or multimode design parameters can be chosen (see Chapter 3).
4. Fabrication of the surface and buried waveguides by electric field-assisted and purely thermal backdiffusion, respectively, with given fabrication conditions (see Chapter 4).
5. Measurement of the concentration profile using a scanning electron microscope (SEM) and the effective mode indices using prism coupling with appropriate comparison to theoretical modeling (see Chapters 4,5,6).

## 1.4 Original contributions

The original contributions of this work to the advancement of planar glass waveguide technology are summarized as follows:

- the demonstration of buried planar optical waveguides by a purely thermal backdiffusion  $K^+ - Na^+$  process and the measurement of the  $K^+$ -ion profile using SEM and EPMA [18,19]
- the correlation of the diffusion properties of the backdiffusion process to the single-mode waveguide propagation characteristics (dispersion curves and modal field profiles) by theoretical modeling and experimentation [20]
- the detailed characterization of planar electric field-assisted  $K^+$ -ion exchange waveguides in glass including an improved model for the refractive index profile and the diffusion characteristics [21,22]

## Chapter 2

# Ion-exchange Theory and Modeling

### 2.1 Introduction

In this chapter, the theoretical foundations of the ion-exchange process for the purpose of modeling optical waveguide concentration profiles are presented. The analysis is quite specific for the  $K^+ - Na^+$  ion-exchange, however, the underlying methodology is general and can be used for other cation pairs and substrate glass. The analytical and numerical solutions are presented for important ion-exchange simulations used in the design of channel-based integrated optical devices.

#### 2.1.1 Glass structure

A typical soda-lime silicate glass substrate is composed of 71 - 75 % silicon dioxide ( $SiO_2$ ), 12 - 16 % sodium oxide, also known as soda ( $Na_2O$ ), 5 - 15 % calcium oxide, or lime ( $CaO$ ), and minor amounts of various other oxides [23,24] such as  $K_2O$ ,  $Al_2O_3$ , and  $MgO$ . In this characterization, commercially available Fisherbrand microscope slides are used as substrates. Their exact chemical composition is listed in Table 2.1 and the instrument used to determine this composition will be introduced in Chapter 4. It will be shown, in Chapters 5 and 6, that certain fabrication conditions affect this composition quite drastically and lead to important waveguiding properties.

Sodium ( $Na^+$ ) ions (supplied by  $Na_2O$ ) have been found to be easily displaced by other monovalent ions. Figure 2.1 shows a typical chemical structure of a soda-lime glass substrate. The sodium ions fit into the relatively large voids in the silica network and are found close to the negatively charged nonbridging oxygen atoms. They are attracted to these oxygen atoms rather weakly by ionic bonds which are much weaker than the  $Si - O$  bonds within the glass matrix [25]. Consequently, these  $Na^+$  ions are relatively mobile compared to the rigid silica network, and at sufficiently high temperature, can be readily displaced. When new ions, such as potassium, are introduced into the glass from a molten potassium nitrate  $KNO_3$  source, they can occupy the same sites as the sodium ions since the ion-exchange occurs on a one-to-one basis [23]. The qualitative details of this mechanism is presented below

### 2.1.2 Ion-exchange kinetics

When a glass substrate is placed into a molten salt bath (melt) containing another monovalent ion, such as  $K^+$ ,  $Ag^+$ ,  $Tl^+$  or  $Cs^+$ , ion-exchange takes place. The process occurs as follows. At the glass-melt interface, the abundant dopant  $K^+$  ions in the melt 'see' the glass as a potassium-free medium and hence, are driven into it by a chemical potential diffusion gradient. Simultaneously, the more mobile  $Na^+$  ions are released into the melt with the  $K^+$  ions replacing them by a one-to-one exchange. Actually, there is another force besides the chemical potential at work here. The difference in the mobilities of the two ionic species creates a local charge imbalance that creates an internal electric field which speeds up the slower  $K^+$  ions [23]. This point will be described quantitatively in the next section.

Gradually, the potassium ions diffuse away from the interface and slowly inhabit a very thin layer near the surface. The resulting  $K^+$ -ion concentration profile has a maximum at the surface and decreases monotonically inside the substrate. In this thin region, the increased dopant concentration leads to a local increase in

the refractive index. This optically dense thin film can be used as a waveguiding medium where the light can travel longitudinally by total internal reflection. The exact relation between the ion concentration and the index change is quite complicated. However, it is generally believed that they are directly proportional [5] and in this thesis, this assumption is a key point. In Chapters 5 and 6, the propagation characteristics of these waveguides will be discussed in more detail and correlated to the diffusion properties of the ion-exchange process.

## 2.2 Derivation of the ion-exchange equations

As mentioned, it is assumed that the refractive index profiles of these waveguides are directly proportional to the concentration of potassium ions in the glass. This concentration can be simulated by solving the diffusion equation which in general, can include the influence of an applied electric field [26]. Consider the schematic of Fig. 2.2 with only two mobile species,  $K^+$  and  $Na^+$ , both of which are monovalent cations. In the one-dimensional ion-exchange process, there exists two forces that act on the exchanging species. The first is due to the gradient in chemical potential. The other is due to the presence of gradients in electrical potential, one arising intrinsically and the other being applied externally. This statement is based upon the assumption that no other thermodynamic forces, such as gradients in pressure or temperature, are present in the system [27].

The change in the concentration,  $c$ , defined as the number of ions per unit volume, of a given cation is related to the flux of ions  $\vec{J}$  by the equation of continuity

$$\frac{\partial c}{\partial t} = -\vec{\nabla} \cdot \vec{J} = -\frac{\partial J}{\partial x} \quad (2.1)$$

with both  $x$  and  $\vec{J}$  directed horizontally. When the species are diffusing isotropically, the flux obeys Fick's first law of diffusion

$$\vec{J} = -D\vec{\nabla}c = -D\frac{\partial c}{\partial x} \quad (2.2)$$

where  $D$ , the self diffusion coefficient, is dependent upon  $c$  and the fabrication conditions. Substituting (2.2) into (2.1), we get Fick's second law:

$$\frac{\partial c}{\partial t} = \vec{\nabla} \cdot (D \vec{\nabla} c) = \frac{\partial}{\partial x} \left( D \frac{\partial c}{\partial x} \right)$$

which can be solved for  $c$ , given appropriate initial and boundary conditions [28].

Intrinsic electric field,  $E_i$  : Since potassium and sodium ions diffuse at different rates, there is a tendency for  $Na^+$  ions to move faster than  $K^+$  ions, leading to a buildup of electrical charge. There is, however, a gradient in electrical potential along with this charge which acts to slow down the faster  $Na^+$  ions and speed up the slower  $K^+$  ions. Despite the difference in the ion mobilities, the gradient in electrical potential forces the fluxes of the two ions to be equal and opposite (see Fig. 2.2(a)), thus preserving charge neutrality [23]. In this purely thermal exchange, the enriched  $K^+$ -ion waveguiding layer is formed on both sides of the substrate.

Externally applied field,  $E_a$  : When a positive dc electric field is applied along the  $x$ -axis, a positive flux of the ions is created. This field is equal to the quotient of the applied voltage and the substrate thickness. As shown in Fig. 2.2(b), these ions are forced to move in the same direction as the electric field creating a waveguiding layer only on the substrate side facing the positive electrode. To avoid space-charge buildup, the sum of the ionic fluxes produces a net positive ionic flux with magnitude  $J_0$ , which must be a constant function of position [26].

The contribution of the total electric field,  $E_t = E_i + E_a$ , to the flux is determined as follows. Consider the ratio of the speed of the ions to the magnitude of  $E_t$  given by the mobility  $\mu$ ,

$$v_E = \mu E_t \quad (\mu m/min.) \quad (2.3)$$

and, according to the Nernst-Einstein definition, the mobility is related to  $D$  by.

$$\mu = \frac{eD}{kT} \quad (\mu m^2/(V min.)) \quad (2.4)$$

where  $e$  is the elementary charge ( $1.6 \times 10^{-19}$  Coul),  $k$  is the Boltzmann constant ( $1.38 \times 10^{-23}$  J/°K), and  $T$  is the temperature in °K. In most glasses, however, the purely thermal migration process is slightly different from the electric field induced transport and (2.4) is not obeyed [5]. Instead, the relation between  $D$  and  $\mu$  is written as

$$\mu = \frac{eD}{fkT} \quad (2.5)$$

where  $f$  is the correlation factor whose value depends only on the glass composition and varies from 0.2 to 1.0 [29]. Hence, the same  $f$  can be used for both  $K^+$  and  $Na^+$  ions. Then,

$$J_E = cv_E = c \frac{eD}{fkT} E_t \quad (2.6)$$

Using (2.2) and (2.6), the magnitude of total fluxes of the potassium and sodium ions becomes

$$J_K = -D_K \left( \frac{\partial c_K}{\partial x} - \frac{eE_t}{fkT} c_K \right) \quad (2.7)$$

$$J_{Na} = -D_{Na} \left( \frac{\partial c_{Na}}{\partial x} - \frac{eE_t}{fkT} c_{Na} \right), \quad (2.8)$$

respectively. As mentioned, the net flux,  $\vec{J}_o$ , must be constant across the substrate to maintain the neutrality of the glass. Hence,

$$\vec{J}_{Na} + \vec{J}_K = \vec{J}_o = \frac{I}{F} \quad (2.9)$$

where  $I$  is the measured ion current density ( $mA/mm^2$ ) and  $F$  is Faraday's constant or 96500 Coul/mole. Also,

$$c_K + c_{Na} = c_o = \text{constant}$$

The constant  $c_o$  is the concentration of  $Na^+$  ions present in the glass prior to the exchange. Since  $K^+$  ions replace  $Na^+$  ions on a one-to-one basis, the total ion concentration remains equal to  $c_o$ . Defining  $\hat{c}_K = c_K/c_o$ ,  $\hat{c}_{Na} = c_{Na}/c_o = 1 - \hat{c}_K$ , then

$$\frac{\partial \hat{c}_K}{\partial x} = -\frac{\partial \hat{c}_{Na}}{\partial x}.$$

Substituting (2.7) and (2.8) into (2.9), we get

$$J_o = c_o \left\{ \frac{eD_K}{fkT} \hat{c}_K E_t - D_K \frac{\partial \hat{c}_K}{\partial x} - D_{Na} \frac{\partial \hat{c}_{Na}}{\partial x} + \frac{eD_{Na}}{fkT} \hat{c}_{Na} E_t \right\} \quad (2.10)$$

After a few manipulations,

$$\frac{J_o}{c_o D_{Na}} = \frac{eE_t}{fkT} \left[ 1 - \left( 1 - \frac{D_K}{D_{Na}} \right) \hat{c}_K \right] + \left( 1 - \frac{D_K}{D_{Na}} \right) \frac{\partial \hat{c}_K}{\partial x}$$

and upon letting  $\alpha = 1 - D_K/D_{Na} = 1 - \mu_K/\mu_{Na}$ , one obtains the expression for the total electric field

$$E_t = E_a + E_i = \frac{fkT}{e} \left\{ \frac{J_o}{c_o D_{Na} (1 - \alpha \hat{c}_K)} - \frac{\alpha}{1 - \alpha \hat{c}_K} \frac{\partial \hat{c}_K}{\partial x} \right\} \quad (2.11)$$

The externally applied field  $E_a$  is

$$E_a = \frac{J_o}{c_o \mu_{Na} (1 - \alpha \hat{c}_K)} \quad (2.12)$$

using the mobility equation (2.5) for sodium ions. Note that the total field (2.11) depends on the total flux density  $J_o$ , the concentration  $c_o$  and the gradient in chemical potential. This expression explicitly shows that when there is no externally applied field (i.e. the net flux  $J_o = 0$ ), only the intrinsic field is still present. As mentioned earlier, this field arises naturally due to the unequal diffusion rates of the ionic species ( $\alpha \neq 0$ ) and, in particular for the  $K^+ - Na^+$  exchange,  $E_t$  depends on  $\alpha$

Using the equation of continuity (2.1) and substituting (2.7) yields

$$\begin{aligned} \frac{\partial \hat{c}_K}{\partial t} + \bar{\nabla} \cdot (\mu_K \hat{c}_K \bar{E}_t - D_K \bar{\nabla} \hat{c}_K) &= 0 \\ \frac{\partial \hat{c}_K}{\partial t} + \mu_K \left( \hat{c}_K \frac{\partial E_t}{\partial x} + E_t \frac{\partial \hat{c}_K}{\partial x} \right) &= D_K \frac{\partial^2 \hat{c}_K}{\partial x^2} \end{aligned} \quad (2.13)$$

Taking the divergence of the electric field (2.11),

$$\frac{\partial E_t}{\partial x} = \frac{fkT}{e} \left\{ \frac{-\alpha^2}{(1 - \alpha \hat{c}_K)^2} \left( \frac{\partial \hat{c}_K}{\partial x} \right)^2 - \frac{\alpha J_o}{c_o D_{Na} (1 - \alpha \hat{c}_K)^2} \frac{\partial \hat{c}_K}{\partial x} - \frac{\alpha}{1 - \alpha \hat{c}_K} \frac{\partial^2 \hat{c}_K}{\partial x^2} \right\}$$

and one obtains, after a few manipulations with (2.13) that,

$$\frac{\partial \hat{c}_K}{\partial t} = \frac{D_K}{1 - \alpha \hat{c}_K} \left\{ \frac{\partial^2 \hat{c}_K}{\partial x^2} + \frac{\alpha}{1 - \alpha \hat{c}_K} \left( \frac{\partial \hat{c}_K}{\partial x} \right)^2 - \frac{J_o}{c_o D_{Na} (1 - \alpha \hat{c}_K)} \frac{\partial \hat{c}_K}{\partial x} \right\}$$

Now, since

$$\frac{D_K}{1 - \alpha \hat{c}_K} \left( \frac{\partial^2 \hat{c}_K}{\partial x^2} + \frac{\alpha}{(1 - \alpha \hat{c}_K)} \left( \frac{\partial \hat{c}_K}{\partial x} \right)^2 \right) = \frac{\partial}{\partial x} \left( \frac{D_K}{1 - \alpha \hat{c}_K} \frac{\partial \hat{c}_K}{\partial x} \right) \quad (2.14)$$

then the nonlinear partial differential equation describing the general ion-exchange process is

$$\frac{\partial \hat{c}_K}{\partial t} = \frac{\partial}{\partial x} \left( \frac{D_K}{1 - \alpha \hat{c}_K} \frac{\partial \hat{c}_K}{\partial x} \right) - \frac{(1 - \alpha) J_o}{c_o (1 - \alpha \hat{c}_K)^2} \frac{\partial \hat{c}_K}{\partial x} \quad (2.15)$$

An alternative expression for this equation can be deduced by incorporating (2.12), so that it becomes independent of the current density  $J_o$ :

$$\frac{\partial \hat{c}_K}{\partial t} = \frac{\partial}{\partial x} \left( \frac{D_K}{1 - \alpha \hat{c}_K} \frac{\partial \hat{c}_K}{\partial x} \right) - \frac{\mu_K E_a}{(1 - \alpha \hat{c}_K)} \frac{\partial \hat{c}_K}{\partial x} \quad (2.16)$$

For constant electric field-assisted ion-exchange, this differential equation becomes more practical than (2.15) because it makes use of the given fabrication conditions and diffusion coefficients (e.g.  $E_a$ ,  $D_K$ , and  $\mu_K$ ) directly. In contrast, (2.15) needs the values of  $J_o$  which can be used directly for the case of constant current field-assisted exchange [30]. If one were to use (2.15) to model the constant electric field-assisted exchange, then *in situ* measurements of  $J_o$  would be needed during the process.

The ion-exchange equation for purely thermal  $K^+$ -ion exchange can be deduced from (2.15) when the total net flux  $J_o = 0$ , (or (2.16) with  $E_a = 0$ ) so that

$$\frac{\partial \hat{c}_K}{\partial t} = \frac{\partial}{\partial x} \left( \frac{D_K}{1 - \alpha \hat{c}_K} \frac{\partial \hat{c}_K}{\partial x} \right) \quad (2.17)$$

## 2.3 Solutions of the purely thermal ion-exchange equation

### 2.3.1 Initial and boundary conditions

The nonlinear partial differential equation of (2.17) is second order in the spatial variable  $x$  and first order in the time variable  $t$ . Hence, it requires two boundary conditions in  $x$  and an initial condition in  $t$  to be solved uniquely. At time  $t = 0$

there are no dopant  $K^+$  ions in the glass and hence, the concentration vanishes:

$$\hat{c}_K(x, 0) = 0. \quad (2.18)$$

For the boundary conditions, a zero concentration at infinity (i.e. far into the substrate to the right) is expected, while at the surface a constant value of concentration represents the effect of the  $KNO_3$  melt providing  $K^+$  ions for ion-exchange. It was observed that for  $K^+ - Na^+$  exchange, the maximum concentration of the exchanged ions is about 90% of the total concentration of available  $Na^+$  sites [31,32], so that

$$\begin{aligned} \hat{c}_K(0, t) &= c_K(0, t)/c_o = c_l = 0.9 \\ \hat{c}_K(\infty, t) &= c_r = 0. \end{aligned} \quad (2.19)$$

Note that with  $c_o = c_{Na}(G, 0)$ , one boundary condition becomes

$$c_K(0, t) = c_l c_{Na}(0, 0). \quad (2.20)$$

Since there are negligible amounts of  $K^+$  ions in the substrate prior to exchange, then  $c_K(0, 0) = 0$ . Hence, (2.20) is valid only for  $t > 0$  and it takes a negligible amount of time (in comparison to the total diffusion time) to reach its final equilibrium value.

With these conditions, it is convenient to renormalize  $\hat{c}_K$  so that  $c = \hat{c}_K/c_l$  and the boundary conditions become

$$c(0, t) = 1, \quad c(\infty, t) = 0.$$

Hence, (2.17) becomes

$$\frac{\partial c}{\partial t} = \frac{\partial}{\partial x} \left( \frac{D_K}{1 - \hat{\alpha}c} \frac{\partial c}{\partial x} \right) \quad (2.21)$$

with  $\hat{\alpha} = \alpha c_l$ .

### 2.3.2 Numerical solutions

In the past, there have been several attempts to obtain the solution of (2.21) by analytical and numerical methods. Crank obtained a parametric solution after reducing it to an ordinary differential equation [33]. Wood used the result of this solution in a convenient power series expression [34]. For the numerical solutions, Walker *et al.* [35] used an explicit finite difference scheme (FDS) to solve a two dimensional version of (2.21). More recently, Albert and Yip used an implicit FDS with unconditional stability for the particular case of planar  $K^+ - Na^+$  exchange [12]. This solution involved a Boltzmann transformation

$$y = \frac{x}{2\sqrt{D_K t}}$$

which brings (2.21) to the form:

$$-2y \frac{dc}{dy} = \frac{d}{dy} \left( \frac{1}{1 - \hat{\alpha}c} \frac{dc}{dy} \right).$$

This transformation can be effective only when the initial condition  $c(x, 0) = 0$  and one boundary condition  $c(\infty, t) = 0$  are equal. This is because the value of  $y \rightarrow \infty$  for  $t = 0$  and  $x \rightarrow \infty$ , so that  $c(y \rightarrow \infty) = 0$  consolidates the same initial and boundary conditions [36]. This consolidation of the conditions severely restricts its use, especially for the simulations with non-zero initial concentration profiles, such as in backdiffusion. Hence, this transformation was not pursued here and instead, the numerical FDS was examined more carefully.

The numerical solution of (2.21) is based on replacing the partial derivatives in  $x$  and  $t$  by finite differences. The region to be analyzed is spanned by a rectilinear grid with sides parallel to the  $x$  and  $t$  axes. The grid spacings  $h$  and  $k$  are in the  $x$  and  $t$  directions, respectively. The grid points  $(X, T)$  are given by  $X = mh, T = nk$ , with  $m$  and  $n$  being integers and with  $m = n = 0$  being the origin, as shown in Fig. 2.3. The concentration values satisfying the finite difference equation at the grid points are denoted by  $U_m^n$ . It is important to note that the grid spacing must be chosen to yield sufficiently high resolution in the domain of interest.

The parabolic ion-exchange equation can be solved numerically by using an implicit three time-level FDS [37]. It was chosen because of its numerical stability for a wide range of operating parameters. Note that stability means that errors made at one stage of the calculations do not cause increasingly large errors as the computations are continued. This implicit method promises to provide unconditional stability. Defining

$$a(u) = \frac{D_K}{1 - \hat{\alpha}u}$$

the partial differential equation that must be solved becomes:

$$\frac{\partial u}{\partial t} = \frac{\partial}{\partial x} \left( a(u) \frac{\partial u}{\partial x} \right), \quad a(u) > 0. \quad (2.22)$$

The finite differences corresponding to the partial derivatives are presented below:

$$\begin{aligned} \frac{\partial u}{\partial t} &= \frac{(U_m^{n+1} - U_m^{n-1})}{2k} \\ \frac{\partial}{\partial x} \left( a(u) \frac{\partial u}{\partial x} \right) &= \frac{1}{h^2} \delta_x (a(U_m^n) \delta_x U_m^n) \end{aligned}$$

with

$$\delta_x U_m^n = U_{m+1/2}^n - U_{m-1/2}^n.$$

The term,  $\delta_x$ , is the common central difference operator [37] and can be used to express the second order partial derivatives of (2.22). Thus,

$$\begin{aligned} \frac{1}{h^2} \delta_x (a(U_m^n) \delta_x U_m^n) &= \frac{1}{h^2} \delta_x [a(U_{m+1/2}^n - U_{m-1/2}^n)] \\ &= \frac{1}{h^2} [a(U_{m+1/2}^n)(U_{m+1}^n - U_m^n) - a(U_{m-1/2}^n)(U_m^n - U_{m-1}^n)] \end{aligned}$$

The elements  $U_{m-1/2}^n = U_m^n - U_{m-1}^n$  and  $U_{m+1/2}^n = U_{m+1}^n - U_m^n$  are defined such so that they can be evaluated at the appropriate grid points of Fig. 2.3. Defining the mesh ratio  $r = k/h^2$ , the FDS becomes

$$U_m^{n+1} - U_m^{n-1} = 2r [a(U_{m+1/2}^n)(U_{m+1}^n - U_m^n) - a(U_{m-1/2}^n)(U_m^n - U_{m-1}^n)] \quad (2.23)$$

Upon replacing the following elements, expressed in three time level form,

$$\begin{aligned} U_{m+1}^n &= \frac{1}{3}(U_{m+1}^{n+1} + U_{m+1}^n + U_{m+1}^{n-1}) \\ U_m^n &= \frac{1}{3}(U_m^{n+1} + U_m^n + U_m^{n-1}) \\ U_{m-1}^n &= \frac{1}{3}(U_{m-1}^{n+1} + U_{m-1}^n + U_{m-1}^{n-1}) \end{aligned}$$

into (2.23), it leads to the formula

$$\begin{aligned} U_m^{n+1} - U_m^{n-1} &= \frac{2r}{3} \left[ \alpha^+ \left\{ (U_{m+1}^{n+1} - U_m^{n+1}) + (U_{m+1}^n - U_m^n) + (U_{m+1}^{n-1} - U_m^{n-1}) \right\} \right. \\ &\quad \left. - \alpha^- \left\{ (U_m^{n+1} - U_{m-1}^{n+1}) + (U_m^n - U_{m-1}^n) + (U_m^{n-1} - U_{m-1}^{n-1}) \right\} \right] \end{aligned} \quad (2.24)$$

where

$$\alpha^+ = a \left( \frac{U_{m+1}^n + U_m^n}{2} \right) = \frac{D_K}{1 - \hat{\alpha}(U_{m+1}^n + U_m^n)/2} \quad (2.25)$$

and

$$\alpha^- = a \left( \frac{U_m^n + U_{m-1}^n}{2} \right) = \frac{D_K}{1 - \hat{\alpha}(U_m^n + U_{m-1}^n)/2} \quad (2.26)$$

The resultant three time-level system of (2.24)-(2.26) can be expressed in a convenient tridiagonal matrix form as:

$$\begin{bmatrix} a_{1,1}^n & a_{1,2}^n & 0 & \cdots & 0 \\ a_{2,1}^n & a_{2,2}^n & a_{2,3}^n & \cdots & 0 \\ 0 & a_{3,2}^n & a_{3,3}^n & \cdots & 0 \\ \vdots & \vdots & \ddots & \vdots & \vdots \\ \vdots & \vdots & \vdots & \ddots & \vdots \\ 0 & 0 & 0 & a_{M1-2,M1-2}^n & a_{M1-2,M1-1}^n \\ 0 & 0 & 0 & a_{M1-1,M1-2}^n & a_{M1-1,M1-1}^n \end{bmatrix} \begin{bmatrix} U_1^{n+1} \\ U_2^{n+1} \\ U_3^{n+1} \\ \vdots \\ \vdots \\ U_{M1-2}^{n+1} \\ U_{M1-1}^{n+1} \end{bmatrix} = \begin{bmatrix} RHS_1 \\ RHS_2 \\ RHS_3 \\ \vdots \\ \vdots \\ RHS_{M1-2} \\ RHS_{M1-1} \end{bmatrix}$$

where the lower-diagonal, diagonal and super-diagonal elements of the matrix can be determined from (2.24) as:

$$\begin{aligned} a_{m,m-1}^n &= -\frac{2r}{3}\alpha^- \\ a_{m,m+1}^n &= -\frac{2r}{3}\alpha^+ \\ a_{m,m}^n &= 1 + \frac{2r}{3}(\alpha^+ + \alpha^-) \end{aligned}$$

The  $RHS_m$  elements are determined from (2.24) as.

$$U_m^{n-1} + \frac{2r}{3} \left[ \alpha^+ \left\{ U_{m-1}^n - U_m^n + U_{m+1}^{n-1} - U_m^{n-1} \right\} - \alpha^- \left\{ U_m^n - U_{m-1}^n + U_m^{n-1} - U_{m-1}^{n-1} \right\} \right]$$

The calculation proceeds as follows: first the column matrix  $U_m^n$  is initialized with zeroes, except at the boundary  $x = 0$  where the values are fixed at  $U_o^n = U_o^{n-1} = U_o^{n+1} = 1.0$ . Note that because of the negligible amounts of  $K^+$  ions in the substrate prior to exchange,  $U_o^o = 0$ . Then, the tridiagonal matrix is inverted [38] at the first time step to determine  $U_m^{n+1}$ . This solution replaces  $U_m^n$  and the process is repeated for another time step until the desired time has been reached. A complete flowchart of the process is shown in Appendix 2A

Due to the nature of this three time-level scheme, the value of the concentration at  $t = k(n = 1)$ ,  $U_m^1$  is needed to solve for the concentration at  $t = 2k(n = 2)$ ,  $U_m^2$ . Since only  $U_m^o$  is known, then a scheme to determine  $U_m^1$  is needed. A simple solution to this problem is to use finite differences expressed for two time-level explicit problems so that

$$\frac{\partial u}{\partial t} = \frac{(U_m^{n+1} - U_m^n)}{k}, \quad \frac{\partial u}{\partial x} = \frac{(U_{m+1}^n - U_{m-1}^n)}{2h} \quad (2.27)$$

and

$$\frac{\partial^2 u}{\partial x^2} = \frac{(U_{m+1}^n - 2U_m^n + U_{m-1}^n)}{h^2}. \quad (2.28)$$

Using the expanded form of (2.22) and the above finite differences,  $U_m^1$  is determined as

$$U_m^1 = U_m^o + rD_K \left\{ \left( \frac{U_{m+1}^o - 2U_m^o + U_{m-1}^o}{1 - \hat{\alpha}U_m^o} \right) + \frac{\hat{\alpha}}{4} \left( \frac{U_{m+1}^o - U_{m-1}^o}{1 - \hat{\alpha}U_m^o} \right)^2 \right\} \quad (2.29)$$

It seems that the three time-level implicit FDS has an advantage over explicit two time-level schemes in the solution of non-linear parabolic problems mainly because of unconditional stability. However, as mentioned by Mitchell, the introduction of a third time level to a nonlinear diffusion problem may cause some trouble [37]. In this work, it was found that the implicit scheme displayed instabilities for high  $\hat{\alpha}$  and  $D_K$  values. This may be due to the fact that the term  $D_K/(1 - \hat{\alpha})$  becomes large as  $\hat{\alpha} \rightarrow 1$  and  $D_K$  increases. To standardize the stability criterion somehow, the program was run for various values of  $\hat{\alpha}$  and  $D_K$  and the best  $r$  val-

ues giving numerical stability are shown in Table 2.2. For all other ranges,  $r = 1/2$  resulted in stable concentration profiles.

An example of the concentration profile obtained for an exchange time  $t_1 = 2$  hours and at temperature  $T_1 = 360^\circ C$  is shown in Fig. 2.4. Note the Gaussian shape [12] with the diffusion depth  $d$  defined at the  $1/e$  point of the profile [11]. As seen from Table 2.2, the mesh ratio  $r \leq 1/2$  gives a numerically stable and accurate profile for these given fabrication conditions. The order of accuracy has been studied extensively by Lees [39] who proved the convergence result to be proportional to  $(h^2 + k^2)$ . The diffusion parameters,  $\hat{\alpha}$  and  $D_K$ , were obtained from a previous characterization of planar  $K^+ - Na^+$  ion-exchange on soda-lime glass [11]. As reported,  $\hat{\alpha} = 0.898$  and the self-diffusion coefficient  $D_K = D_e(TE)/4(1.17)^2 = 0.323 \mu m^2/hr.$  [4]

Finally, since each nonlinear problem has its own particular difficulties, the apparent choice between a two level and a three level method is a difficult one. In this thesis, the implicit scheme promised unconditional stability and was thus chosen to deal with the wide range of operating parameters encountered in purely thermal exchange. Other numerical schemes, such as the two level explicit scheme, were not pursued in this section, however these were explored more carefully for the field-assisted ion-exchange problem (see 2.4.2).

### 2.3.3 The backdiffusion process

As mentioned in Chapter 1, backdiffusion has become an important fabrication process used in the manufacturing of passive waveguide devices. In this technique, the first exchange surface  $K^+$ -ion concentration profile is introduced into a pure melt of  $NaNO_3$  for a diffusion time  $t_2$  and backdiffusion temperature  $T_2$ . The advantage of this process is that a buried layer can be created below the substrate surface thereby allowing for more efficient coupling with optical fibers [5]

To mathematically model this process, it is necessary to modify the initial

and boundary conditions of (2.18) and (2.19), respectively. The first exchange concentration at time  $t_1$  and temperature  $T_1$  is now used as the initial condition for backdiffusion. In addition, since it is assumed that there are no potassium ions in the  $NaNO_3$  melt, the boundary condition is zero at  $x = 0$ . Hence,

$$U_o^{n-1} = U_o^n = U_o^{n+1} = 0.0$$

and  $U_m^o$  is determined from the numerical solution of the first exchange.

Since single-mode waveguides were of main interest, the first exchange waveguides were fabricated such that they propagated the lightwave only in the fundamental mode. Hence,  $T_1$  was kept fixed at  $360^\circ C$  and the diffusion times were chosen as  $t_1 = 2.0$  and  $4.0$  hours. The time  $t_2$  was varied from 2 to 60 minutes and, for reasons described in Chapter 5,  $T_2$  was kept fixed at  $440^\circ C$  [18] with  $\hat{\alpha} = 0.898$ . At this temperature, the coefficient  $D_K = D_c(TE)/4(1.17)^2 = 4.391 \mu m^2/hr$ .

For numerical stability, it was found that for the first exchange time  $t_1$ , the mesh ratio  $r = 1/2$ , but, because of the high value of  $D_K$  encountered in backdiffusion,  $r$  was chosen as 0.06. The modeling was implemented on an IBM AT personal computer using Microsoft Fortran 4.0. The typical computing time for the first-exchange simulation with a 200 point spatial grid is about 20-40 minutes, depending on the exchange time. For backdiffusion, the computing time was longer, about 45-60 minutes, mainly because of the smaller mesh ratio which resulted in a greater number of time iterations. An example of a buried concentration profile is shown in Fig. 2.5. Note the concentration characteristics, such as the location  $x_{peak}$  and the maximum  $n_{peak}$  which can be determined accurately as functions of  $t_1$  and  $t_2$  [20].

## 2.4 Solutions of the field-assisted ion-exchange equation

### 2.4.1 Approximate analytical solutions

The field-assisted ion-exchange concentration profiles can be determined analytically without the need of a finite difference scheme. To find a solution, it is convenient to define the following normalized variables

$$x^* \equiv \frac{\mu_K E_a x}{D_K}, \quad t^* \equiv \frac{(\mu_K E_a)^2 t}{D_K}$$

with the appropriate derivatives being

$$\frac{\partial \hat{c}_K}{\partial x} = \frac{\mu_K E_a}{D_K} \frac{\partial \hat{c}_K}{\partial x^*}, \quad \frac{\partial \hat{c}_K}{\partial t} = \frac{(\mu_K E_a)^2}{D_K} \frac{\partial \hat{c}_K}{\partial t^*}$$

and hence, (2.16) becomes

$$\frac{\partial \hat{c}_K}{\partial t^*} = \frac{\partial}{\partial x^*} \left( \frac{1}{1 - \alpha \hat{c}_K} \frac{\partial \hat{c}_K}{\partial x^*} \right) - \frac{1}{1 - \alpha \hat{c}_K} \frac{\partial \hat{c}_K}{\partial x^*}. \quad (2.30)$$

Spiegler and Coryell were the first researchers to consider the influence of an externally applied electric field on the concentration profiles for the migration of two ionic species in a cation exchange column [40]. They showed that for the exchange of species A with species B,  $c_l = 1$ ,  $c_r = 0$ , and  $M = \mu_A/\mu_B < 1$ , the concentration can be represented by a step function between  $c_l = 1$  and  $c_r = 0$ . This profile is stationary relative to a reference frame moving at velocity  $v_o = J_o/c_o$ , for constant current exchange. For the case of more general boundary conditions where  $0 < c_r < c_l < 1$ , a similar step-like profile will develop with the reference velocity  $v \neq v_o$ . In the subsequent analysis, the existence of a stationary-state profile relative to a moving reference frame is assumed.

For constant electric field exchange, an approximate analytical solution can be deduced following the methodology of Abou-el-Liel for the case of constant current exchange [26]. The existence of such a stationary-state suggests that the space and time variables combine into one variable as

$$\eta = x^* - v^* t^* \quad (2.31)$$

where  $\nu^*$  is a dimensionless constant to be determined from the boundary conditions. Using (2.31), one determines

$$\frac{\partial \hat{c}_K}{\partial x^*} = \frac{d\hat{c}_K}{d\eta} \quad \frac{\partial \hat{c}_K}{\partial t^*} = -\nu^* \frac{d\hat{c}_K}{d\eta}$$

and substituting into (2.30) gives

$$-\nu^* \frac{d\hat{c}_K}{d\eta} = \frac{d}{d\eta} \left\{ \frac{1}{1 - \alpha \hat{c}_K} \frac{d\hat{c}_K}{d\eta} \right\} - \frac{1}{(1 - \alpha \hat{c}_K)} \frac{d\hat{c}_K}{d\eta}$$

Integrating once with respect to  $\eta$  yields

$$-\nu^* \hat{c}_K = \frac{1}{1 - \alpha \hat{c}_K} \frac{d\hat{c}_K}{d\eta} + \frac{1}{\alpha} \ln(1 - \alpha \hat{c}_K) + \kappa \quad (2.32)$$

where  $\kappa$  is an integration constant. Equation (2.32) has two unknowns,  $\kappa$  and  $\nu^*$  which can be determined as follows. Assuming a step-like profile, we expect that, at both  $\hat{c}_K = c_l$  and  $\hat{c}_K = c_r$ , the gradient of the concentration vanishes, so that

$$\frac{\partial \hat{c}_K}{\partial x^*} = \frac{d\hat{c}_K}{d\eta} = 0.$$

Substituting the above conditions into (2.32) and solving simultaneously gives

$$\nu^* = -\frac{\ln(1 - \alpha c_l)}{\alpha c_l} \quad (2.33)$$

and

$$\kappa = 0. \quad (2.34)$$

Using the normalizations of (2.21) and  $\hat{\alpha} = \alpha c_l$ , then the differential equation (2.32) becomes:

$$-\nu^* c = \frac{1}{1 - \hat{\alpha} c} \frac{dc}{d\eta} + \frac{1}{\hat{\alpha}} \ln(1 - \hat{\alpha} c). \quad (2.35)$$

To simplify the procedure, the following transformation is made [41]

$$g = \ln(1 - \hat{\alpha} c) \quad (2.36)$$

so that

$$\frac{dc}{d\eta} = -\frac{\exp(g)}{\hat{\alpha}} \frac{dg}{d\eta}$$

and we obtain a first order separable differential equation:

$$\frac{dg}{d\eta} = g + \nu^*(1 - \exp(g)). \quad (2.37)$$

An approximate analytical solution to (2.37) is detailed in Appendix 2B with the normalized steady-state concentration  $c^S$  expressed as:

$$c^S = \frac{\exp[(1 - \nu^*)\eta]}{1 + \exp[(1 - \nu^*)\eta]}$$

and upon re-instating the normalized variables, we obtain:

$$c^S = \exp[\Phi(x - \nu^*\mu_K E_a t)] \{1 + \exp[\Phi(x - \nu^*\mu_K E_a t)]\}^{-1} \quad (2.38)$$

where the superscript  $S$  refers to the steady-state case and  $\Phi = (1 - \nu^*)\mu_K E_a / D_K$ , for convenience. This Fermi-shaped profile is shown in Fig. 2.6 for  $\alpha = 0.991$ . The diffusion depth  $d$  is defined as the  $x$  value at the half-point of the concentration profile. This corresponds to  $\eta = 0$  so that

$$d \simeq \nu^*\mu_K E_a t$$

which is linearly proportional to the diffusion time,  $t$ . In comparison to the results of  $Ag^+$ -ion exchange where  $\alpha = 0$  [42], the depth  $d \simeq \mu_{Ag} E_a t$ . Here,  $\nu^* = 1$ , which is a limiting case ( $\alpha \rightarrow 0$ ) of (2.33), as expected.

Due to the assumptions on the boundary conditions discussed earlier, the above solution (2.38) is approximate. In fact, this Fermi-Dirac distribution does not satisfy the initial condition as in (2.18). It only describes the state which the system asymptotically approaches for all initial concentration profiles. Nevertheless, it provides a first order model for the Fermi-like index profile of a surface waveguide. In addition, it shows that a Fermi-like function is a more exact representation of the concentration profile of field-assisted waveguides compared to the step-index profiles quoted in the literature [5].

Before leaving this section, it is worth mentioning that a similar analytical model was derived by Abou-el-Liel for constant current field-assisted ion-exchange

[26]. The steady-state distribution  $\hat{c}_K^S$  is:

$$\hat{c}_K^S - c_r = \frac{(c_l - c_r)}{1 + \exp[\alpha \nu^* (c_l - c_r)(x^* - \nu^* t^*)]}$$

with

$$\nu^* = \frac{1 - \alpha}{(1 - \alpha c_r)(1 - \alpha c_l)}$$

and upon substituting the normalized variables, we obtain

$$\hat{c}_K^S = \left( 1 + \exp \left[ \frac{\alpha J_o}{c_o D_K} \left( x - \nu^* \frac{J_o t}{c_o} \right) \right] \right)^{-1}. \quad (2.39)$$

As with solution (2.38), a Fermi profile is obtained and the diffusion depth varies linearly with time.

## 2.4.2 Accurate numerical solutions

In this section, we present a more accurate numerical solution to the field-assisted equation which uses the initial and boundary conditions of the original problem.

The process was numerically modeled by solving (2.16).

$$\frac{\partial c}{\partial t} = \frac{\partial}{\partial x} \left( \frac{D_K}{1 - \hat{\alpha} c} \frac{\partial c}{\partial x} \right) - \frac{\mu_K E_a}{(1 - \hat{\alpha} c)} \frac{\partial c}{\partial x} \quad (2.40)$$

where the normalizations (2.21),  $\hat{\alpha} = \alpha c_l$  and the transformation (2.36) has been used again. Hence,

$$\frac{\partial g}{\partial x} = \frac{-\hat{\alpha}}{1 - \hat{\alpha} c} \frac{\partial c}{\partial x} = -\hat{\alpha} \exp(-g) \frac{\partial g}{\partial x}$$

and with similar expressions for  $\partial g / \partial t$ , one arrives at the equation:

$$\frac{\partial g}{\partial t} = \exp(-g) \left\{ D_K \frac{\partial^2 g}{\partial x^2} - \mu_K E_a \frac{\partial g}{\partial x} \right\}. \quad (2.41)$$

The spatial domain of integration is identical to that of the purely thermal exchange simulations. The initial and boundary conditions are the same as those in (2.18) and (2.19), except that, in terms of  $g$ , they become.

$$g(x, 0) = \ln(1 - \hat{\alpha} c(x, 0)) = 0$$

$$g(0, t) = \ln(1 - \hat{\alpha} c(0, t)) = \ln(1 - \hat{\alpha})$$

$$g(\infty, t) = \ln(1 - \hat{\alpha} c(\infty, t)) = 0$$

The numerical solution of (2.41) is based upon replacing the derivatives by finite differences, similar to those expressed in (2.27) and (2.28). Using  $\tau = k/h^2$ ,  $g_m^{n+1}$  is determined as:

$$g_m^{n+1} = g_m^n + \tau D_K \exp(-g_m^n) \{ [g_{m+1}^n - 2g_m^n + g_{m-1}^n] - \tau h \mu_K E_a [g_{m+1}^n - g_{m-1}^n] / 2 \} \quad (2.42)$$

The calculation proceeds as follows: first the matrix  $g_m^n$  is initialized with zeroes, except at the boundary  $x = 0$  where the values are fixed at  $\ln(1 - \hat{\alpha})$ . Note again that  $g_0^0 = 0$ . Then, the finite difference equation is calculated for the values of  $g_m^1$  using (2.42). This solution replaces  $g_m^n$  and the process is repeated for another time step until the desired time has been reached.

As mentioned earlier, the apparent choice between a two level and a three level method is a difficult one for non-linear problems. Here, the two time-level explicit scheme was compared to the three time-level implicit scheme outlined in 2.3.2, and it was found that numerical stability was achieved when  $\tau \leq 0.4$ . The typical computing time for the simulations with a 200 point spatial grid is about 60-90 minutes depending on the exchange time. However, for the implicit scheme, numerical stability was achieved for a much smaller mesh ratio, resulting in excessive computation times of over 10 hours for typical simulations. Hence, this scheme was not pursued and the conditionally stable explicit scheme was chosen.

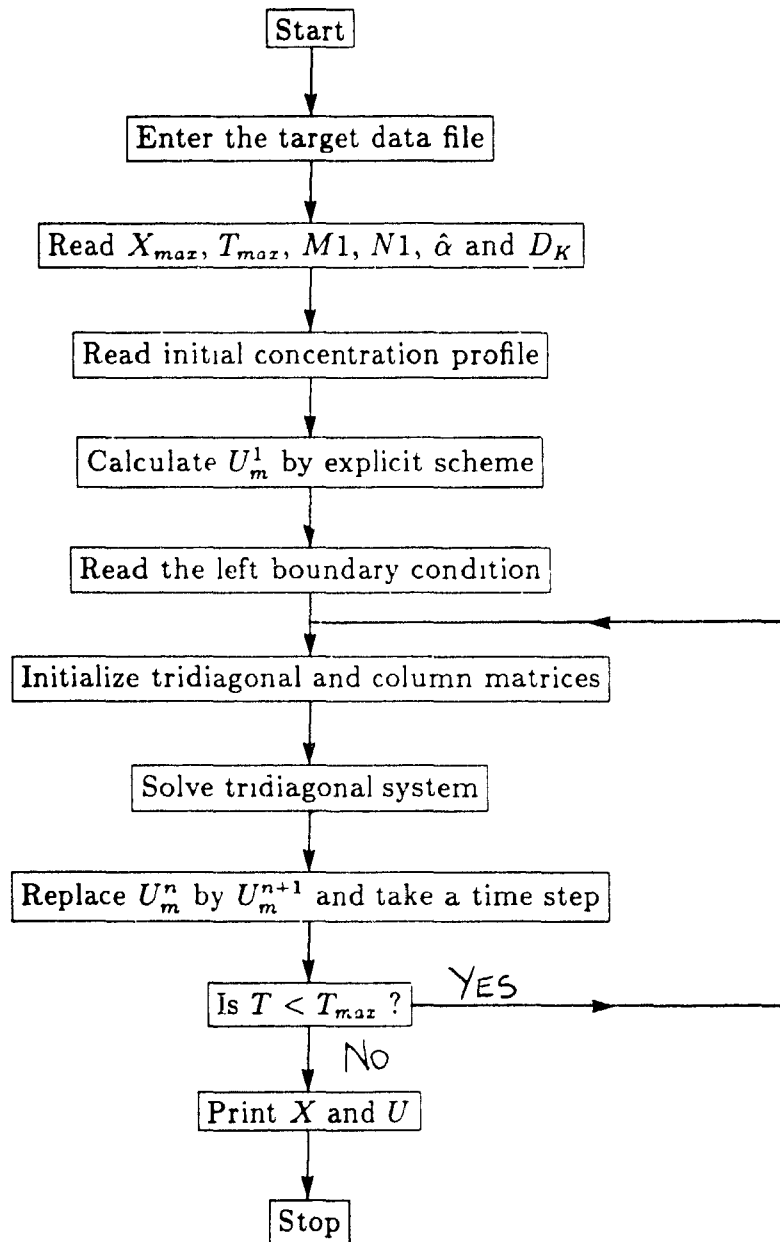
An example of a field-assisted ion-exchange concentration profile is shown in Fig. 2.7 for  $E_a = 21.1 V/mm$ ,  $t = 20$  minutes and  $T = 385^\circ C$ . Note the Fermi-like nature of the profile with the diffusion depth  $d$  located at the half-point of the profile. The mobility  $\mu_K = 8.549 \mu m^2/V \text{ min.}$  and  $D_K = 0.01186 \mu m^2/\text{min}$  [11], values corresponding to the TE modes were used. This value of the mobility was obtained from our own characterization which is based on the measurements of coefficient  $F_c$  and constant  $A_1$  to be discussed in Chapter 6.

In summary, the theoretical tools needed to establish the concentration profiles of ion-exchange waveguides have been presented. These refractive index profiles

will be used in the analysis of the waveguide propagation characteristics presented in Chapters 3 and 6.

## 2.5 Appendix 2A

Following is the flowchart of the computer program DIF1 used to calculate the ion concentration profile generated by solving the diffusion equation (2.21):



## 2.6 Appendix 2B

Following is the detailed derivation of the analytical solution:

Starting with equation (2.37), we separate the variables and integrate:

$$\int \frac{dg}{g - \nu^* \exp(g) + \nu^*} = \int d\eta. \quad (2.43)$$

However, the integral on the left hand side cannot be integrated easily and hence, a series solution for the exponential term is used to simplify integration. Since,

$$\exp(g) = 1 + g + \frac{g^2}{2} + \frac{g^3}{6} + \dots$$

then by taking the first three terms, (2.43) becomes

$$\int \frac{dg}{g(A - Bg)} = \int d\eta \quad (2.44)$$

where  $A = 1 - \nu^*$  and  $B = \nu^*/2$ . Using partial fractions, we get

$$\int \frac{dg}{g(A - Bg)} = \frac{1}{A} \int \frac{dg}{g} + \frac{B}{A} \int \frac{dg}{A - Bg}$$

and upon integrating,

$$\frac{1}{A} \ln \left[ \frac{g}{A - Bg} \right] = \eta + \frac{\ln K}{A}$$

with  $K$  being an arbitrary constant of integration. Hence,

$$\frac{g}{K(A - Bg)} = \exp(A\eta)$$

and adding unity to both sides,

$$\frac{KA - KBg + g}{K(A - Bg)} = 1 + \exp(A\eta).$$

Now, setting  $K = 1/B$ , the expression for  $g$  becomes

$$1 - \frac{Bg}{A} = (1 + \exp(A\eta))^{-1}.$$

Re-instating  $g = \ln(1 - \hat{a}c)$  and knowing that  $1 - \hat{a} \leq 1 - \hat{a}c \leq 1$ , (since  $0 \leq c \leq 1$ ),

then the first term of a series for the logarithm can be used:

$$g = \ln(1 - \hat{a}c) \sim -\hat{a}c$$

yielding

$$1 + \frac{\hat{\alpha} B c}{A} = (1 + \exp[A\eta])^{-1}$$

so that finally, we obtain

$$c = \frac{2(\nu^* - 1)}{\hat{\alpha}\nu^*} \left\{ \frac{\exp[(1 - \nu^*)\eta]}{1 + \exp[(1 - \nu^*)\eta]} \right\} \quad (2.45)$$

It must be noted that the above solution is not very accurate because we only considered the first few term of the series expressions. However, this greatly simplifies the integration and allows for a closed form solution.

In addition, for the exponential series to be accurate, we should have  $0 < g < 1$ . Since  $0 \leq c \leq 1$ , then the series argument,  $\ln(1 - \hat{\alpha}) < g < 0$ , with  $\ln(1 - \hat{\alpha}) = -2.226$ . Strictly speaking this is not appropriate for the two term expansion of (2.44). This inaccuracy is displayed in the term multiplying the Fermi-like profile of (2.45) which has a value greater than 1. Hence, the approximate analytical solution  $c^S$  is normalized with respect to this term. Further investigation of a more accurate analytical solution is needed.

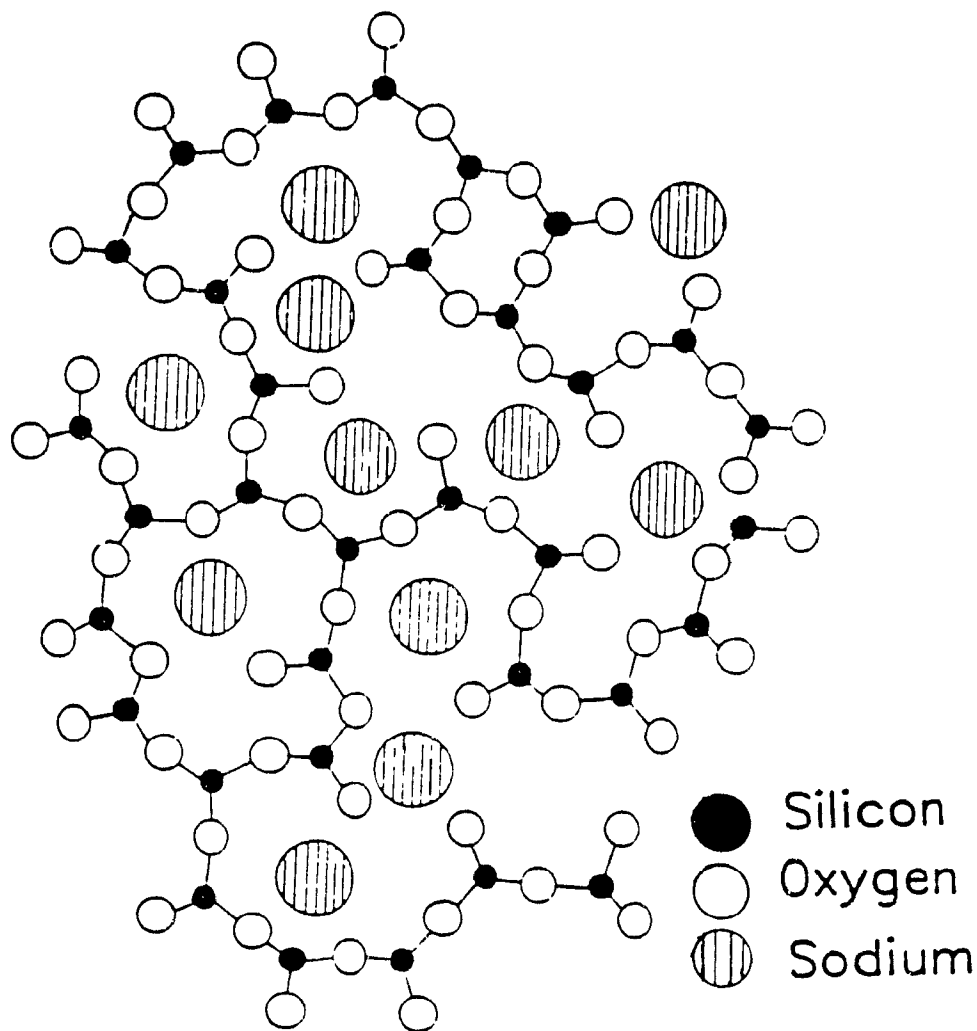


Figure 2.1: Structure of a typical soda-lime glass (see [24])

Oxide	Substrate glass (weight %)
$SiO_2$	72.31
$Na_2O$	14.33
$K_2O$	1.21
$CaO$	6.44
$Al_2O_3$	1.22
$MgO$	4.31

Table 2.1: Chemical composition of a soda-lime substrate

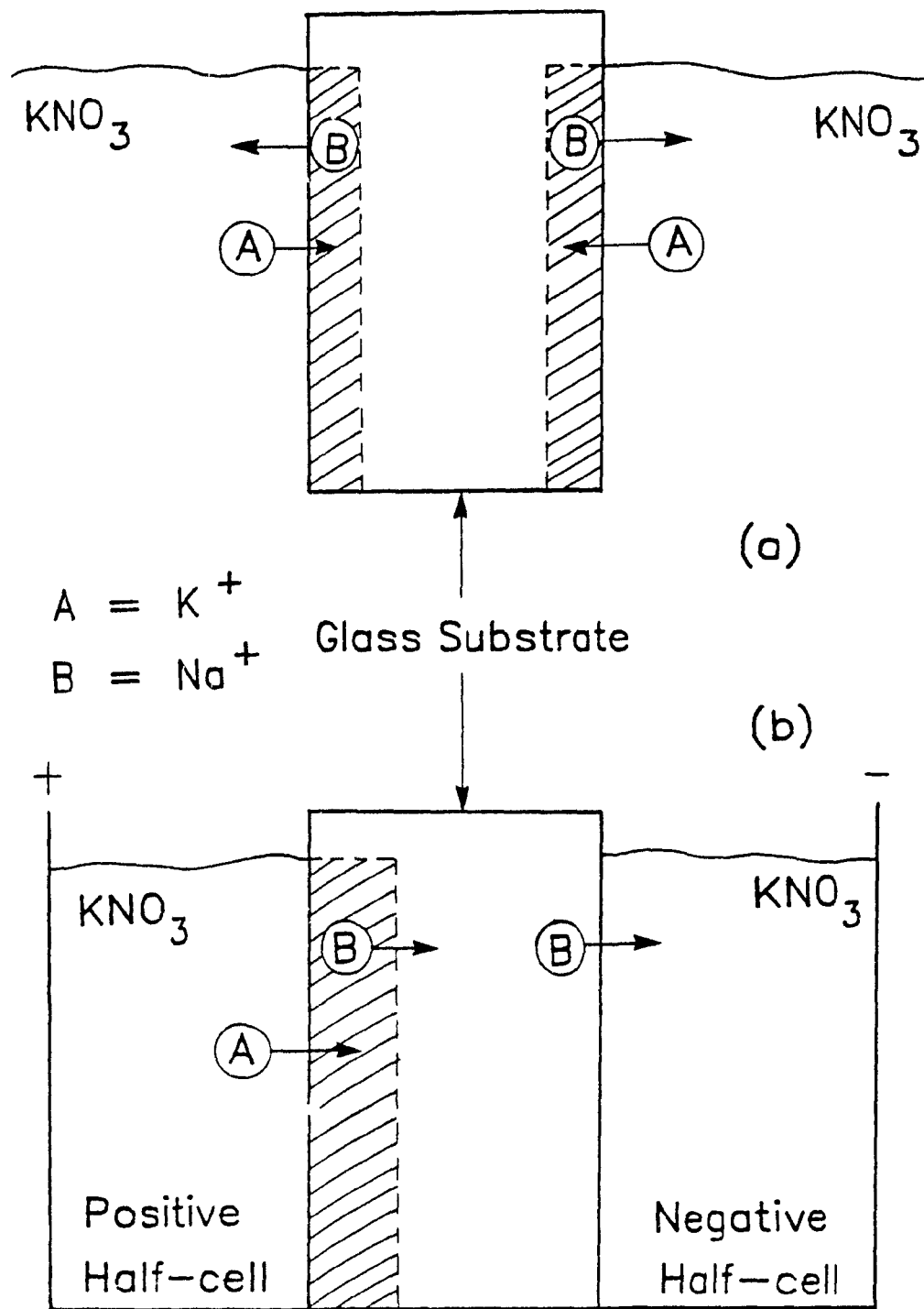


Figure 2 2 Diagram showing the ion-exchange process for (a) purely thermal exchange (b) field-assisted exchange

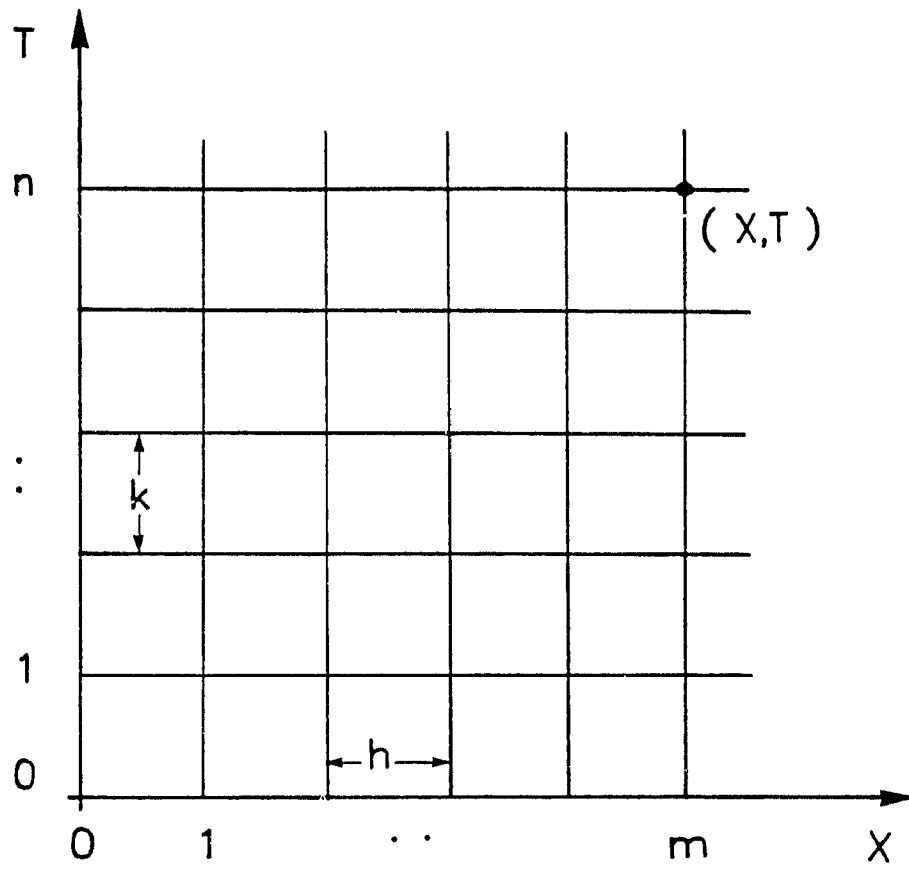


Figure 2.3: Computational grid for the numerical solution

$\hat{\alpha}$	$D_K(\mu m^2/hr.)$	$r$
0.898	0.7	0.500
0.898	2.0	0.250
0.898	3.0	0.167
0.898	4.0	0.125
0.898	5.0	0.100
0.970	0.7	0.250
0.980	0.7	0.167
0.990	0.7	0.100
0.999	0.1	0.050
0.999	0.4	0.014
0.999	0.5	0.014

Table 2.2: Typical values of diffusion parameters yielding numerical stability

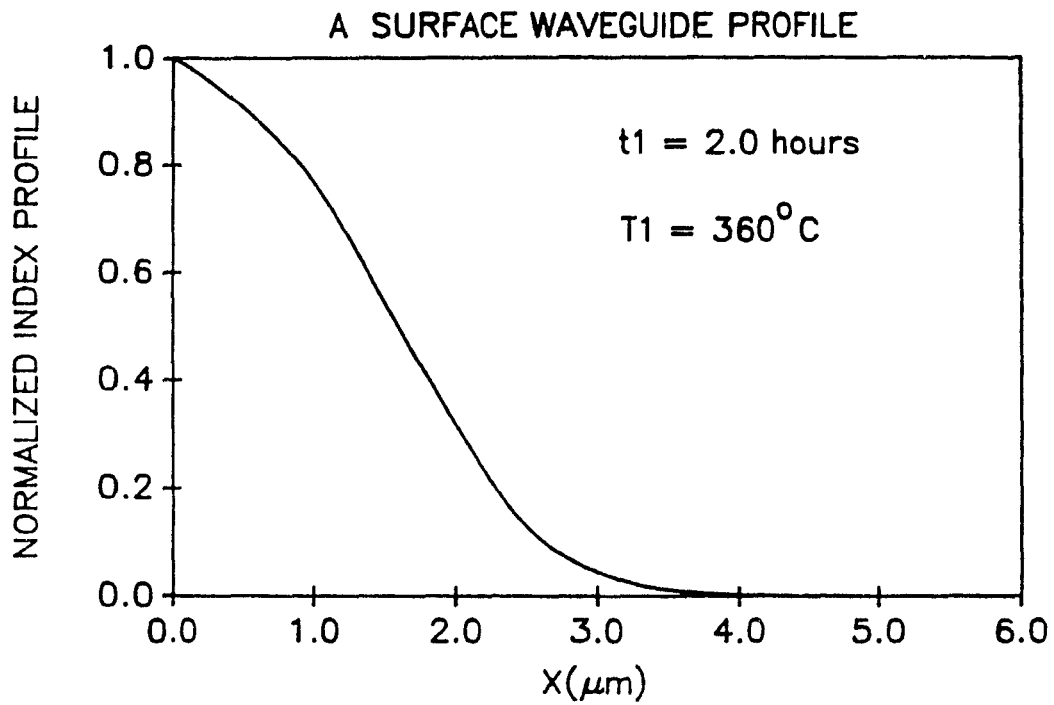


Figure 2.4: Numerical solution for a purely thermal surface waveguide

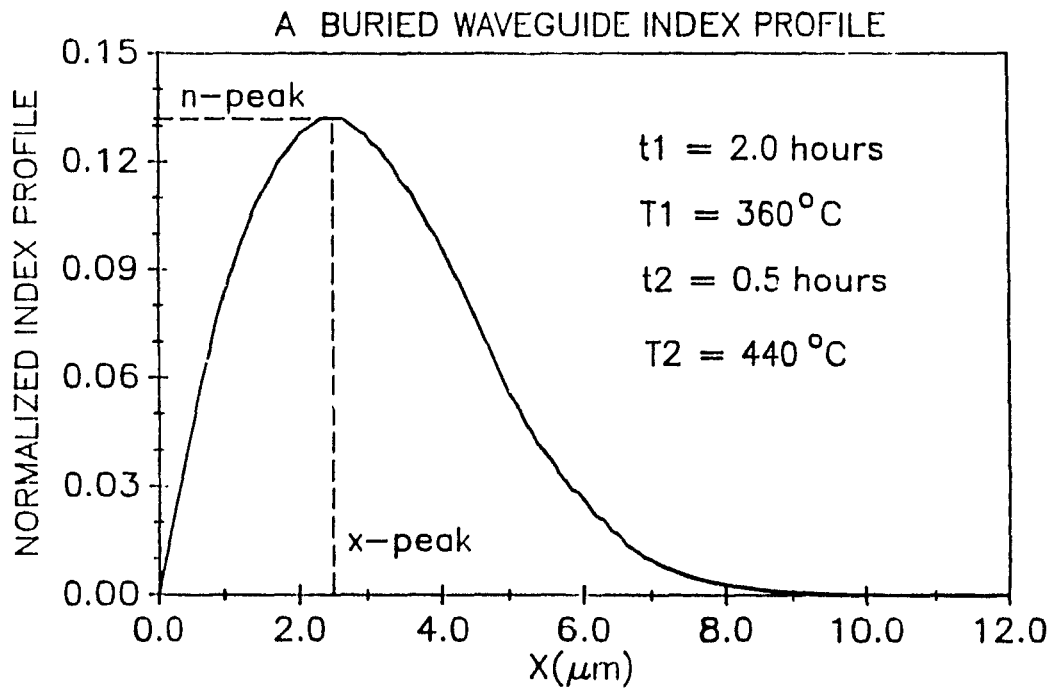


Figure 2.5: Numerical solution for a purely thermal buried waveguide

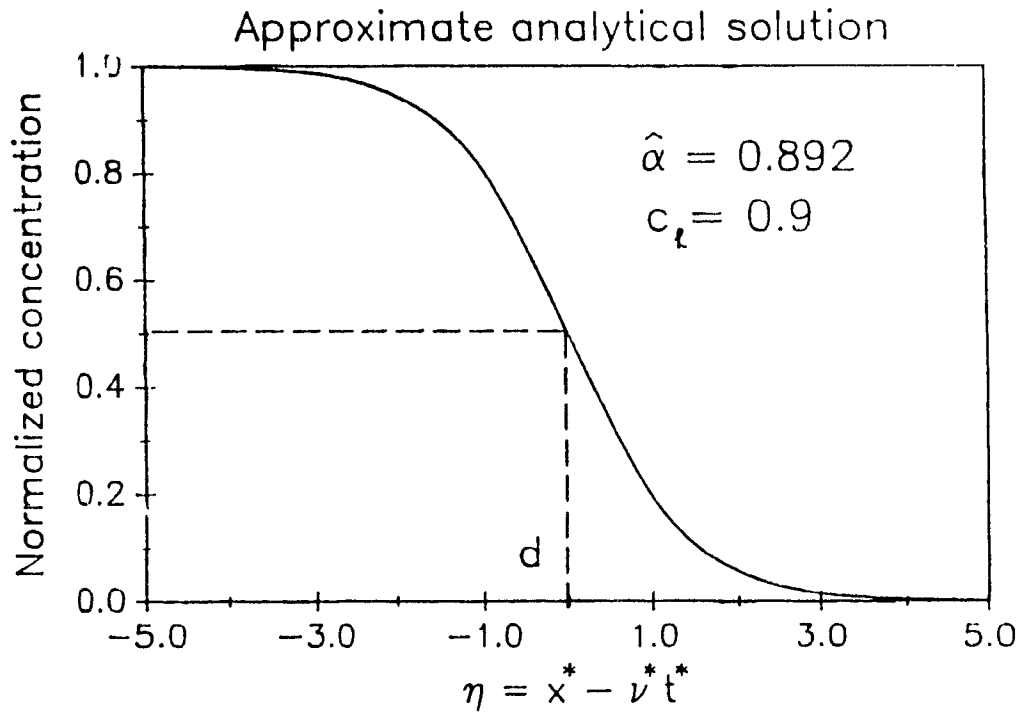


Figure 2.6: Analytical solution for a constant electric field-assisted surface guide

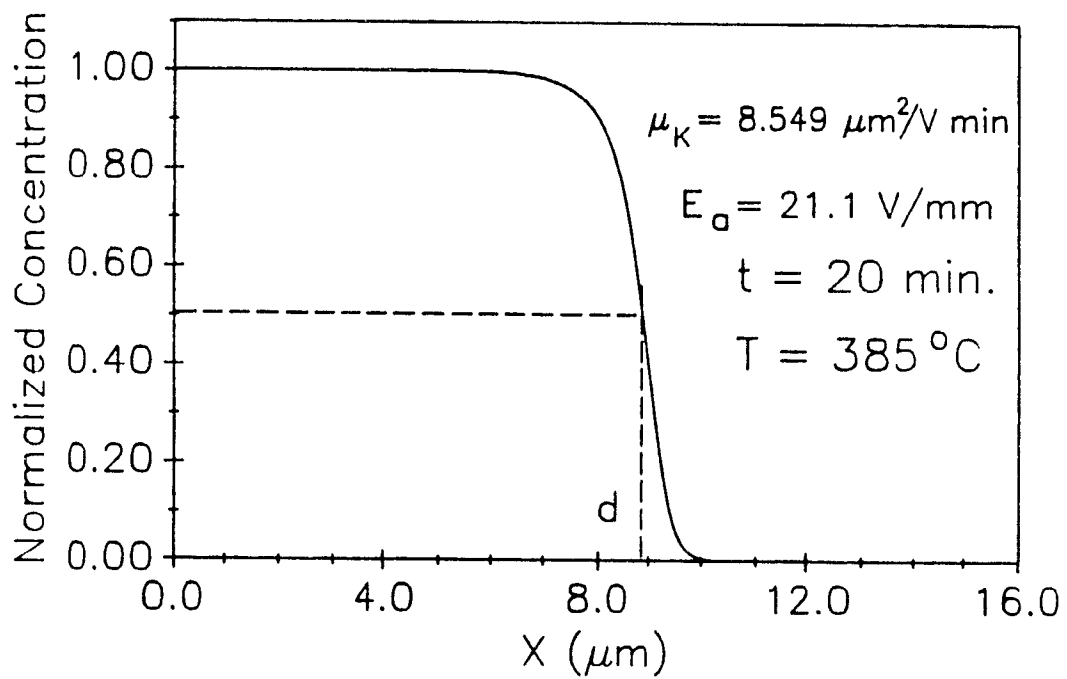


Figure 2.7: Numerical solution for a constant electric field-assisted surface guide

# Chapter 3

## Waveguide modeling and design

### 3.1 Introduction

In the following sections, the theoretical aspects of the waveguide propagation characteristics are presented. The modes of propagation of optical waveguides fabricated by the methods to be presented in Chapter 4 are derived using Maxwell's equations and solved by numerical and analytical methods. The normalized propagation constants (also known as the effective mode indices) are related to the waveguide depth by the dispersion relations. These are used to design single and multimode waveguides.

### 3.2 Basic principles

#### 3.2.1 Planar structure

The planar waveguide structure of Fig. 3.1, which has a higher refractive index  $n(x)$  than its surroundings, can be used to confine and propagate a lightwave along its propagation axis in the  $z$  direction. The geometry is asymmetric since the substrate index  $n_b$  is not the same as the air-cover region,  $n_o = 1.0$ . The inhomogeneous refractive index distribution  $n(x)$  can be written as

$$n(x) = n_b + \Delta n_s f(x) \quad (3.1)$$

where  $\Delta n_s = n(0) - n_b$  is the maximum index change and  $f(x)$  is a simple analytic function describing the shape of the index profile. For the waveguides considered

here, the index change fabricated by  $K^+$ -ion exchange  $\Delta n_s \ll 1$  [11], so that

$$n^2(x) = \begin{cases} n_b^2 + 2n_b \Delta n_s f(x) & x \geq 0 \\ 1.0 & x < 0 \end{cases} \quad (3.2)$$

### 3.2.2 Scalar wave equations

Assuming that the waveguides are isotropic, free of impurities and non-magnetic sources, Maxwell's equations are:

$$\vec{\nabla} \times \vec{H} - j\omega\epsilon\vec{E} = 0 \quad (3.3)$$

$$\vec{\nabla} \times \vec{E} + j\omega\mu_o\vec{H} = 0 \quad (3.4)$$

$$\vec{\nabla} \cdot (\epsilon\vec{E}) = 0 \quad (3.5)$$

$$\vec{\nabla} \cdot \vec{H} = 0 \quad (3.6)$$

with the fields having an exponential time dependence  $\exp(j\omega t)$ . Taking the curl of (3.4) and replacing (3.5) in the result, the vector Helmholtz equation for  $\vec{E}$  can be derived as:

$$\vec{\nabla}(\vec{\nabla} \ln(\epsilon) \cdot \vec{E}) + \vec{\nabla}^2 \vec{E} + \omega^2 \mu_o \epsilon \vec{E} = 0 \quad (3.7)$$

and similarly for  $\vec{H}$ :

$$\vec{\nabla} \ln(\epsilon) \times (\vec{\nabla} \times \vec{H}) + \vec{\nabla}^2 \vec{H} + \omega^2 \mu_o \epsilon \vec{H} = 0 \quad (3.8)$$

Note that the  $\ln(\epsilon)$  term does not vanish since the inhomogeneous dielectric term  $\epsilon(x) = \epsilon_o n^2(x)$  is a function of  $x$  only.

A planar waveguide mode describes a set of electromagnetic fields which satisfy Maxwell's equations and the appropriate boundary conditions. These fields maintain their spatial distribution while propagating along the  $z$  direction, assuming waveguide uniformity in  $z$ . Thus, the magnitude of the  $\vec{E}$  and  $\vec{H}$  fields take the form:

$$\begin{Bmatrix} E(x, y, z, t) \\ H(x, y, z, t) \end{Bmatrix} = \begin{Bmatrix} E(x, y) \\ H(x, y) \end{Bmatrix} \exp j(\omega t - \beta z)$$

where  $\beta$  defines the propagation constant of the mode. Since the index along the  $y$  direction does not vary, then all the derivatives with respect to  $y$  vanish i.e.

$\partial/\partial y = 0$ . These planar waveguides support transverse electric (TE) modes with  $E_x = 0$ , and transverse magnetic (TM) modes with  $H_x = 0$ . For TE modes, the non-trivial field components are  $(E_y, H_x, H_z)$ , while for TM modes, the components are  $(H_y, E_x, E_z)$ . The governing partial differential equations satisfying these planar waveguide conditions now become:

$$\frac{\partial}{\partial x} \left( \frac{\partial}{\partial x} (\ln(\epsilon)) \cdot \vec{E} \right) + \frac{\partial^2 \vec{E}}{\partial x^2} + (k^2 n^2(x) - \beta^2) \vec{E} = 0 \quad (3.9)$$

$$\frac{\partial}{\partial x} \left( (\ln(\epsilon)) \times (\vec{\nabla} \times \vec{H}) \right) + \frac{\partial^2 \vec{H}}{\partial x^2} + (k^2 n^2(x) - \beta^2) \vec{H} = 0 \quad (3.10)$$

The solution of the above equations can become fairly complex owing to the fact that the  $\ln(\epsilon)$  term becomes complicated for general index distributions  $n(x)$ . Fortunately, however, this term becomes negligible if [43]

$$\nabla(\ln \epsilon) = \frac{\nabla \epsilon}{\epsilon} = \frac{dn^2(x)/dx}{n^2(x)} = \frac{2n_b \Delta n_s df/dx}{n_b^2 + 2n_b \Delta n_s f(x)} \simeq \left| \frac{2\Delta n_s df/dx}{n_b} \right| \ll 1 \quad (3.11)$$

For the optical waveguides considered here,  $df/dx$  is bounded,  $\Delta n_s/n_b \ll 1$ , and hence, (3.11) is well justified. Due to this weak guidance condition, the 'scalar wave approximation' [44] is applied to the following Helmholtz equations.

$$\frac{\partial^2 \phi}{\partial x^2} + (k_o^2 n^2(x) - \beta^2) \phi = 0 \quad (3.12)$$

where  $k_o^2 n^2(x) = \omega^2 \mu_o \epsilon(x)$ ,  $k_o (= 2\pi/\lambda_o)$  is the free space wavenumber, and

$$\phi = \begin{cases} E_y & TE \text{ mode} \\ E_x = H_y/n(x) & TM \text{ mode} \end{cases}$$

The above eigenvalue equations can be solved to obtain the modes of the waveguide with the appropriate boundary conditions. The eigenvalues or propagation constants,  $\beta$ , are solved numerically for graded-index waveguides in the next section.

### 3.2.3 Exact solutions for step-index profiles

For the special case of surface waveguides fabricated by field-assisted exchange, the index profile has been shown to be step-like [15,45] with film index,  $n_f$ , as shown

in Fig. 3.2. The well-established relations for such slab waveguides can be solved by applying the continuity of the relevant field components to obtain [46]:

$$d = \frac{\phi_1 + \phi_2 + m\pi}{k_o \sqrt{n_f^2 - N_e^2}}, \quad m = 0, 1, 2, \dots \quad (3.13)$$

where

$$\phi_1 = \tan^{-1} \left( \chi^* \sqrt{(N_e^2 - n_b^2)/(n_f^2 - N_e^2)} \right); \quad \phi_2 = \tan^{-1} \left( \chi \sqrt{(N_e^2 - 1.0)/(n_f^2 - N_e^2)} \right) \quad (3.14)$$

and

$$\chi^* = \begin{cases} 1 & \text{TE modes} \\ (n_f/n_b)^2 & \text{TM modes} \end{cases} \quad \chi = \begin{cases} 1 & \text{TE modes} \\ n_f^2 & \text{TM modes} \end{cases}$$

The effective index,  $N_e$ , of the mode is defined as the normalized propagation constant,  $N_e = \beta/k_o$ . These step-index dispersion curves will be compared to those generated by a more accurate Fermi distribution in Chapter 6.

### 3.2.4 Approximate solutions for graded-index profiles

The WKB method can be used to obtain approximate solutions of the Helmholtz equation for the modes of profiles with slowly varying graded-index  $n(x)$ . This method is well-known, especially in the quantum mechanics literature, and its applications to planar waveguides has been discussed by many researchers [5]. More recently, Yip and Albert used the WKB dispersion relation to characterize  $K^+$ -ion exchange surface waveguides [11].

For planar surface guides, the WKB integral relation

$$k_o d \int_0^{\hat{x}_t} \sqrt{n^2(\hat{x}) - N_e^2} d\hat{x} = \left( m + \frac{1}{4} \right) \pi + \phi_s, \quad m = 0, 1, 2, \dots \quad (3.15)$$

with  $\phi_s = \phi_2$  of (3.14) (with  $n_f$  replaced by  $n_s$ ),  $\hat{x} = x/d$ , and  $x_t$  is the turning point defined by  $n(x_t) = N_e$ .

For planar buried waveguides, the effective indices can be found for the buried refractive index profile  $f(x)$ , characterized by the location  $x_{peak}$  and the maximum

index  $n_{peak}$ . The WKB dispersion relation for a two-turning point buried profile is [49],

$$k_o \int_{x_{t_1}}^{x_{t_2}} \sqrt{n^2(x) - N_c^2} dx = \left(m + \frac{1}{4}\right) \pi + \phi_s, \quad m = 0, 1, 2, \dots \quad (3.16)$$

and it will be used in Section 3.4 for the design of single-mode guides. The dispersion curves for the buried guides are not generated by this method. They will be analyzed by a more exact numerical method in the next section.

### 3.3 Numerical solutions of the scalar Helmholtz equation

#### 3.3.1 Background

The propagation constant and the transverse modal field distribution can in general be obtained from the solution of the scalar Helmholtz equation. However, except for a few refractive index profiles such as exponential, analytical solutions do not exist. Hence, one uses either approximate methods such as the variational method and the WKB method or uses numerical methods to obtain the solution [47,48]. It has been shown that the WKB method does not give accurate results for lower order modes and for cutoff  $V$  numbers [49]. This flaw can cause inaccuracies in single-mode design where the  $TE_0$  and  $TE_1$  mode cutoffs are crucial. Hence, one must try another method to obtain more accurate cutoffs and dispersion curves, especially for single-mode waveguides. The numerical method that seemed to suggest promising results is outlined in a paper by Kaul [50]. They used a simple Runge-Kutta technique after transforming the Helmholtz equation into a first order linear (Ricatti) differential equation. These authors found more accurate cutoff and effective index values than by using WKB.

### 3.3.2 Computation of the effective mode indices

Using the definition of the effective index, the Helmholtz equation (3.12) becomes

$$\frac{\partial^2 \phi}{\partial \xi^2} + k_o^2 d^2 [n^2(\xi) - N_e^2] \phi = 0 \quad (3.17)$$

with  $\xi = x/d$ . The solution of  $N_e$  for the fundamental mode can be determined as follows. By making the transformation

$$G = \frac{1}{\phi} \frac{d\phi}{d\xi}$$

(3.17) reduces to a first order Ricatti equation:

$$\frac{dG}{d\xi} = -G^2 - k_o^2 d^2 [n_b^2 + 2n_b \Delta n_s f(\xi) - N_e^2] \quad (3.18)$$

which can be solved with appropriate boundary conditions. In order to obtain the boundary conditions on  $G$ , we observe that for TE modes, both  $\phi$  and  $d\phi/d\xi$  are continuous everywhere. Thus,  $G$  is continuous everywhere. In air ( $\xi < 0$ ), (3.17) becomes:

$$\frac{d^2 \phi}{d\xi^2} - k_o^2 d^2 [N_e^2 - 1] \phi = 0$$

with general solution

$$\phi(\xi) = C_1 \exp \left[ k_o d \sqrt{N_e^2 - 1} \xi \right] + C_2 \exp \left[ -k_o d \sqrt{N_e^2 - 1} \xi \right]$$

Since the modal field must vanish away from the surface, then  $\phi \rightarrow 0$  as  $\xi \rightarrow -\infty$ , so that the second solution must be rejected, leaving us with

$$\phi \propto \exp \left[ k_o d \sqrt{N_e^2 - 1} \xi \right]$$

Hence, the boundary condition on  $G$  is

$$G(\xi = 0^+) = G(\xi = 0^-) = \frac{1}{\phi} \frac{d\phi}{d\xi} \Big|_{\xi=0^-} = k_o d \sqrt{N_e^2 - 1} \quad (3.19)$$

However, for TM modes,  $H_y$  and  $\frac{1}{n^2(\xi)}dH_y/d\xi$  are continuous everywhere, since  $\phi = H_y/n(\xi)$ , and thus

$$\begin{aligned}\phi(\xi = 0^+) &= \frac{H_y(\xi = 0^+)}{n(\xi = 0^+)} = \frac{H_y(\xi = 0^+)}{\sqrt{n_b^2 + 2n_b\Delta n_s f(0^+)}} \\ &= \frac{H_y(\xi = 0^-)}{\sqrt{n_b^2 + 2n_b\Delta n_s f(0^+)}} = \frac{\phi(\xi = 0^-)}{\sqrt{n_b^2 + 2n_b\Delta n_s f(0^+)}}\end{aligned}$$

Similarly,

$$\begin{aligned}\left. \frac{1}{\phi} \frac{d\phi}{d\xi} \right|_{\xi=0^+} &= \left. \frac{1}{H_y} \frac{dH_y}{d\xi} \right|_{\xi=0^+} - \left. \frac{1}{n(\xi)} \frac{dn(\xi)}{d\xi} \right|_{\xi=0^+} \\ &= (n_b^2 + 2n_b\Delta n_s f(0)) \left. \frac{1}{\phi} \frac{d\phi}{d\xi} \right|_{\xi=0^-} - \left. \frac{n_b\Delta n_s}{(n_b^2 + 2n_b\Delta n_s f(0))} \frac{df}{d\xi} \right|_{\xi=0^+}\end{aligned}$$

and thus,

$$G(\xi = 0^+) = k_o d \left( n_b^2 + 2n_b\Delta n_s f(0) \right) \sqrt{N_e^2 - 1} - \left. \frac{n_b\Delta n_s}{(n_b^2 + 2n_b\Delta n_s f(0))} \frac{df}{d\xi} \right|_{\xi=0^+} \quad (3.20)$$

Since the refractive index saturates to  $n_b$  far into the substrate (i.e.  $\xi \rightarrow \xi_o$ ,  $\xi_o \rightarrow \infty$ ), the field is expected to tend as  $\exp(-k_o d \sqrt{N_e^2 - n_b^2} \xi)$  and thus,

$$G(\xi)|_{\xi \rightarrow \xi_o} = -k_o d \sqrt{N_e^2 - n_b^2} \quad (3.21)$$

Hence, for a planar surface or buried waveguide with given values of  $k_o$ ,  $d$  (or  $x_{peak}$ ),  $n_s$ ,  $\Delta n_s$ , and  $f(\xi)$ , the problem of computing  $N_e$  for a particular mode reduces to solving the differential equation (3.18) with boundary conditions given by (3.19) or (3.20) and (3.21)

### 3.3.3 $TE_o$ and $TM_o$ modal fields

The numerical model is also useful for deducing the transverse modal fields  $E_y$  and  $H_y$  as functions of  $\xi$ . These field distributions are needed in overlap integral calculations of coupling efficiency so as to determine the insertion loss between optical fibers and buried waveguides. Such plots are quite helpful for computing the field width,  $W$ , defined as the width at which the field amplitude reduces to 1/e of its peak value.

Since  $\phi$  satisfies a linear differential equation, the solution is unique apart from a constant multiplier. Hence, without loss of generality, we may assume the field to be unity at the air-guide interface (i.e.  $\phi(0) = 1.0$ ). Since,

$$\frac{d\phi}{d\xi} = G\phi,$$

then the separable differential equation can be solved at any arbitrary value of  $\xi$  as:

$$\phi(\xi) = \exp \left\{ \int_0^\xi G(\xi') d\xi' \right\} \quad (3.22)$$

Once  $N_e$  is determined, the integral is computed numerically using Simpson's rule [38] with the integrand  $G(\xi')$  obtained from the solution of (3.18). Thus, the modal field  $E_v$  or  $H_v$  can be plotted as a function of  $\xi$ .

### 3.3.4 Numerical methodology

Equation (3.18) can be solved numerically by using a fourth order Runge-Kutta method [38] as follows:

$$G_1 = G_o + \frac{1}{6}(k_1 + 2k_2 + 2k_3 + k_4) \quad (3.23)$$

with

$$\begin{aligned} k_1 &= h\Gamma(\xi_o, G_o) \\ k_2 &= h\Gamma\left(\xi_o + \frac{h}{2}, G_o + \frac{k_1}{2}\right) \\ k_3 &= h\Gamma\left(\xi_o + \frac{h}{2}, G_o + \frac{k_2}{2}\right) \\ k_4 &= h\Gamma(\xi_o + h, G_o + k_3) \end{aligned} \quad (3.24)$$

where  $G_1$  is the value of  $G$  after a step of size  $h$  has been taken.  $G_o$  is the boundary condition expressed in (3.19) or (3.20). The function  $\Gamma(\xi, G)$  represents the right hand side of (3.18). The associated truncation error is  $\sim h^5$  and, for  $h = 0.005$  one expects accuracy of seven or eight decimal places.

The differential equation for  $G$  must be solved simultaneously while 'shooting' [38] for the boundary condition at infinity (3.21). This transcendental equation can be tackled using the Secant root search method [38]. The accuracy of the solution depends on the value of  $\xi_0$  which can be chosen arbitrarily. Thus, before solving (3.20), one has to choose a value of  $\xi_0$  and two initial guesses for  $N_e$ . These two values are related in the sense that if  $N_e$  is not sufficiently close to the true value of  $N_e$  (which must be determined by the correct solution) the solution may blow up even before  $\xi$  reaches  $\xi_0$ . Hence, the correct choice of the initial values of  $N_e$  and  $\xi_0$  is quite important in the analysis. The following steps have been taken to solve the problem:

- Choose a low enough value of  $\xi_0$ , say  $1.0 \leq \xi_0 \leq 1.5$ , and two initial guesses for  $N_e$  ( $n_b < N_e < n_b + \Delta n_s$ ). The step size value  $h$  in the Runge-Kutta scheme is 0.005 and the new value of  $N_e$  is determined by the Secant method.
- Increase the value of  $\xi_0$  by 0.1, using the  $N_e$  obtained above as the initial guess to solve  $N_e$  with better accuracy.
- The process is repeated until the desired accuracy of  $N_e$  (about  $1 \times 10^{-6}$ ) is reached.

These steps can be easily programmed to determine the effective index of the mode and its field profile. Typical computing times for these simulations, which depend on the chosen value of  $h$ , ranged from 20-30 minutes. The flowchart is presented in Appendix 3A

## 3.4 Design of single and multi-mode waveguides

### 3.4.1 Introduction

In general, the number of guided modes in optical waveguides can be derived using (3.15) and (3.16). The resulting analytical formulas are simple and can be readily used for the single-mode design of planar and channel  $K^+$ -ion exchange waveguide devices

### 3.4.2 Step-index profiles

For the step-index guides, a convenient expression can be derived using (3.13) at the cutoff condition,  $N_c = n_b$  [52], becoming:

$$k_o d \sqrt{n_f^2 - n_b^2} = m\pi + \tan^{-1} \left( \chi \sqrt{(n_b^2 - 1.0)/(n_f^2 - n_b^2)} \right) \quad m = 0, 1, 2, \dots \quad (3.25)$$

Since  $\Delta n_f \ll 1$ , then  $n_f^2 - n_b^2 = 2n_b \Delta n_f$ , resulting in the simple relation for the number of TE or TM modes

$$m = INT \left\{ 2 \frac{d}{\lambda_o} \sqrt{2n_b \Delta n_f} - \frac{1}{\pi} \tan^{-1} \left( \chi \sqrt{(n_b^2 - 1.0)/(n_f^2 - n_b^2)} \right) - \frac{1}{2} \right\} \quad (3.26)$$

where  $INT$  represents the next largest integer.

### 3.4.3 Graded-index profiles

For graded-index surface waveguides, a similar design formula can be derived. In this case, the cutoff condition,  $n(x_t) = N_c = n_b$  forces the turning point to infinity ( $x_t \rightarrow \infty$ ) [53] since the substrate index,  $n_b$ , is located far from the location of the index peak. Hence, using  $\Delta n_s \ll 1$  and  $n_s^2 - n_b^2 = 2n_b \Delta n_s f(\bar{x})$ , one obtains an expression for the number of guided modes from (3.15) as:

$$m = INT \left\{ \frac{2d}{\lambda_o} \sqrt{2n_b \Delta n_s} \int_0^\infty \sqrt{f(\bar{x})} d\bar{x} - \frac{1}{\pi} \tan^{-1} \left( \chi \sqrt{(n_b^2 - 1.0)/(n_s^2 - n_b^2)} \right) + \frac{1}{4} \right\}. \quad (3.27)$$

The function  $f(\bar{x})$  can be used to evaluate the integral analytically as will be shown in Chapter 6. This allows for a convenient formula which is useful for designing single-mode waveguides.

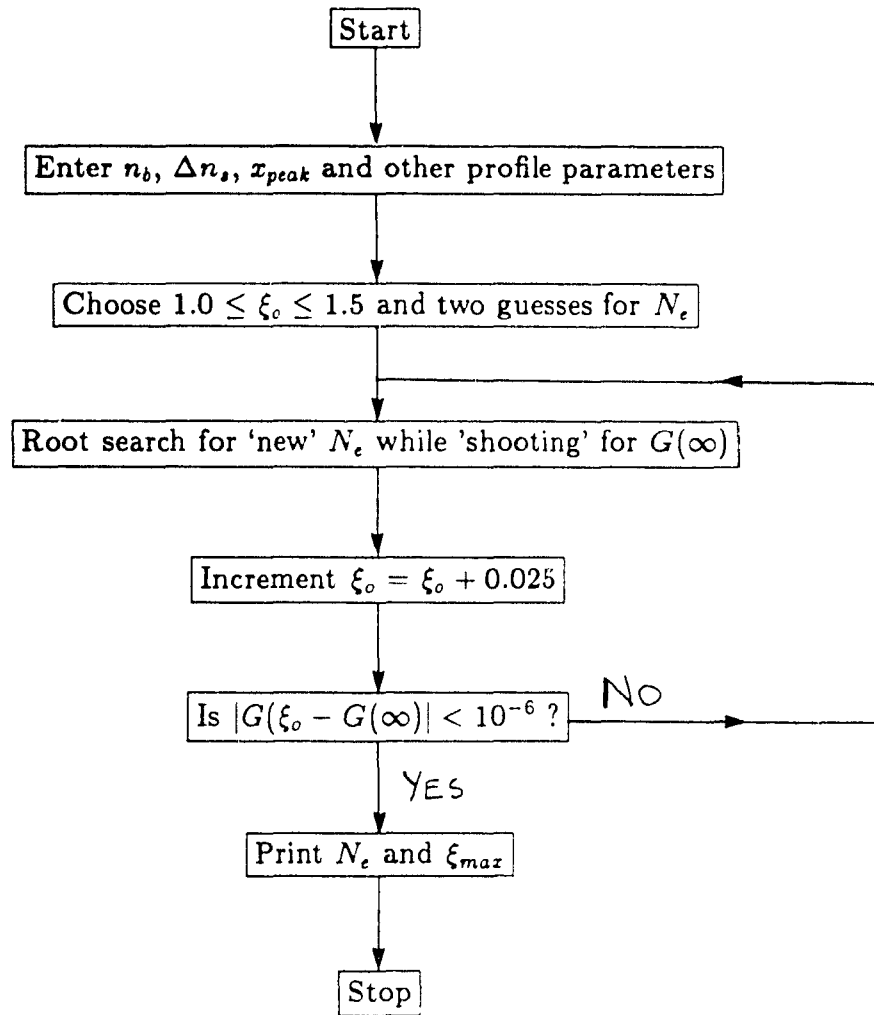
The number of guided modes in a buried waveguide can be determined, given the refractive index profile  $f(x)$ , the location  $x_{peak}$  and the maximum index change  $\Delta n_s$ . Using (3.2) and (3.16), with the turning points,  $x_{t1} = 0$  and  $x_{t2} = \infty$ , and knowing that  $\Delta n_s \ll 1$ , we get

$$k_o \int_0^\infty \sqrt{2n_b \Delta n_s f(x)} dx = \left( m + \frac{1}{4} \right) \pi + \tan^{-1} \left( \chi \sqrt{(n_b^2 - 1.0)/(n_s^2 - n_b^2)} \right) \quad (3.28)$$

Once  $f(x)$  is established more exactly, (3.28) can be used to determine an analytical relation for the design of single-mode planar waveguides, as will be shown in Chapters 5 and 6.

### 3.5 Appendix 3A

Following is the flowchart of the computer program NEBUR used to calculate the effective fundamental mode index for a buried waveguide:



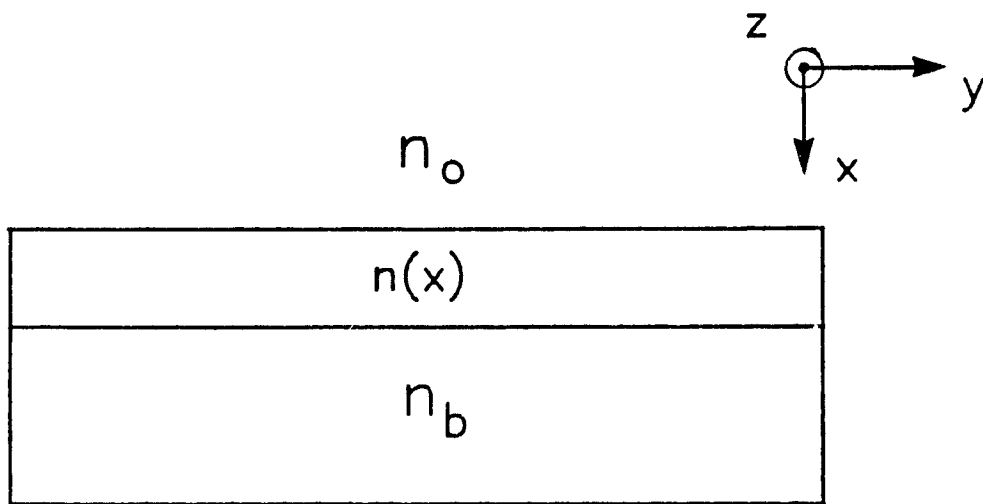


Figure 3.1: Planar waveguide structure

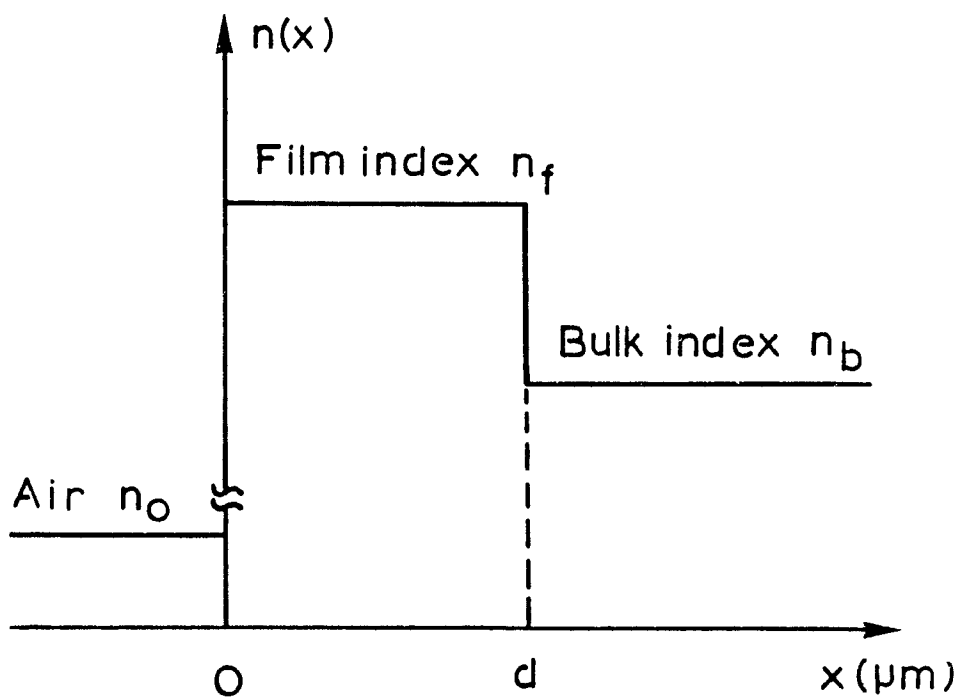


Figure 3.2: Step-index waveguide profile

# Chapter 4

## Fabrication and Measurement

### 4.1 Introduction

The fabrication and measurement techniques of planar optical waveguides are described in this chapter. The experimental apparatus used in the processes of purely thermal and electric field-assisted ion-exchange are presented together with the microanalytical measurement techniques of the  $K^+$ -ion concentration. Finally, optical measurement methods to determine important waveguiding characteristics are described.

### 4.2 Purely thermal waveguide fabrication

#### 4.2.1 Preliminary considerations

In addition to the general properties mentioned in Chapter 1, the host glass substrate must meet some desirable compositional requirements. These include

- high transmittivity over a wide wavelength region (0.60 to 1.60  $\mu m$ ) where the low loss and low dispersion windows of optical fiber are available
- low losses which can be achieved by the removal of foreign impurities, surface defects and by making the glass homogeneous

These requirements should be targeted for the ideal host glass, yet no standard glass composition has been agreed upon yet by international researchers [5]. In

fact, most commercial manufacturers of IO glass components such as Corning Inc., fabricate their own 'in house' substrate.

The substrate used in this work is a commercially available *Fisherbrand* microscope slide composed of soda-lime silicate glass (see Chapter 2). Manufactured by the Fisher Scientific Co., the slide dimensions measure  $75\text{ mm} \times 25\text{ mm} \times 1\text{ mm}$  and it has a good surface quality. The main advantage in using this substrate is that it is very cheap (approximately \$0.30 per substrate as of May 1990) compared with specially manufactured optical quality glass such as *BGG21* [54]. However, it is not of high enough optical quality to be used as a substrate for the demanding low-loss performance of commercial IO devices. Nevertheless, the soda-lime glass slides used here provides some of the desirable qualities mentioned earlier and are ideal for research applications.

#### 4.2.2 Substrate cleaning

The microscope slides are packed 'pre-cleaned' in sealed boxes but they must be cleaned thoroughly if they are to be used as substrates. This step is compulsory so as to avoid contamination of the melt and subsequent diffusion of foreign impurities into the waveguide layer. In addition, the surface must be defect-free because imperfections as small as a fraction of a wavelength of the light source can cause scattering losses.

The cleaning procedures are performed in a suitable clean-room environment. The slides are rinsed in flowing deionized (D.I.) water and then blown dry with nitrogen. Using soft cotton swabs, they are cleaned in a dilute non-abrasive Sparkleen detergent solution and rinsed again with D.I. water. Then, they are placed in an aluminum holder for further cleaning steps that include.

- 1 a 3 minute wash in an ultrasonic bath containing a few grains of detergent in 300 ml of D.I. water,
- 2 a rinse in flowing D.I. water.

3. a 3 minute ultrasonic wash in D.I. water,
4. an organic cleaning which consists of placing the holder in an empty beaker containing 20 ml of 2-propanol and then capping it with a Pyrex dish. The setup is then placed on a heating plate so that the vaporizing alcohol condenses on the substrate resulting in a cleansing action that is effective for organic decontamination,
5. a final rinse in D.I. water

Note that one must choose a cleaning procedure that is not too aggressive since it may damage the surface polish.

To assess the substrate cleanliness, a simple inspection technique known as the water break method is used [46]. If the slide is free of organic residue, the D.I. water wets the slide evenly and evaporates slowly, showing interference colours as the layer thins out. When judged clean, it is blown dry and placed in a drying oven kept at 80°C for about 10 minutes to ensure that it is completely dry before ion-exchange.

#### 4.2.3 The ion-exchange environment

In this study, pure potassium nitrate ( $KNO_3$ ) and sodium nitrate ( $NaNO_3$ ) salt crystals were used as the ionic sources for the  $K^+$  and  $Na^+$  ions, respectively. Since the melting points are quite high (334°C for  $KNO_3$  and 307°C for  $NaNO_3$ ) [55], a furnace is needed. The Lindberg crucible furnace has a vertical core and a thermocouple controlling the temperature in the 200 – 1200°C range to within 1°C. The  $KNO_3$  crystals are placed in a stainless steel crucible inside the furnace which is closed at the top by an asbestos cover. When melted, the  $KNO_3$  occupies about 200 ml. Two substrates are held in a steel clip which is attached to the end of a brass rod that emerges from a small hole in the cover. Thus, the slides can be lowered into the melt without opening the cover.

#### 4.2.4 Fabrication procedures

The purely thermal first exchange surface waveguides are fabricated as follows. The substrates are taken from the drying oven using plastic gloves and placed in the steel clip which holds them in the furnace. The setup remains suspended over the melt for a warm-up time of 10 minutes so as to bring the slides in thermal equilibrium with the melt avoiding any thermal shock. They are then lowered slowly into the  $KNO_3$  melt for an exchange time  $t_1$ . Once the time has elapsed, they are raised from the melt, the setup is removed from the furnace, and the substrates are coaxed out of the clip using steel calipers. They fall into a soft bed of tissue paper where they are allowed to cool for about 20 minutes. Since some residual  $KNO_3$  recrystallizes on the glass surface during cooling, the slides must be washed clean of the salt in running D.I. water before they can be measured.

To fabricate buried guides by backdiffusion, the surface guides (fabricated at  $T_1 = 360^\circ C$  for time  $t_1$ ) are subjected to a similar process in  $NaNO_3$  at  $T_2 = 440^\circ C$  except that the warm-up time is reduced to 2 minutes. This was done to prevent the index profile of the surface guide from being modified by annealing. Furthermore, this short time is enough to bring the sample in thermal equilibrium with the melt.

### 4.3 Electric field-assisted waveguide fabrication

This ion-exchange process is much more complicated than the purely thermal and deserves its own section in this thesis. This technique is new to the McGill Guided Wave Optics laboratory but has been used in other research institutions worldwide [15,56].

#### 4.3.1 Experimental setup

The configuration used for the fabrication of optical waveguides by the field-assisted ion-exchange process is basically comprised of three structures

- the electrodes and their support
- the molten salt support
- the external electrical equipment

The electrode configuration (see Fig. 4.1(a)) is comprised of two 'C' shaped stainless steel (S.S.) blocks which have been milled to form half-cells for holding the  $KNO_3$  melt [56]. Note that most of the steel which comes in contact with the salt is stainless so as to avoid contamination. They are placed facing each other with the glass substrate and Teflon isolation sheets sandwiched between them. The two holes in the corners of the electrodes are used for attaching Teflon-protected wires to form positive and negative potential. The electrodes are held together by two S.S. plates which are connected with seven S.S. screws and bolts (see Fig. 4.2)

At the top of the electrode configuration, a flat aluminum plate is used to support two S.S. cones which are used to funnel the salt into each half-cell. This plate is fastened to the two S.S. plates by brackets. The melt is held in two S.S. cylindrical containers which lie just above the cones and are supported by a T-section with wire levers (see Fig. 4.3)

The electrode setup, up to the aluminum plate, is put into a tin can and filled with sand for thermal isolation. This is important to avoid thermal shock and subsequent cracking of the substrate during the cooling process. This can and the whole apparatus is placed in an aluminum cylinder which is then put in the vertical furnace. An asbestos lid with a hole in its center (for the emerging wires) is used to cover the furnace top. The wires are connected to the external electrical equipment which include a voltage controlled D.C. power supply and a current meter as shown in Fig. 4.4. The current meter has a variable DC ( $mA$ ) current range and the voltage source is internally protected against short circuits. A full list of the lab materials needed is shown in the Bill of Materials in Table 4.1

## 4.4 Fabrication procedures

The fabrication procedures are described below in list form as follows:

1. Preparing Teflon sheets : These sheets are needed to electrically isolate the electrode and substrate. Two 'U' shaped pieces and one rectangular piece are cut, as shown in Fig 4.1(b).
2. Electrode sandwich · The rectangular sheet is placed on one S.S. plate. Then one electrode is put on top of it, followed by a 'U' sheet, the glass substrate, another 'U' sheet, the other electrode and the other S.S. plate in a sandwich-like process. Ensure that the smooth part of the glass substrate is facing the positive electrode. Also, the S.S. plates should always be flat and smooth; polishing paper should be used when needed. The seven S.S. screws and bolts are inserted in the plates and tightened gently. Tightening too hard will cause the substrate to crack during cooling however, if the setup is too loose, the molten salt will leak into the sand. Practice is needed to develop the correct tightness.
3. One Teflon-coated wire is fastened by screw onto the electrode which has been isolated by the Teflon sheets.
4. Then the flat aluminum plate is fastened to the S.S. plate by four small screws. The other wire is now screwed to the small hole on the S.S. plate which is in contact with the other electrode.
5. At this point, a short circuit check is needed. This is done by connecting the two Teflon-coated wires to the positive and negative terminals on the power supply. A low ammeter reading of about 0.01 mA signifies good electrical isolation.

6. The two cones are placed in each half-cell and the whole setup is placed in a tin can which is subsequently filled with sand using a plastic funnel.
7. The melt containers are then filled with  $KNO_3$  crystals using a teaspoon to about three-quarters capacity.
8. This whole configuration is then fitted into the special aluminum cylinder and then placed carefully in the furnace using a U-shaped wire. The furnace is covered with the lid.
9. The electric circuit is completed as shown in Fig. 4.4.
10. The furnace is turned on and a waiting period of about 2.5 hours is needed for the temperature to reach  $385^\circ C$ .
11. After this time, the lid is removed and the containers holding the molten salt are tilted by using the wire levers and a steel caliper so that the salt is poured into the cones. Cotton gloves should be used to avoid any burns
12. After pouring the melt, the cones are removed immediately. The voltage source is turned on and the ammeter begins recording the ionic current in desired intervals of time. If a short occurs, the voltage will be low and the current high. Turn off the furnace and voltage source and return to step 1 after the furnace has cooled down
13. When the exchange time is reached, the power supply and furnace are turned off and the asbestos lid is removed by placing it near the side of the furnace opening. A steel caliper is helpful for removing the lid
14. Wait for ten minutes. This step avoids thermal shock and subsequent cracking of the substrate. However, it means that the waveguides are still being influenced by ion-exchange. This step must be included in the concentration profile modeling (see Chapter 6) and the temperature was measured to

be  $T = 379^{\circ}C$ . Future improvement of this step is needed to simplify the process and the index profile modeling.

15. Finally, the whole setup is removed from the furnace using the U-shaped wire. The cooling time is about one hour. A graph describing the total diffusion process is shown in Fig. 4.5.

## 4.5 Ion concentration measurement

### 4.5.1 Introduction

The direct measurement of the dopant concentration profile is an important step in the fundamental characterization of optical waveguides. Analytic tools such as electron or ion probe microanalysis (EPMA), scanning electron microscopy (SEM), or atomic absorption spectrometry have been used for ion-exchange waveguides [5]. In this thesis, two such techniques (SEM and EPMA) have been used to study the chemical constituents and concentration profiles of the glass waveguides. Another technique is to use optical measurements (described in Section 4.6) to determine indirectly the best fitting refractive index profile. Here, the index profile is assumed to be a replica of the concentration profile.

### 4.5.2 Waveguide preparation

Before the waveguides can be analyzed for the SEM analysis, they must be prepared in a special way. The samples were first mounted edge-on in a mold cup which was then filled with a resin-based compound. This compound was then cold-cured in a pressure vessel for about 30 minutes. Then, the samples were ground and polished on a variable speed polishing machine in the following manner:

- a 400 grit bronze disk for 2 minutes at 15 psi
- a 600 grit bronze disk for 45 seconds at 15 psi
- a 9 micron compound on an aluminum (Al) disk for 2 minutes at 40 psi

- a 1 micron compound on an Al disk for 1 minute at 40 psi
- a colloidal silica liquid on an Al disk for 30 seconds at 40 psi

The polisher was set at 100 rpm speed. This polishing procedure provided a smooth surface and a strong edge retention which is important since most of the waveguide region is within 10 microns of the edge. Finally, the samples were carbon coated with a 50 Å thin film to prevent charging of the sample during the analysis

For the EPMA, only the waveguide side of the glass surface was analyzed and hence, the preparation was much simpler. The samples only had to be cut into  $3 \times 5$  cm pieces so as to fit into the special EPMA holder and then carbon coated, as before.

### 4.5.3 Scanning electron microscopy (SEM)

The SEM can be used for determining the concentration profile in two ways. One approach is to analyze X-rays (known as energy dispersive spectroscopy, EDS) characteristic of the desired ion or, alternatively to study the back-scattered electrons (BSE's) originating from the sample [57]. Both have been successfully used to measure  $Ag^+$  concentration in soda-lime glass waveguides.

Here, the SEM-BSE approach was studied, for the first time, for  $K^+$  concentration profiles [18]. The JEOL TSM-300 was used for the experiments and its operating procedure is described as follows. An electron beam was focused onto a small area of the sample close to the edge. A solid-state BSE detector was used as shown in Fig. 4.6. By line scanning within  $10 \mu m$  near the edge of the polished end-face of the sample, a good indication of the concentration is obtained by the BSE intensity profile. The yield of these electrons, which depends on the backscattering coefficient, is generally found to increase with increasing atomic number [58]. In a homogeneous mixture of several elements, like glass, the composite coefficient depends on each pure element's coefficient and its weight fraction. In these samples, the waveguide region is composed of a mixture of ions such as  $K^+$ ,  $Na^+$ ,  $Si^{4+}$  and

$Ca^{2+}$  found in oxides. Since the atomic number of potassium is higher than the rest of the ions, except for calcium, and its weight fraction is considerable in the guiding region, the contribution of  $K^+$  ions to the yield of BSE is dominant. To obtain a good BSE-SEM image with a solid-state detector, it is important to have samples with minimal surface roughness and fine edge definition. The surface of the sample should be perpendicular to the scanning electron beam and parallel to the detector [59]. These conditions are achieved using the polishing methods described in 4.5.2.

#### 4.5.4 Electron probe microanalysis (EPMA)

The electron microprobe has been used successfully to measure the  $Ag^+$  concentration and more recently, the  $K^+$  profile [5]. In this method, X-ray photons emitted from the sample are analyzed for their chemical composition.

In this thesis, a quantitative electron microprobe analysis [60] in 'line mode' was conducted to study the glass substrate and waveguide compositions just at the samples' surface. The CAMECA electron microprobe was used for the experiments and its operation is explained as follows. Similar to the SEM, an electron beam is focused onto a small ( $\sim 1 \mu m$ ) area of the sample from which X-rays characteristic of the chemical composition are emitted. The emitted X-rays containing the necessary information are dispersed in their wavelength spectrum and the intensity of these spectral lines are measured quantitatively. These photon intensities depend on the concentration of the element in the sample and hence, the EPMA needs to be calibrated for the constituents to be analyzed. The intensities are detected by an argon/methane gas detector, amplified, and then the oxide concentrations, in weight fraction, are printed on an output device. For a more detailed description of the microprobe, the reader is referred to [61].

The detailed results of these experimental findings in comparison to the theoretical modeling of the ion-exchange process, using both the SEM and the EPMA, are discussed in Chapter 5.

## 4.6 Measurement of propagation characteristics

### 4.6.1 Preliminary considerations

After fabricating these waveguides, their propagation characteristics need to be measured. These include the refractive index parameters, such as the waveguide depth and index change, and the propagation losses. In this thesis, two established techniques based on two-prism coupling were used. The first method involves measuring the propagation constants of all the modes that can be excited in a waveguide to determine its index profile. This method offers an indirect way of determining the profile, whereas the SEM technique offers a direct way to obtain the profile. The second method involves measuring the propagation losses of optical waveguides. These are very important because they can influence the performance of passive optical integrated circuits.

### 4.6.2 Modal spectroscopy

Modal spectroscopy involves using a two-prism coupler configuration to selectively excite the guided modes of a waveguide [46]. The theoretical aspects of the prism-coupler have been described often [62] and are not presented here. However, the measurement setup is described below in detail.

To measure the propagation constants,  $\beta$ , with great accuracy, the coupling 'synchronous' angles,  $\theta$ , must be known precisely. The measurement of these angles was performed using the setup in Fig. 4.7. Laser light from a 5 mW He-Ne source operating at  $0.6328 \mu\text{m}$ , passes through a polarizer to select TE and TM modes. Then, the incident beam is 'evanescently' coupled into the waveguide using a LaF60 glass prism. An identical output prism located a short distance away couples the beam out of the guide. The resulting far-field pattern shows sharp vertical lines, known as m-lines, which can be excited individually (see Fig. 4.8). The prism-waveguide holder, shown in Fig. 4.9, rests on a 3-axis micropositioner which is

itself mounted on a precise rotational stage with 5 arc-second accuracy. The angular measurement at which the m-line appears brightest is recorded. The reference marker is used to measure the zero reference angle by adjusting the rotational stage until the incoming beam is reflected back onto itself.

The normalized propagation constants,  $N_e$ , are obtained from the angle of incidence using the following formula [46] derived from geometrical optics:

$$N_e = \frac{\beta}{k_0} = n_p \sin \left\{ \alpha_p + \sin^{-1} \left( \frac{\sin \theta_i}{n_p} \right) \right\} \quad (4.1)$$

where  $n_p$  is the refractive index of the prism,  $\alpha_p$  is the prism's base angle, and  $\theta_i$  is the coupling angle of the beam relative to the zero reference. The value of  $\alpha_p = 58.37^\circ$  and  $n_p = 1.780$  for the wavelength  $0.6328 \mu m$ .

This experimental scheme yields an accuracy of  $\pm 1$  arc-minutes in the measurements of  $\theta_i$ , corresponding to an accuracy of  $\pm 2 \times 10^{-4}$  in the measured values of  $N_e$ . The errors in the values of  $\alpha_p$  and  $n_p$  lead to an additional uncertainty of  $\pm 3 \times 10^{-4}$ . The refractive index of the soda-lime glass substrates  $n_b = 1.5125$ .

### 4.6.3 Propagation loss

To improve the performance of optical devices in IO applications, it is desirable to fabricate waveguides with low propagation loss. These losses are dominated by absorption (owing to the presence of foreign impurities) and scattering contributions caused by glass inhomogeneity and surface defects. In the literature, a variety of techniques have been developed to measure the propagation loss [63,64]. Here, the two-prism sliding method [65], was used

The experimental setup is presented in Fig. 4.10 with the identical prism-coupler configuration of Fig. 4.9. One must ensure that the sample and both prisms are very clean, the accuracy of the measurements may be affected by dust particles. When a mode is excited, the m-line on the white screen is imaged by a Hamamatsu video camera. The camera's output signal is then displayed on a video monitor whose analog output is fed into a channel input of an oscilloscope. The

m-line is observed on the scope by scanning the time base in a Horizontal Mode A. This allows for one frame of the video signal to be displayed by sharp vertical lines. The voltage level,  $V$ , of the line with the largest magnitude is recorded when the mode is excited. The output prism positions,  $L_{pi}, i = 1, \dots, N$ , are measured accurately using a Vernier caliper. At each  $L_{pi}$ , the voltage peak on the scope is measured and then the output prism is moved a few millimeters towards the input prism. This is done repeatedly to get at least 5 data points. The last prism position,  $L_{pN}$ , closest to the input prism (roughly 1 mm) is used as the reference to measure the propagation distance  $\Delta L_i = L_{pN} - L_{pi}$ . The experimental conditions (i.e. the prism holders) are such that this small distance is unavoidable yielding a small error in  $\Delta L_i$ .

An important requirement is that nearly 100% efficiency from the output prism coupler must be achieved during the measurements in order to maintain constant coupling efficiency [53]. This is quite difficult to achieve considering that point pressure on the prism is fluctuating for every measurement. Hence, reproducibility is affected and the measurement errors are estimated to be 0.2 – 0.3 dB/cm. To improve the situation, the use of matching fluids [65] has shown to make the coupling stronger with nearly perfect efficiency.

The propagation losses are calculated as follows. By plotting the values of  $V^2$  versus  $\Delta L(\text{mm})$  on semi-log paper, a best linear regression fit is obtained through these points. The losses are evaluated from the slope of the line. We assume that the output power  $P$  follows

$$P = P_o \exp(-\alpha \Delta L)$$

where  $P_o$  is the input power and  $\alpha$  is a measure of the propagation loss. Taking  $\log_{10}$  of both sides, we get

$$\log_{10} P = \log_{10} P_o - \alpha (\log_{10} e) \Delta L$$

For convenience, let  $A = \alpha \log_{10} e$ , so that

$$\log P = \log P_0 - A\Delta L$$

Now, in the decibel scale,  $1dB = 10 \log(P/P_0)$  so that

$$10 \log(P/P_0) = -10A\Delta L$$

Hence, we multiply our regression fit slope by 10 to get the actual value of loss in  $dB/cm$ .

This completes the description of the experimental apparatus and techniques used in this thesis. The reduction and analysis of the results are presented in the following chapter.

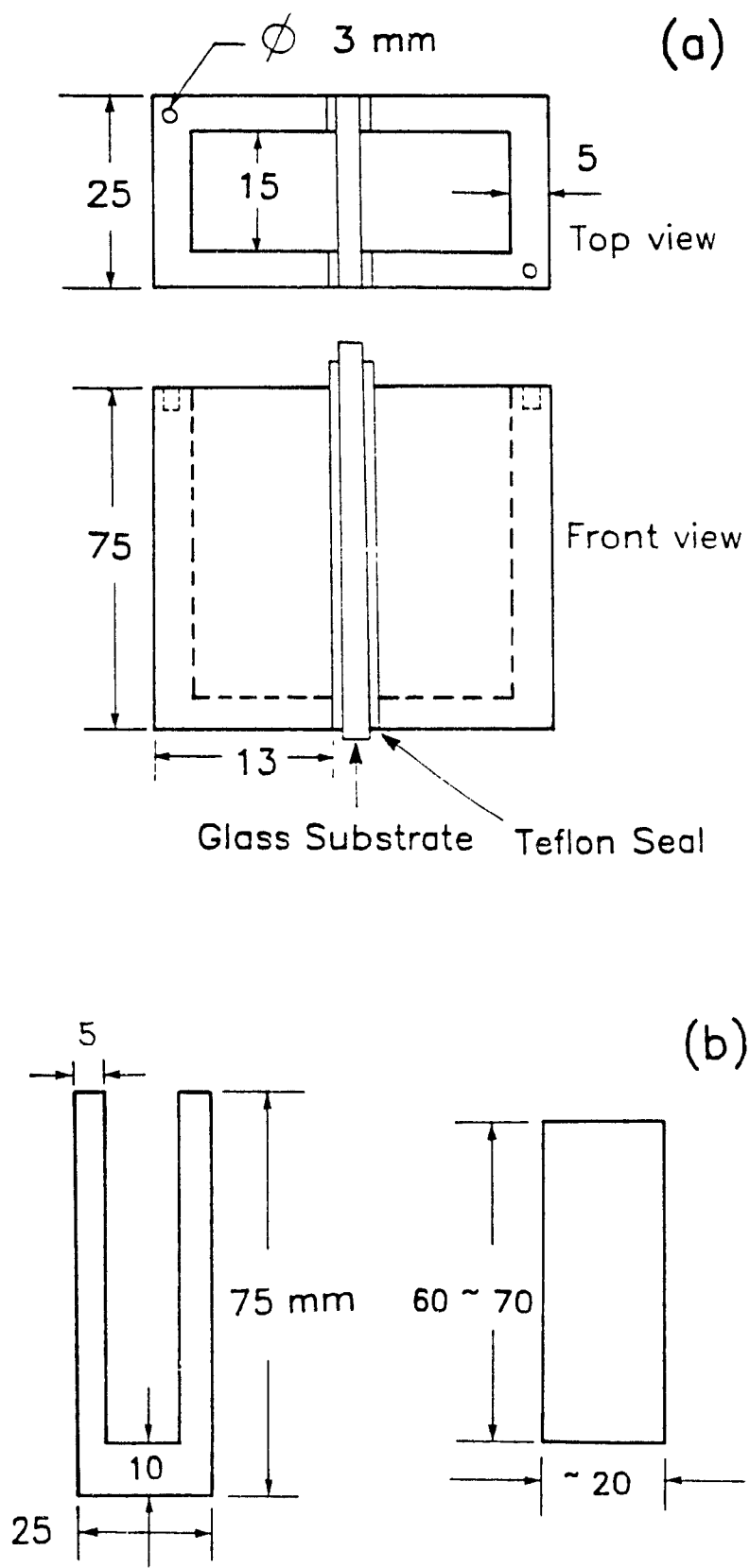


Figure 4.1: Diagram showing (a) half-cell configuration and (b) Teflon seals

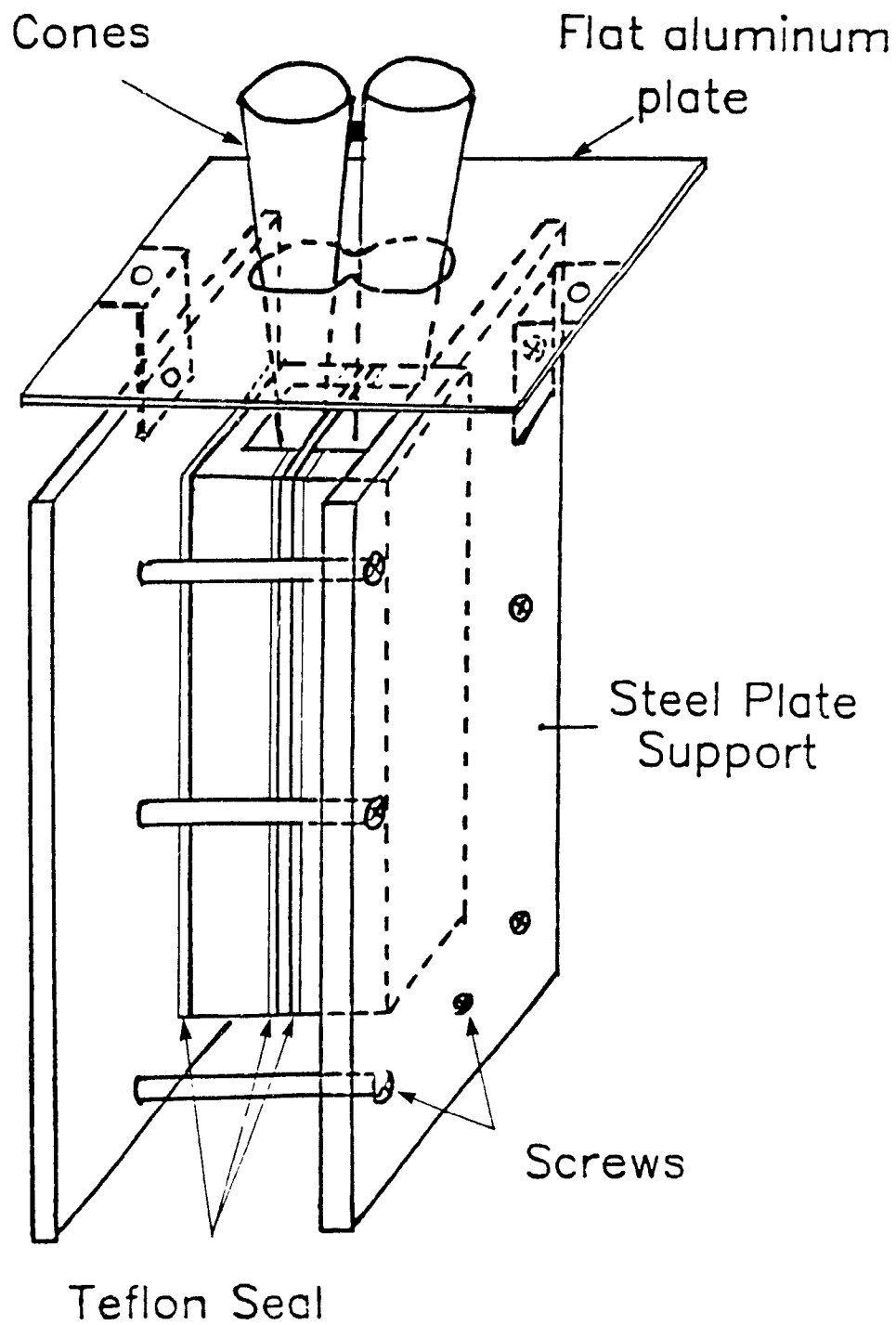


Figure 4.2. Complete electrode configuration

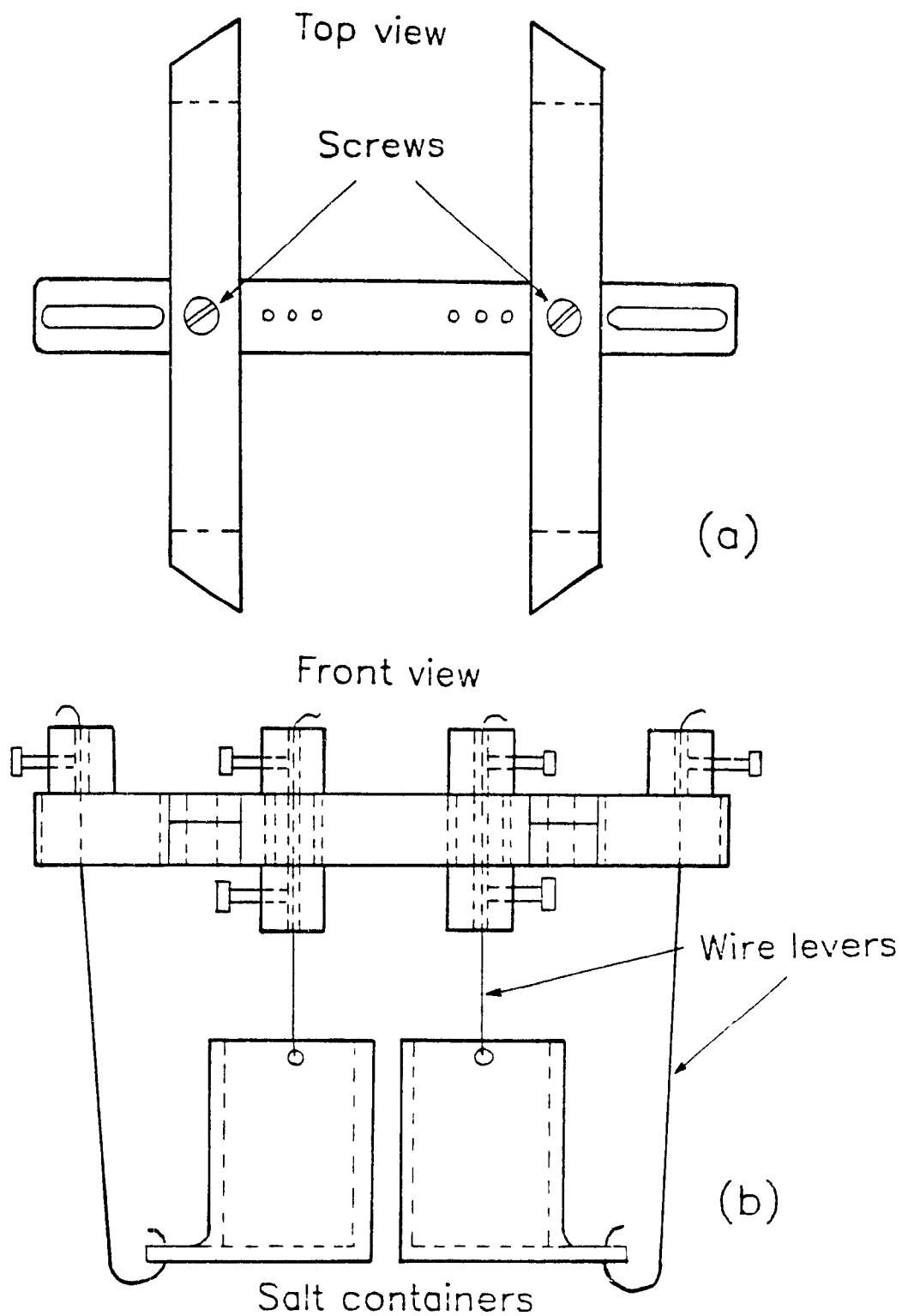


Figure 4.3 Schematic of (a) T-section and (b) wire levels

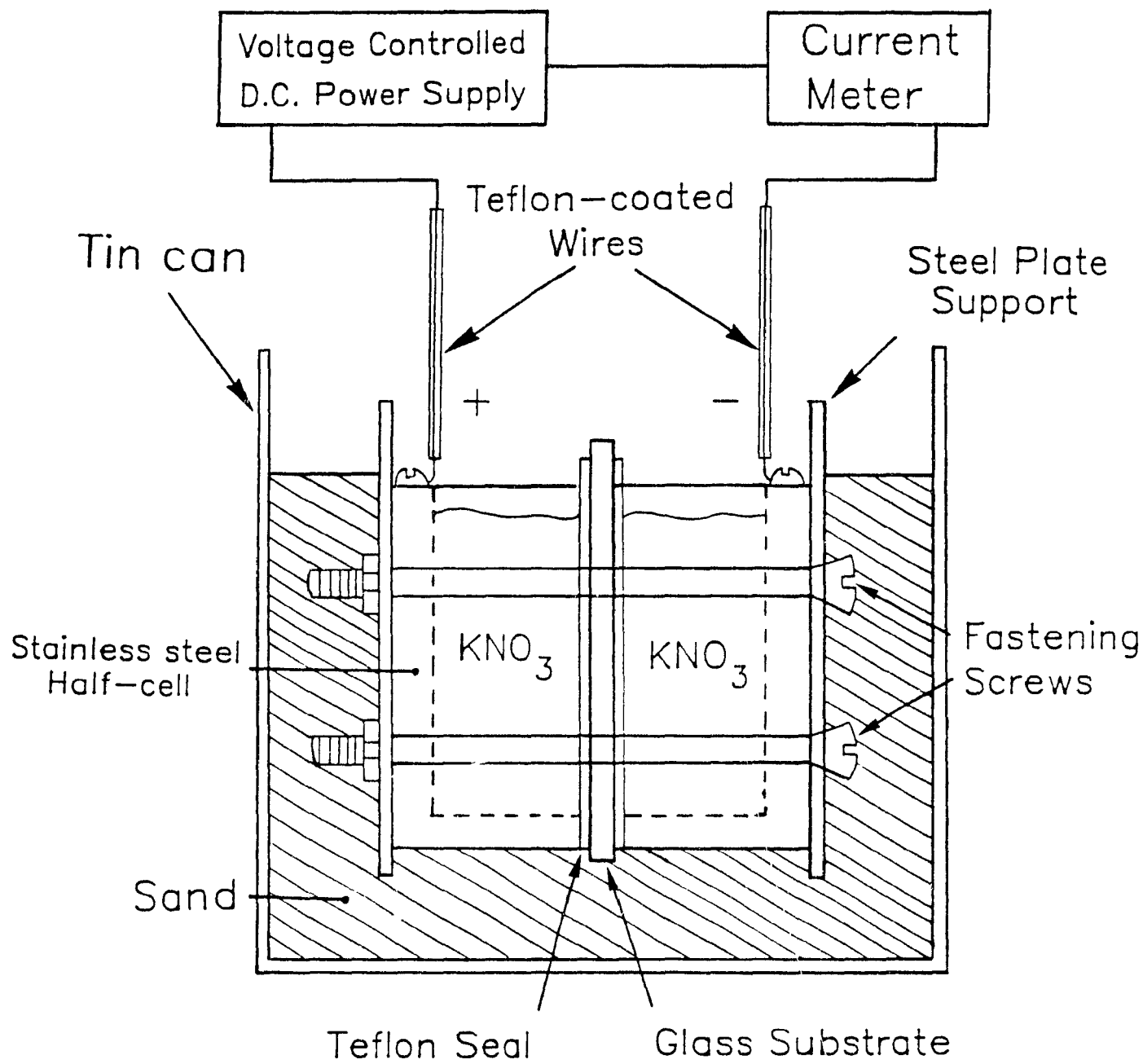


Figure 4 4 Schematic of the electric field-assisted apparatus

Item	Quantity	Description
1	1	0.030 inch thick Teflon sheet
2	2	Stainless steel plates
3	2	Stainless steel(S.S.) electrodes
4	1	Teflon 'spaghetti' tubing
5	7	0.25 inch S.S. screws and bolts
6	14	0.25 inch lock washers
7	4	S.S. cones
8	1	Tin can
9	-	Sand (playground)
10	1	Plastic funnel
11	2	S.S salt containers
12	6	Cotton glove pairs
13	1	Steel caliper
14	-	$KNO_3$ salt crystals
15	-	Thermally protected wire
16	1	Special aluminum cylinder

Table 4.1: Bill of materials

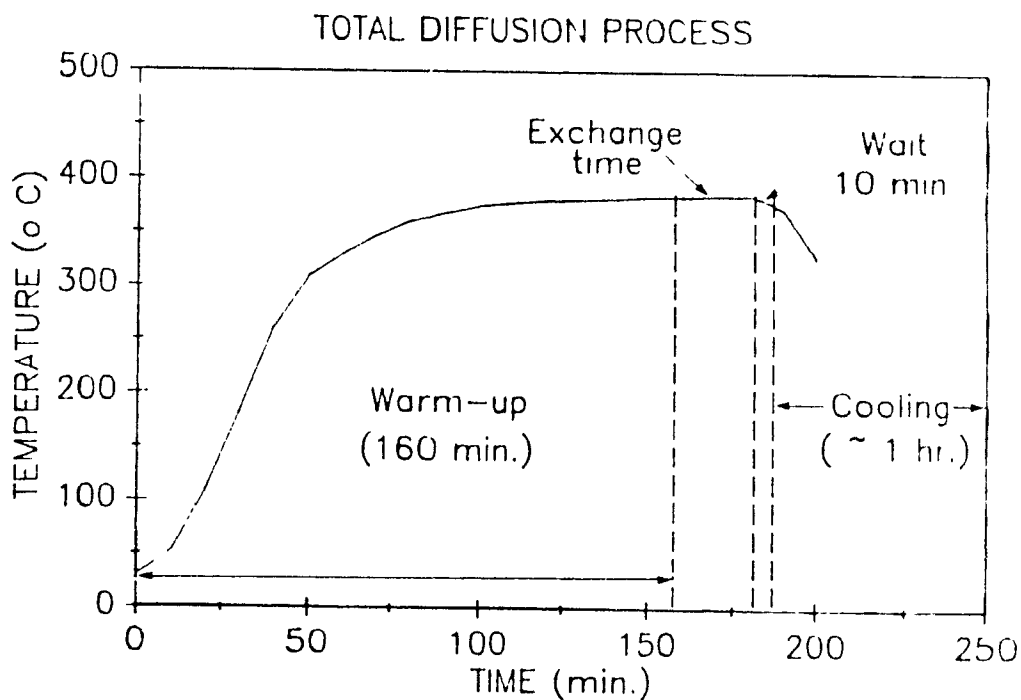


Figure 4.5. Electric field-assisted diffusion process

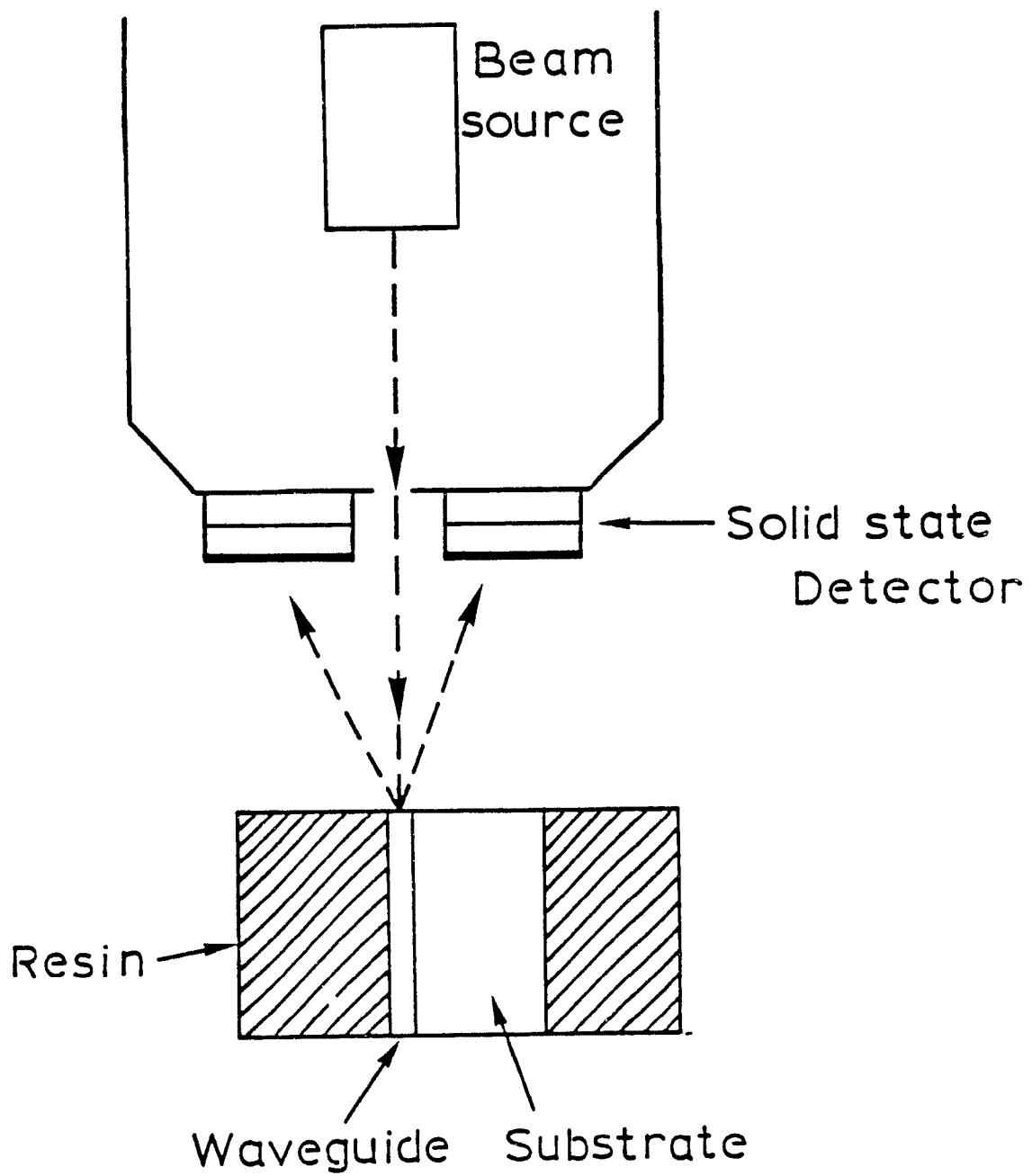


Figure 4.6: Diagram showing SEM method used to determine potassium concentration profile in ion-exchanged waveguides

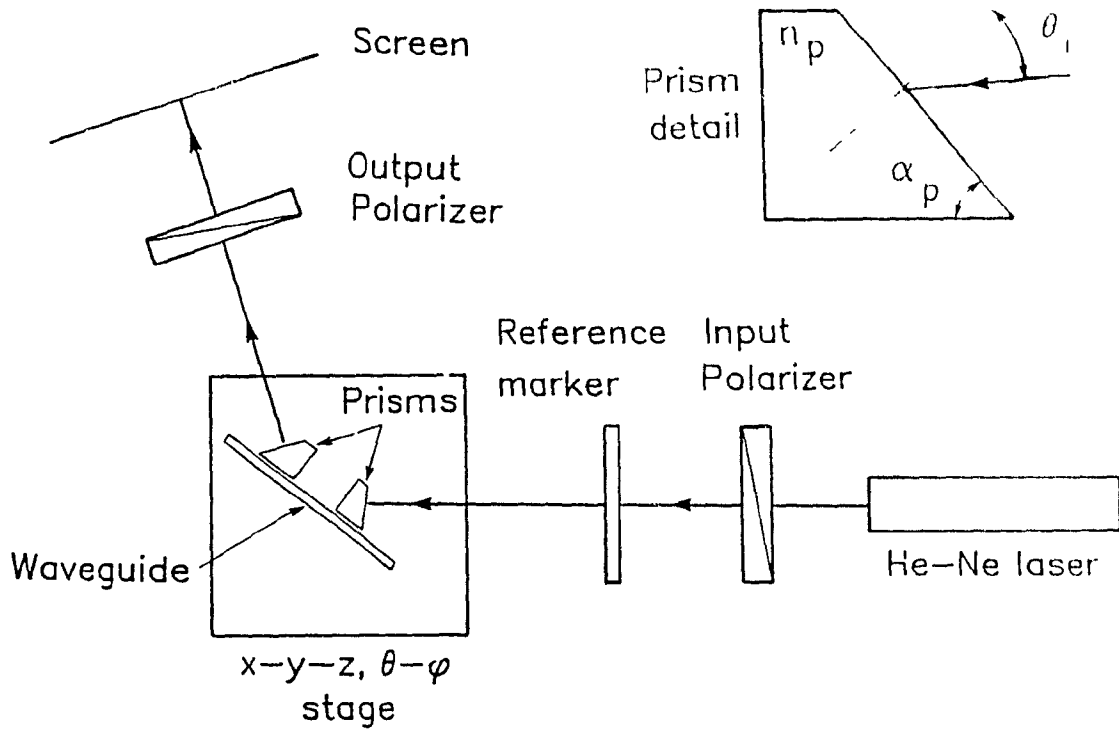


Figure 4.7: Experimental setup for measuring the effective mode indices



Figure 4.8: Photograph of the m-lines from a multi-mode waveguide

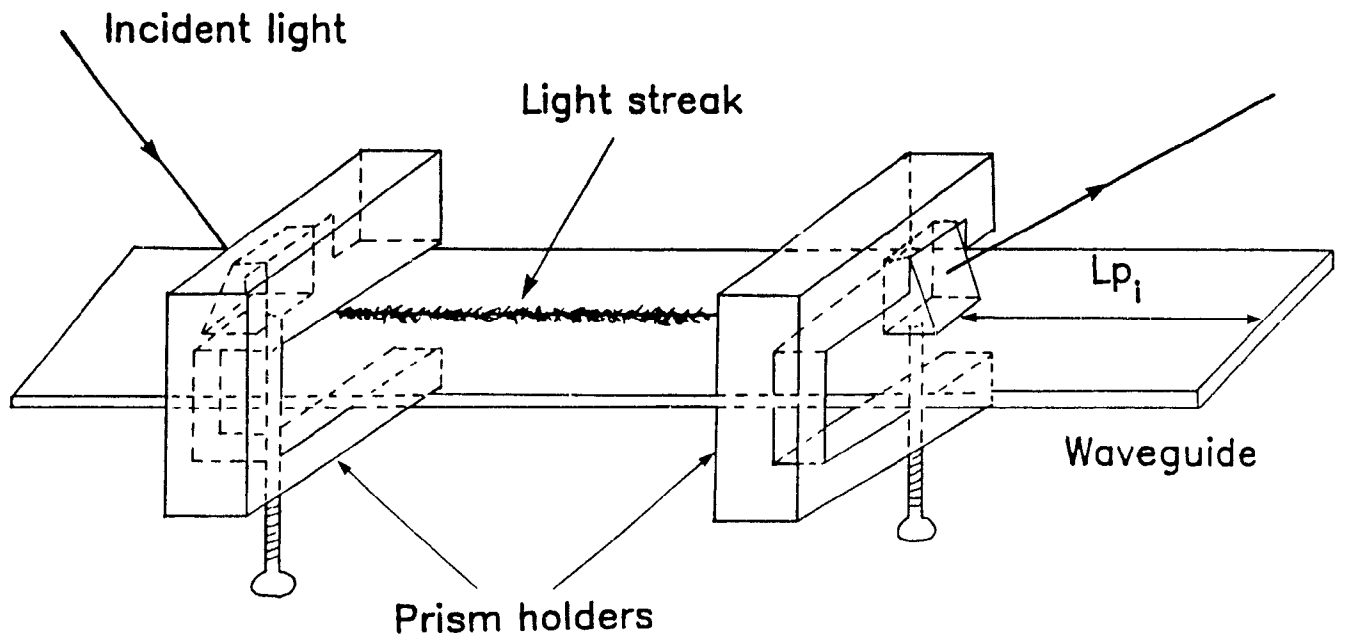


Figure 4.9: Prism position measurement for measuring the propagation losses

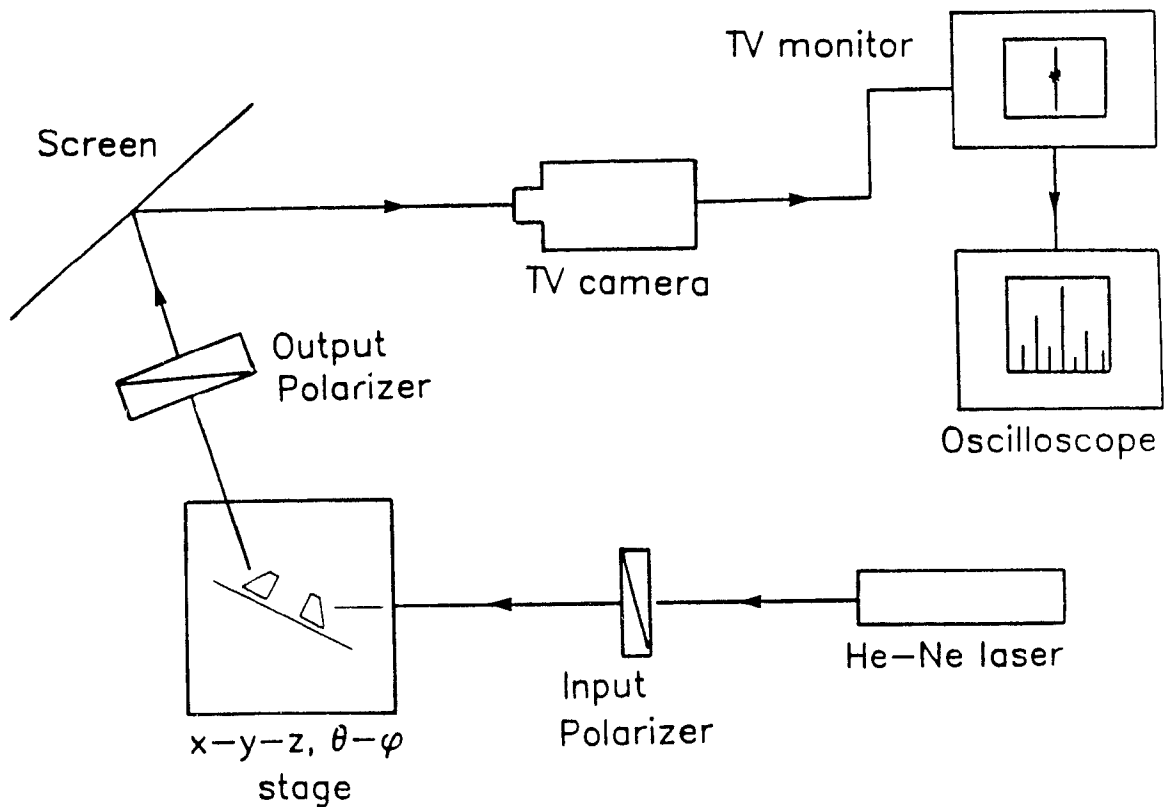


Figure 4.10: Experimental setup for measuring the propagation losses

## Chapter 5

# Purely thermal buried waveguide characterization

### 5.1 Introduction

In this chapter, the theoretical modeling and experimental characterization of the purely thermal waveguides are presented. The diffusion characteristics, such as the  $K^+$ -ion concentration profile, are correlated to the experimental SEM and EPMA data. These parameters are then used to determine the propagation characteristics, such as the dispersion curves, which are compared to the effective mode index measurements.

Buried waveguides have been demonstrated and characterized using a two-step electric field-assisted ion-exchange in glass for silver ions [66] and more recently, for potassium ions [9]. Purely thermal silver [67] and thallium [68] ion-exchange has been used to fabricate buried waveguides. However, the demonstration of such buried guides using purely thermal migration of  $K^+$  ions in glass is still lacking. In this section, we report a procedure for fabricating shallow buried waveguides in soda-lime glass using a purely thermal backdiffusion process [18]. To our knowledge, this is the first time such waveguides has been demonstrated.

## 5.2 SEM and EPMA results

Using the microanalytical methods described in Chapter 4, the potassium ion concentration profiles are shown in Fig. 5.1(a) and (b). The resin compound (the left-hand side) shows negligible BSE contribution, the  $K^+$ -ion profile (the right-hand side) gives an indication of the refractive index change in the glass. Note that at the interface of Fig. 5.1(a), the signal is slightly shifted to the right of the resin-glass interface. This is possibly caused by the slow response time of the signal due to the abrupt change in the yield of BSE in going from the resin to the glass. For the buried waveguide in Fig. 5.1(b), the kink in the signal near the interface represents the potassium concentration which is at the same level as that in the bulk.

Buried waveguides were successfully fabricated at  $T_1 = 360^\circ C$  and  $T_2 = 440^\circ C$  for various  $t_1$  and  $t_2$ . Other fabrication conditions were attempted at ( $T_1 = 385^\circ C$  :  $T_2 = 385^\circ C$ ) and ( $T_1 = 385^\circ C$  :  $T_2 = 425^\circ C$ ). However, buried profiles were not obtained, their SEM signatures resembled those of surface waveguides, as shown in Fig. 5.1(a). The demonstration of these buried guides is contrary to some researchers' report that the  $K^+$  ions do not diffuse out because the potassium is held rigidly to the glass matrix [17]. We believe that the originally compressed surface waveguide approaches its annealing point [24], close to the higher temperature of  $440^\circ C$  during backdiffusion, so that the internal stresses are relaxed, permitting  $K^+$  to be replaced by  $Na^+$  more readily. Further investigation of this point is needed.

Furthermore, a quantitative electron microprobe analysis [60] was conducted to determine the  $K_2O$  and  $Na_2O$  concentrations just at the samples' surface. Table 5.1 shows the chemical compositions of a Fisher substrate glass slide, a surface guide, and a buried sample. For the surface guide, the weight percent of  $K_2O$  is higher than that of  $Na_2O$ , while for the buried waveguide, the weight percent of  $Na_2O$  is higher. Hence, this analysis confirms the BSE-SEM data near the buried

waveguide surface, where low  $K_2O$  and high  $Na_2O$  values are obtained. Contrary to the results of Gortych and Hall [14], a significant outdiffusion of  $Ca^{2+}$  and  $Mg^{2+}$  was not observed. Our analysis shows that the  $K^+ - Na^+$  exchange dominates in soda-lime glass (see Table 5.1).

For comparison, the numerical solution of the diffusion equation with scaled SEM data for a buried guide is shown in Fig. 5.2. The agreement is excellent at  $x_{peak}$  and beyond but not so accurate within  $2 \mu m$  of the edge. This discrepancy may be due to the rounding of the sample edge during polishing.

### 5.3 Diffusion characteristics

Buried waveguide profiles can be determined accurately by the numerical procedure outlined in 2.3.3. In this modeling, the first exchange concentration profile is used as the initial condition for backdiffusion. In the first diffusion at  $T_1 = 360^\circ C$ , the value of  $D_K(TE) = D_e(TE) \cdot 4(1.17)^2 = 0.323 \mu m^2/hr$  [4] and we use the available data for  $\hat{\alpha} = 0.898$  at  $374^\circ C$  even though our working temperature is a little lower. In the backdiffusion process at  $T_2 = 440^\circ C$ , the value of  $D_K(TE) = 4.391 \mu m^2/hr$ , however, there was some doubt about using the available value of  $\hat{\alpha} = 0.898$  at this temperature. Hence, a four-mode waveguide was fabricated at  $440^\circ C$  for 281 minutes and its TE effective mode indices ( $N_e$ ) were measured. Then, by using the well-known WKB dispersion relation for a Gaussian profile, the turning points,  $x_t$ , were determined for each measured  $N_e$  by [11]

$$x_t = d \sqrt{-\ln \left( \frac{N_e - n_b}{\Delta n_s} \right)} \quad (5.1)$$

where  $\Delta n_s = n_s - n_b$ ,  $n_s$  and  $n_b$  being the surface and bulk indices, respectively. The value of  $d(TE) = \sqrt{D_e t}$  is  $10.6 \mu m$  while  $\Delta n_s(TE)$  is 0.0084. Now, since the normalized concentration profile is assumed to be equal to the normalized refractive index profile then,

$$\frac{c(x)}{c(0)} = \frac{\Delta n(x)}{\Delta n_s} = \exp(-x^2/d^2) \quad (5.2)$$

where  $\Delta n(x) = n(x) - n_b$ . At the measured effective indices  $N_e = n(x_t)$ , the turning points can be plotted against  $c(x_t)/c(0) = (N_e - n_b)/\Delta n_b$ . In Fig 5.3, these points are shown in comparison with the numerical simulations using  $\hat{\alpha} = 0.898$ . The agreement is excellent and hence,  $\hat{\alpha} = 0.898$  is used in the backdiffusion simulation at  $440^\circ\text{C}$ .

The buried waveguide index profile characteristics can be determined accurately as functions of first exchange time  $t_1$  and backdiffusion time  $t_2$ . By solving the diffusion equation, we find a linear relationship between  $x_{peak}$  and  $\sqrt{t_2}$  as given by

$$x_{peak} = \sqrt{B_e t_2} + K_1 \quad (5.3)$$

where  $t_2$  is in hours,  $B_e$  is the effective backdiffusion coefficient, and  $K_1$  is a constant. Figures 5.4 and 5.5 show the calculated TE results of the dependence of  $x_{peak}$  and  $n_{peak}$  on  $t_2$ , respectively, for  $t_1 = 2$  hr and  $t_1 = 4$  hr., when  $t_2$  varies from 2 to 60 minutes. We find that for  $t_1 = 2$  hr.,  $B_e = 7.22 \mu\text{m}^2/\text{hr.}$  and  $K_1 = 0.58$  while for  $t_1 = 4$  hr.,  $B_e = 6.69 \mu\text{m}^2/\text{hr.}$  and  $K_1 = 0.87$ . This plot clearly establishes a linear relation between  $x_{peak}$  and  $\sqrt{t_2}$ . For the TM modes, the same values of  $B_e$  can be used. This is because the TM diffusion coefficients in the first exchange at  $360^\circ\text{C}$  ( $D_K = 0.298 \mu\text{m}^2/\text{hr.}$ ) and in backdiffusion at  $440^\circ\text{C}$  ( $D_K = 4.524 \mu\text{m}^2/\text{hr.}$ ) [11] are only slightly different from the corresponding TE coefficients and hence, yield similar concentration profiles as for the TE case.

## 5.4 Curve fitting

In order to design buried waveguide devices (using dispersion curves) or to study the efficiency of coupling these guides to an optical fiber, it is convenient if the index profile can be expressed as a simple analytical function. By trying to fit a simple function  $f(x)$  to the  $K^+$ -ion concentration profile, we can express the index variation as

$$n(x) = n_t + \Delta n_e f(x) \quad (5.4)$$

where,  $f(x)$  must satisfy the requirements of a buried profile i.e.  $f(x) = 0$  at  $x = 0$  and at  $x = \infty$ . Knowing that the surface planar waveguide profile is Gaussian [11], we believe that the buried profile should be similar in shape while satisfying the condition at  $x = 0$ . One profile which satisfies these conditions is the Rayleigh distribution

$$f(x) = Ax \exp(-\gamma x^2) \quad (5.5)$$

with the fitting parameters  $A$  and  $\gamma$  dependent on  $t_1$  and  $t_2$ . An example of this profile fitted to the numerical solution is shown in Fig. 5.6, with the SEM data also superimposed. The fit is excellent and hence, the Rayleigh profile is used to describe the refractive index profile of the buried guide. We note that with  $\xi = x/x_{peak}$ , the Rayleigh function can be expressed as

$$f(\xi) = C^2 \xi \exp(-\delta^2 \xi^2) \quad (5.6)$$

where  $C^2 = Ax_{peak}$  and  $\delta^2 = \gamma x_{peak}^2$ . Table 5.2 shows some values of  $A$  and  $\gamma$  calculated with a least square fit [38] for given fabrication conditions  $t_1$  and  $t_2$ , while Figs. 5.7(a) and (b), show the detailed dependence of these parameters on  $t_2$ . We find that for the TM modes,  $A$  and  $\gamma$  were very close to those for the TE case and hence, Figs. 5.4, 5.5 and 5.7 are also good for the TM case.

## 5.5 Dispersion curves and modal fields

The exact method discussed in Chapter 3 was first used to generate dispersion curves of single-mode surface planar waveguides fabricated at 360 °C for various diffusion times ranging from 1-4 hours. These curves were then compared to the WKB dispersion plots in the single-mode region using  $\Delta n_s(TE) = 0.0092$  and  $\Delta n_s(TM) = 0.0113$ , as shown in Figs. 5.8(a) and (b). The comparison is quite good except close to the  $TE_c$  and  $TM_c$  cutoff values. Furthermore, three single-mode surface guides were fabricated at  $t_1 = 1, 2,$  and  $4$  hr. and their effective indices compared well with the theoretical values.

The effective indices of the single-mode buried waveguides were calculated and plotted against  $t_2$ , for both TE and TM modes, and the theoretical dispersion curves were compared with the measured data, as shown in Figs. 5.9(a) and (b). The agreement seems quite good. The measured mode indices are presented in Table 5.3. The discrepancies between theory and experiment were calculated for each of the 14 measured indices and the average of these was found to be

$$|N_e(\text{meas.}) - N_e(\text{theo.})| = (1.4 \pm 1.3) \times 10^{-4}$$

with the largest deviation being  $5 \times 10^{-4}$ . Hence, the simple Runge-Kutta technique with the Rayleigh index profile, characterized for  $t_1$  and  $t_2$ , provides a good model for predicting the propagation characteristics of buried planar waveguides.

From our measurements and numerical modeling, we observed two important effects of the purely thermal backdiffusion process:

1. A decrease of the effective index with an increasing time  $t_2$
2. A decrease of the birefringence ( $N_e(TM) - N_e(TE)$ ) with an increasing  $t_2$

The first effect can be explained on physical grounds. Starting with a surface waveguide ( $\Delta n_s = 0.0092$ ), the value of the surface index change  $\Delta n_s$  decreases rapidly with increasing  $t_2$ . This was shown previously in Fig. 5.5, where the  $n_{\text{peak}}$  decreased with ascending  $t_2$ . Now, since  $N_e$  is directly proportional to  $\Delta n_s$ , we can see that as  $t_2$  increases,  $N_e$  will decrease. The effect of decreasing birefringence may be explained as follows. It is known that the origin of the birefringence in  $K^+ - Na^+$  waveguides is due to stress-induced surface effects [13]. We believe that the higher temperature in backdiffusion leads to stress relaxation in the waveguide, thus decreasing the birefringence as backdiffusion progresses. Hence, the TE and TM mode propagation constants begin to equalize as the backdiffusion time increases. This finding may be useful to fabricate single-mode polarization insensitive waveguide devices which have attracted recent interest for improving the characteristics of  $1 \times N$  branching couplers in glass [69].

The numerical model is also useful for deducing the modal fields  $E_y$  and  $H_y$  as functions of  $\xi$ . These field distributions are needed in overlap integral calculations of coupling efficiency so as to determine the insertion loss between optical fibers and buried waveguides. Such plots are quite useful in computing the field width,  $W_f$ , defined as the width at which the field amplitude reduces to  $1/e$  of its peak value. Figures 5.10(a) and (b) show the index and modal field plots for both a surface and buried waveguide. We find that field depths of the buried guides are greater than those of the surface guides, as expected. Furthermore, we calculated  $W_f$  with varying time  $t_2$  and a square root dependence is found, as shown in Fig. 5.11, indicating a broader field distribution with increasing backdiffusion time. Recently, Ramaswamy *et al.* established a similar square root relation for the index profile width  $W$  (which is proportional to  $W_f$ ) in the case of electric field-assisted Ag<sup>+</sup>-ion exchanged buried waveguides [66].

## 5.6 Single-mode design

As discussed in Chapter 3, a convenient formula can be established to determine the number of guided modes in a planar waveguide given the refractive index profile  $f(x)$ , the depth  $d$  and the maximum index change  $\Delta n_s$ . Using (3.28), at the cutoff condition ( $n(x_t) = N_c = n_b$ ), yields, for a buried Rayleigh profile,

$$x_t \exp(-\gamma x_t^2) = 0$$

so that the turning points,  $x_{t_1} = 0$  and  $x_{t_2} = \infty$ . Using the index profile of (5.5), and knowing that  $\Delta n_s \ll 1$ , we get

$$k_0 \int_0^\infty \sqrt{2n_b \Delta n_s f(x)} dx = (m + \frac{1}{4})\pi + \tan^{-1} \left[ \chi \sqrt{\frac{n_b^2 - 1}{n_s^2 - n_b^2}} \right]. \quad (5.7)$$

For buried planar waveguides with Rayleigh profile  $f(x)$ , the integral relation for the number of guided modes in the guide can be expressed analytically. Using

the definite integral [70]

$$\int_0^{\infty} x^{1/2} \exp(-\gamma x^2/2) dx = \frac{\Gamma(3/4)}{2\sqrt{(\gamma/2)^{3/2}}} = \frac{1.0304}{\gamma^{3/4}}$$

the expression for the number of guided modes becomes

$$m = INT \left\{ \frac{2\sqrt{2n_b \Delta n_s A}}{\lambda_o} \frac{1.0304}{\gamma^{3/4}} - \frac{1}{\pi} \tan^{-1} \left[ \chi \sqrt{\frac{n_b^2 - 1}{n_s^2 - n_b^2}} \right] - \frac{1}{4} \right\} \quad (5.8)$$

This formula is quite useful for designing buried single-mode waveguides given the fitting parameters  $A$ ,  $\gamma$  and the index parameters  $n_b$ ,  $\Delta n_s$ . Note that  $\Delta n_s(TE) = 0.0092$  and  $\Delta n_s(TM) = 0.0113$ . This design formula is verified for all the fabricated TE and TM mode buried waveguides in Table 5.4 with excellent agreement.

## 5.7 Propagation losses

A main attraction of buried optical waveguides is their promise of lower scattering losses. This is due to the minimal interaction of the propagating field with surface irregularities that invariably contribute to losses via scattering [5]. These losses were measured for one surface guide and three buried guides and the results are presented in Table 5.5. We observed that the backdiffusion process increases the losses. This phenomenon can be explained by considering surface stresses. It seems that during backdiffusion, the out-diffusion of  $K^+$  ions induces tensile stresses which may be promoting crack formation in the originally compressed surface guide [71]. Our measurements of the buried guides indicate that these stresses may be causing the increase in scattering losses. Furthermore, these crack formations were observed in SEM micrographs of the ion-exchanged glass surface, as shown in Fig. 5.12. Clearly, deformations in the microstructure are apparent in the buried guide (Fig. 5.12(b)), while the surface guide (Fig. 5.12(a)) showed no damage. Thus, these results confirm the propagation loss measurements and we believe these findings are important to consider in the fabrication of single-mode  $K^+$  buried waveguide devices. If  $t_2$  is too long, the waveguide may be too lossy for practical application.

The present analysis suggests that a low-loss buried waveguide can be achieved by backdiffusing for a short period of time (less than 20 minutes).

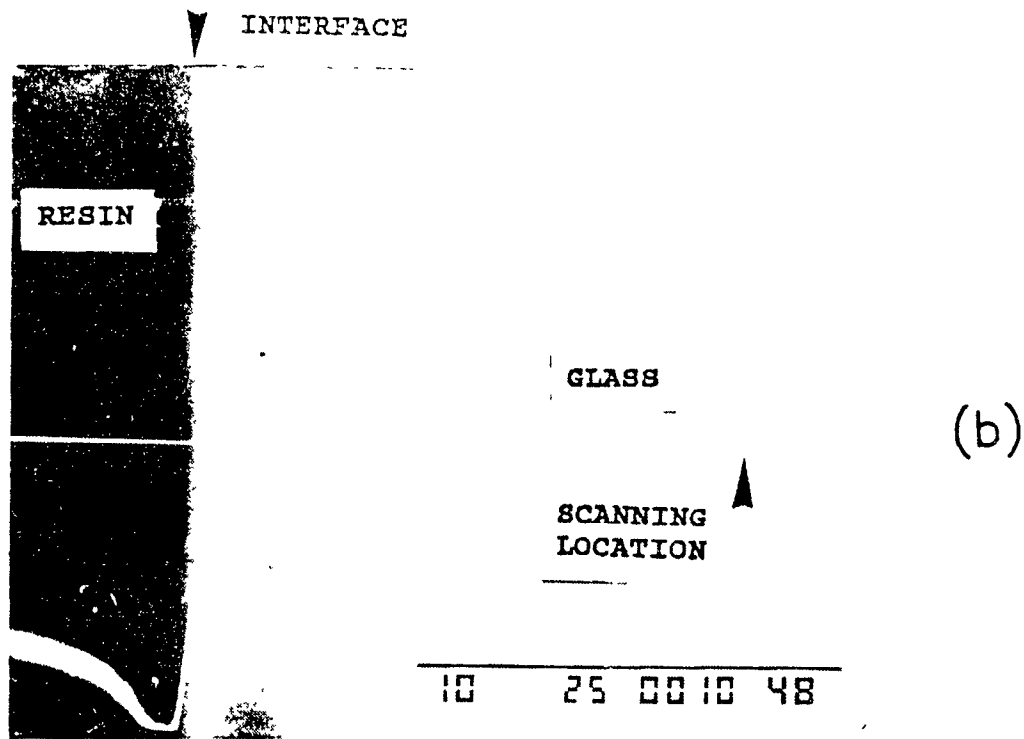
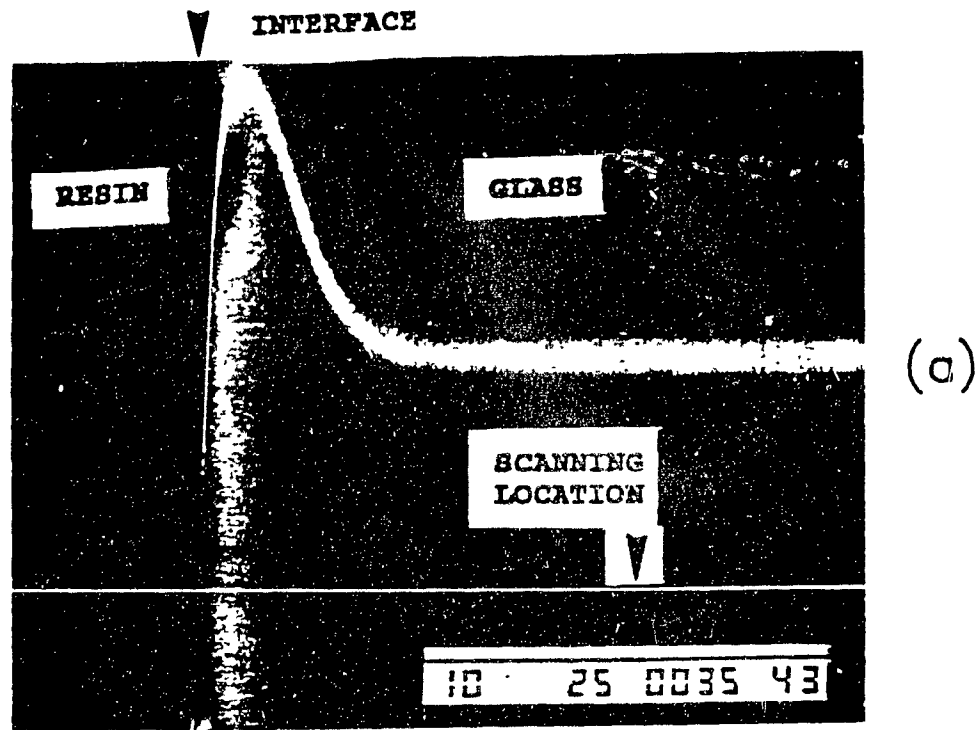


Figure 5 1 SEM photographs of (a) surface waveguide ( $10,000\times$ ),  $t_1 = 2.0$  hr.,  $T_1 = 360^\circ C$  and (b) buried waveguide ( $5000\times$ ),  $t_1 = 2.0$  hr.,  $T_1 = 360^\circ C$ ,  $t_2 = 0.5$  hr.,  $T_2 = 440^\circ C$

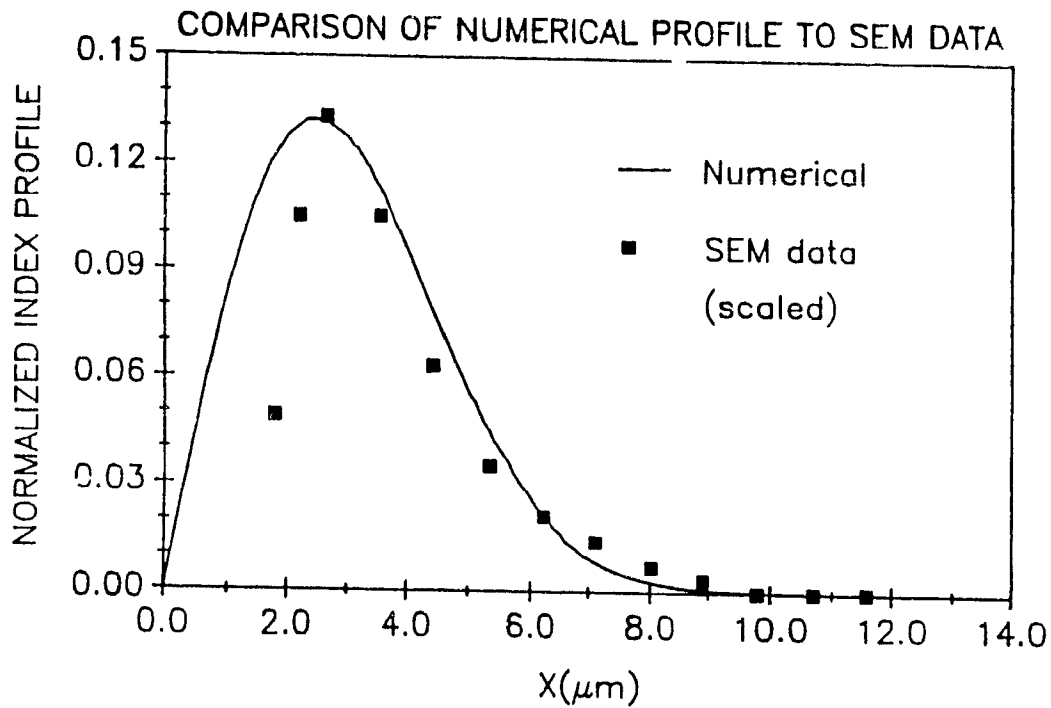


Figure 5.2: Comparison of the numerical solution to the scaled SEM data of the buried guide in Fig 5.1(b)

Oxide	Substrate glass (weight %)	Surface guide (weight %)	Buried guide (weight %)
$SiO_2$	72.31	69.93	72.00
$Na_2O$	14.33	4.35	13.24
$K_2O$	1.21	13.60	1.31
$CaO$	6.44	6.14	6.25
$Al_2O_3$	1.22	1.36	1.46
$MgO$	4.31	4.09	4.17

Table 5.1: Quantitative electron microprobe analysis of a soda-lime glass substrate, a surface waveguide, and a buried waveguide

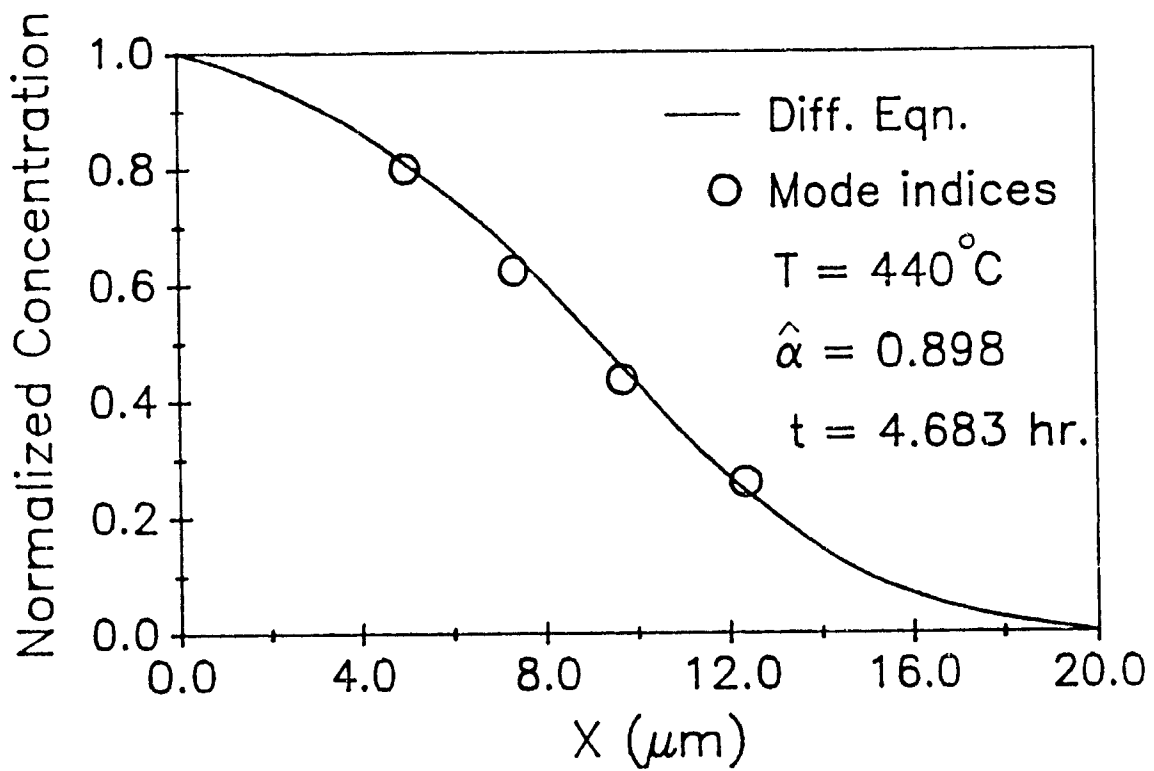


Figure 5.3: Comparison of the numerical simulation of the diffusion equation to the measured mode indices using  $\hat{\alpha} = 0.898$  at  $T = 440^{\circ}\text{C}$

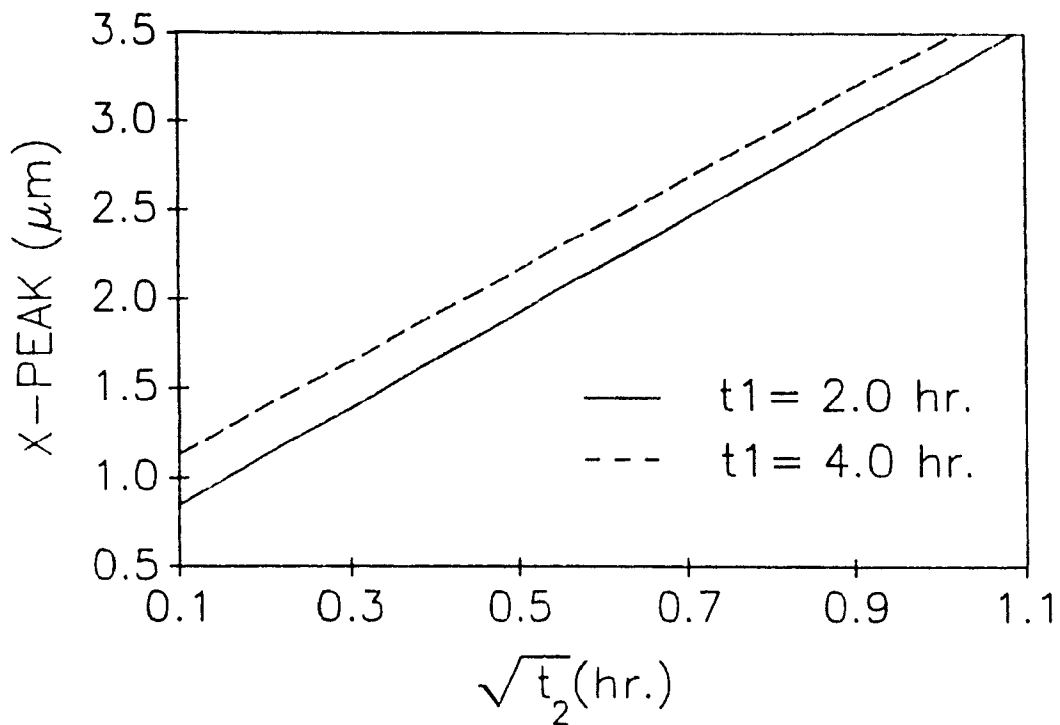


Figure 5.4: Square root dependence of  $x_{peak}$  with  $t_2$  for  $t_1 = 2$  and 4 hr.

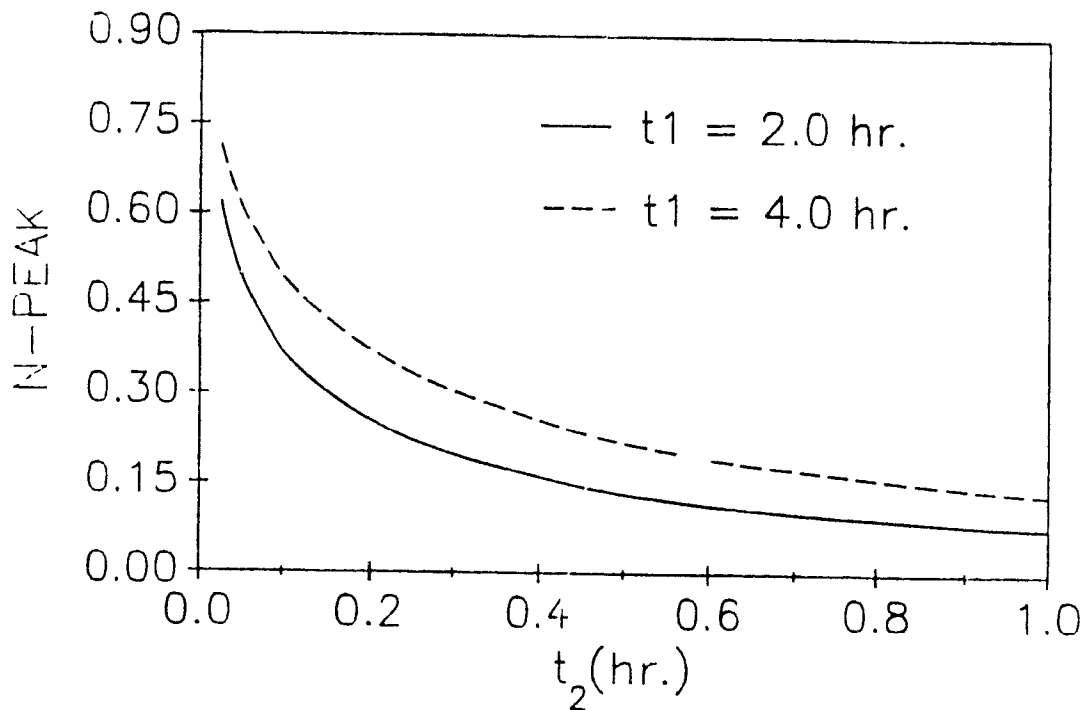


Figure 5.5: Variation of  $n_{peak}$  vs  $t_2$  for  $t_1 = 2$  and 4 hr.

$t_2(\text{min.})$	$t_1 = 2\text{hrs.}$		$t_1 = 4\text{hrs.}$	
	$A$	$\gamma$	$A$	$\gamma$
6	0.430	0.237	0.486	0.163
15	0.196	0.140	0.260	0.106
30	0.090	0.083	0.136	0.069
45	0.055	0.060	0.090	0.053

Table 5.2: Fitting parameters  $A$  and  $\gamma$  related to  $t_2$

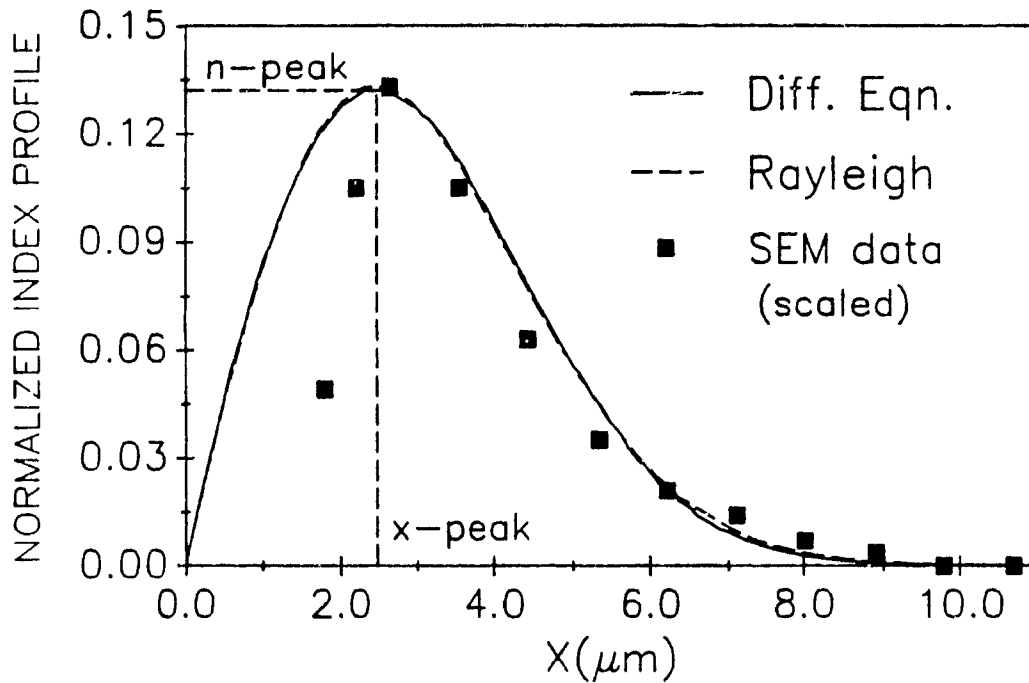


Figure 5.6: Rayleigh profile fitted to the numerical simulation of diffusion equation with superimposed SEM data for ( $t_1 = 2$  hr. :  $t_2 = 30$  min.)

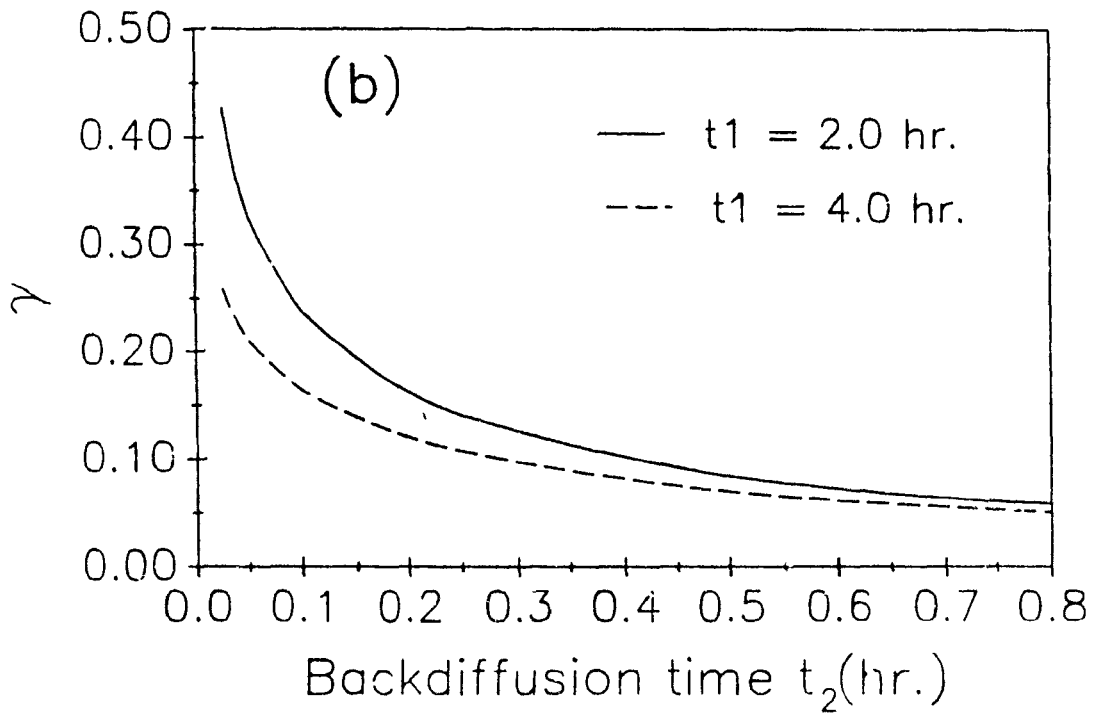
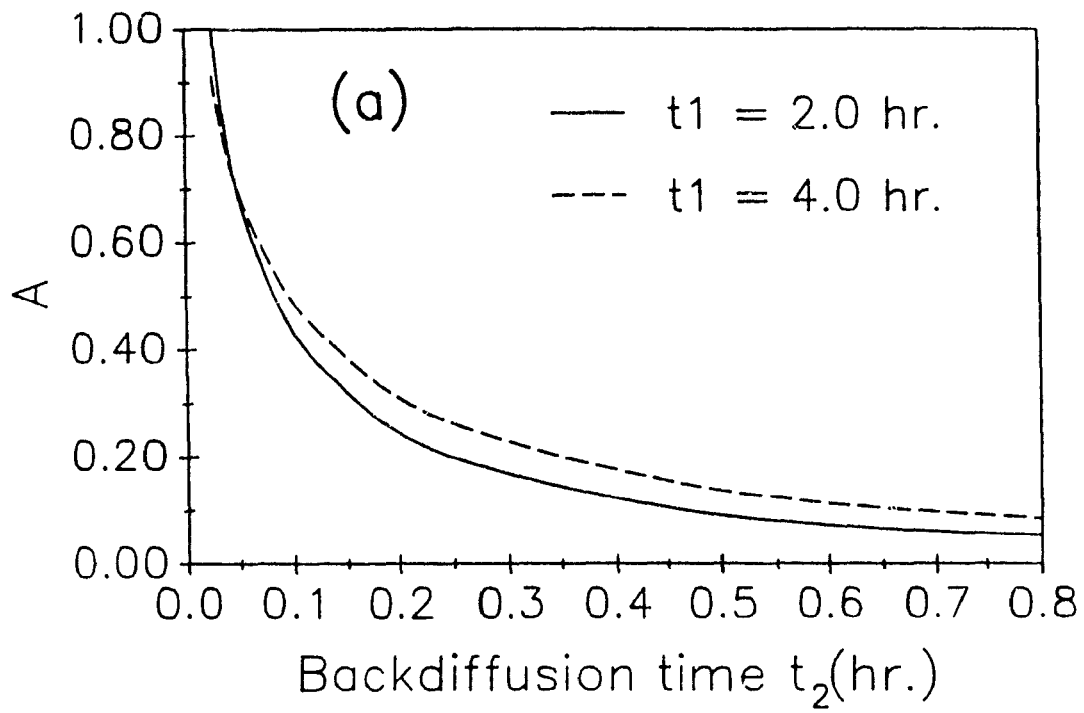


Figure 5.7: Plot of (a)  $A$  and (b)  $\gamma$  vs.  $t_2$  for  $t_1 = 2$  and 4 hr.

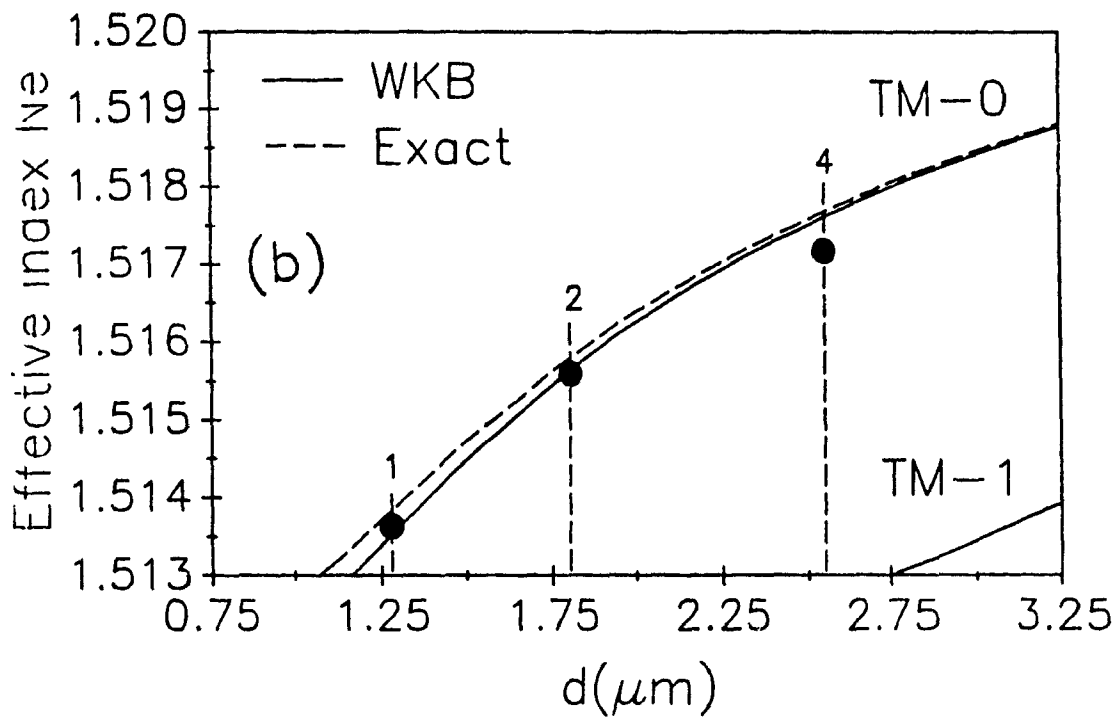
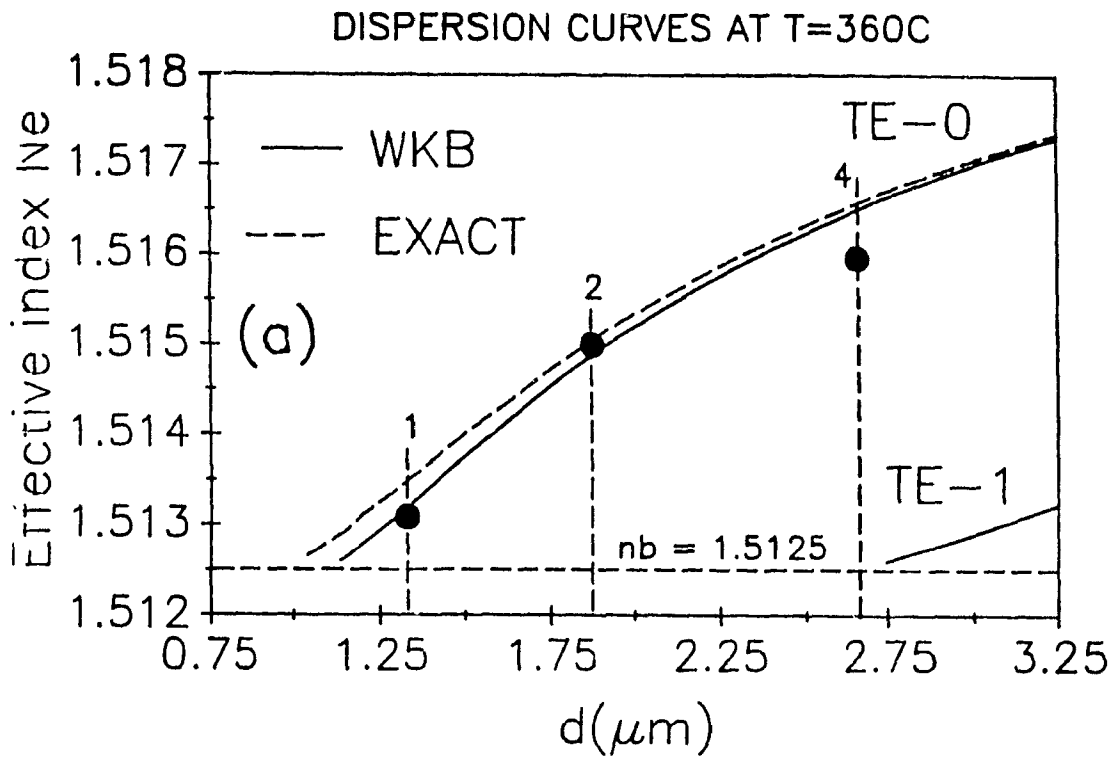


Figure 5.8: Theoretical dispersion curves (WKB and exact) of the guided modes compared with measured indices for samples prepared at  $T = 360^\circ\text{C}$  for a Gaussian profile (times in hrs.) (a)  $TE_0$ , (b)  $TM_0$ .

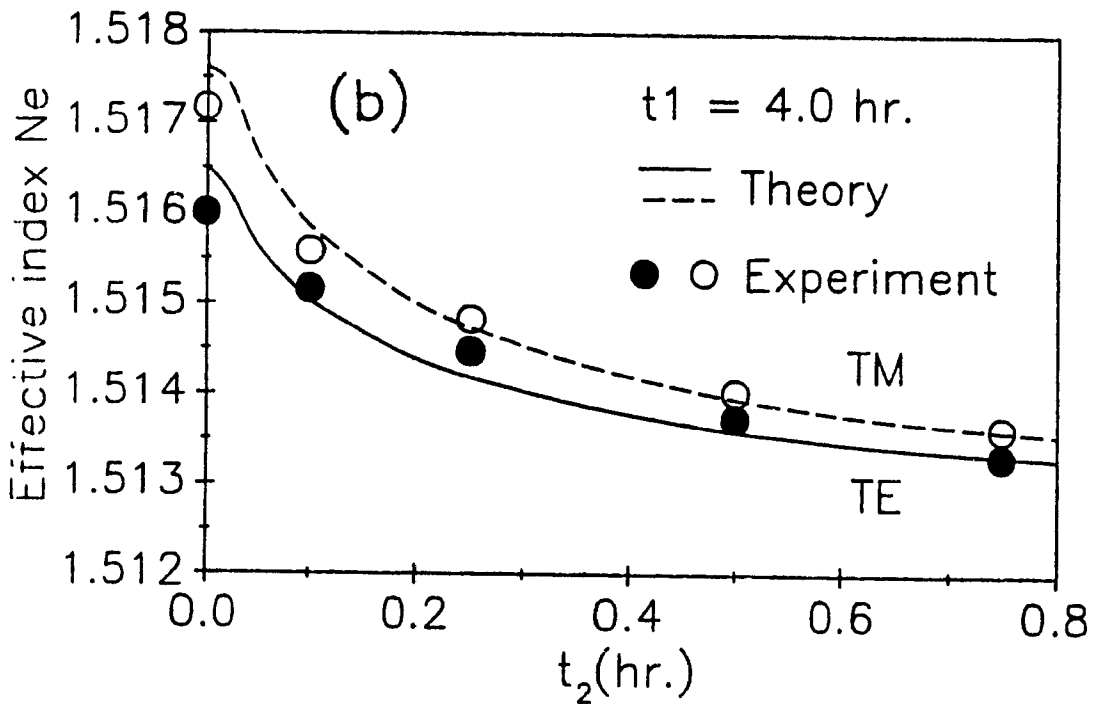
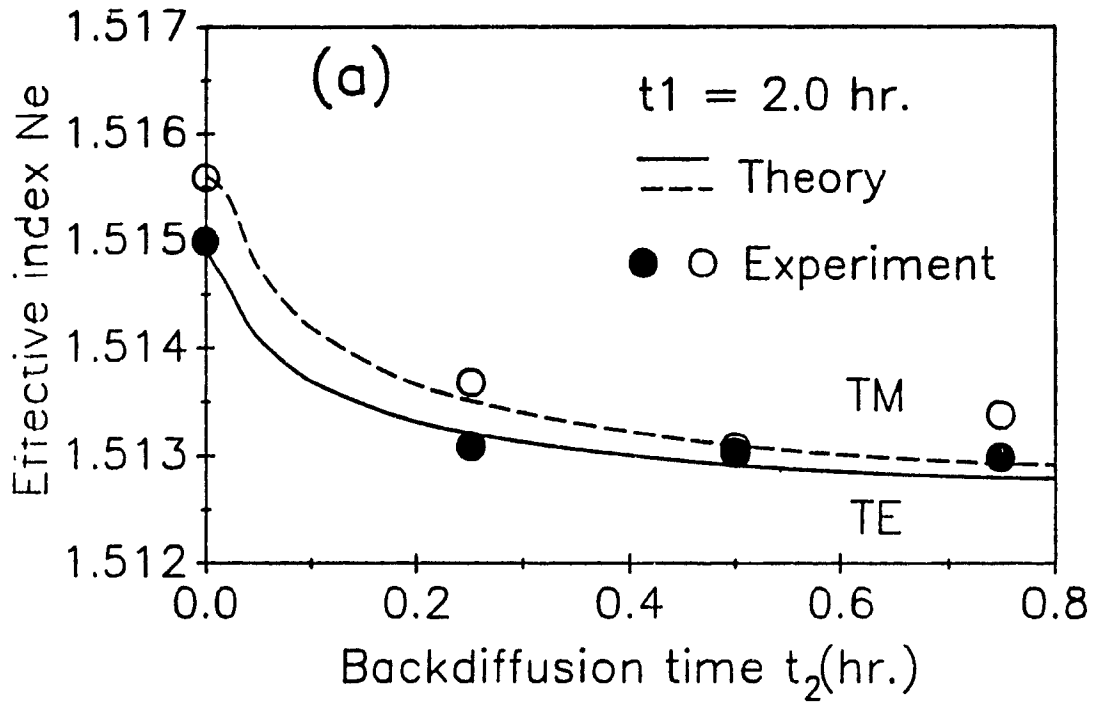


Figure 5.9: Theoretical dispersion curves (Rayleigh profile) of the guided  $TE_0$  and  $TM_0$  modes compared with measured indices for: (a)  $t_1 = 2$  hr. (b)  $t_1 = 4$  hr.

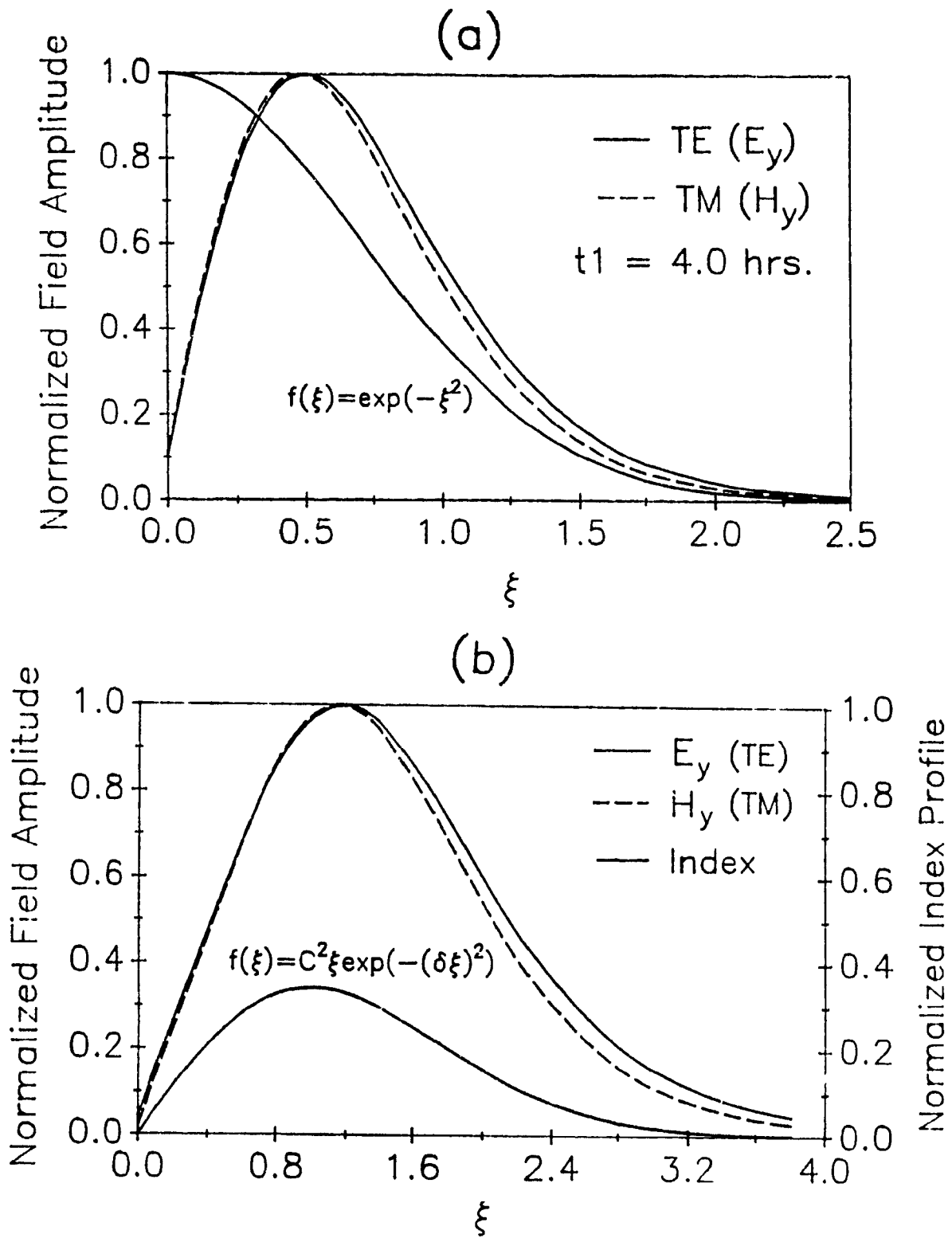


Figure 5.10: Plots of normalized field amplitude as a function of  $\xi$  for  $TE_0$  and  $TM_0$  modes for a: (a) Gaussian profile ( $\xi = x/d$ ): ( $t_1 = 4$  hr.) (b) Rayleigh profile ( $\xi = x/x_{peak}$ ): ( $t_1 = 4$  hr.,  $t_2 = 15$  min.)

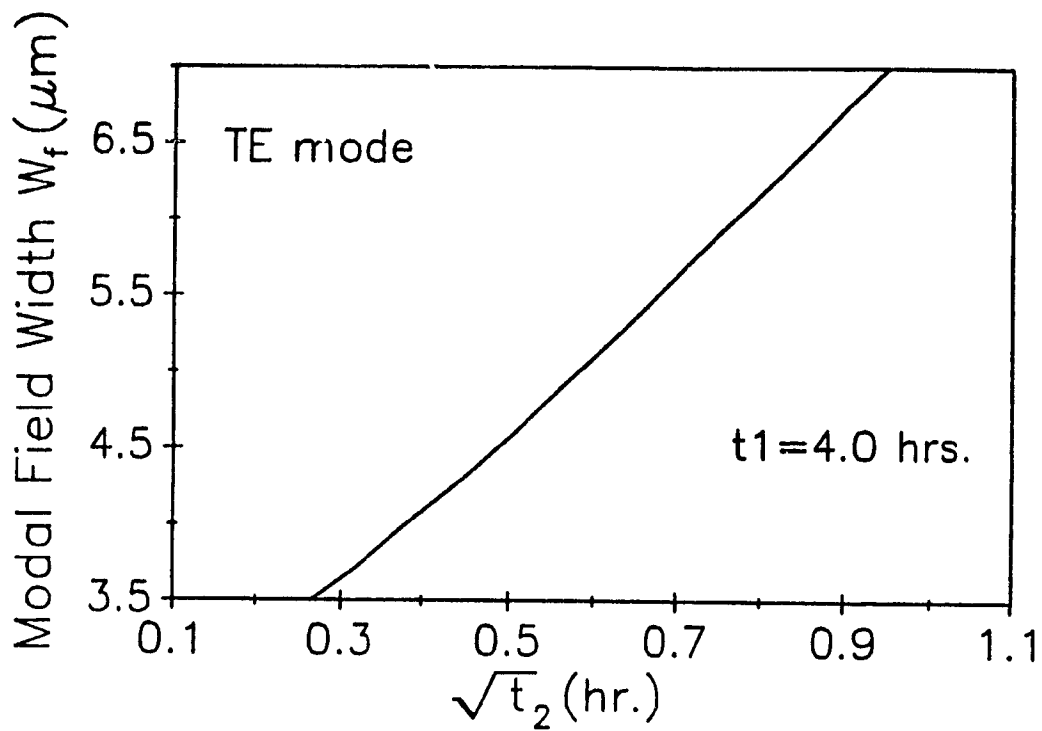


Figure 5.11: Square root dependence of modal field width  $W_f$  with  $t_2$

Wvg. #	$t_1$ (hr.)	$t_2$ (min.)	$N_e$ (TE)	$N_e$ (TM)
57	2.0	15.0	1.5131	1.5137
70A	2.0	30.0	1.5130	1.5131
61	2.0	45.0	1.5130	1.5134
66	4.0	6.0	1.5152	1.5156
62	4.0	15.0	1.5145	1.5148
63	4.0	30.0	1.5137	1.5140
64	4.0	45.0	1.5133	1.5136

Table 5.3: Measured TE and TM single mode effective indices

Wvg. #	$x_{peak}$ ( $\mu m$ )	$C$	$\delta$	arg. (TE)	arg. (TM)	$m =$ $INT(arg.)$
57	1.875	0.606	0.701	0.35	0.44	1
70A	2.475	0.471	0.715	0.34	0.43	1
61	2.925	0.420	0.686	0.47	0.57	1
66	1.725	0.915	0.696	0.77	0.91	1
62	2.175	0.751	0.709	0.78	0.92	1
63	2.700	0.605	0.709	0.78	0.92	1
64	3.075	0.526	0.705	0.78	0.92	1

Table 5.4: Single-mode design parameters

$t_2$ (min.)	Loss (dB/cm)	Type
0	1.0	Surface
15	0.7	Buried
30	2.4	Buried
45	4.0	Buried

Table 5.5:  $TE_0$  propagation loss measurements ( $t_1 = 4$  hr.)

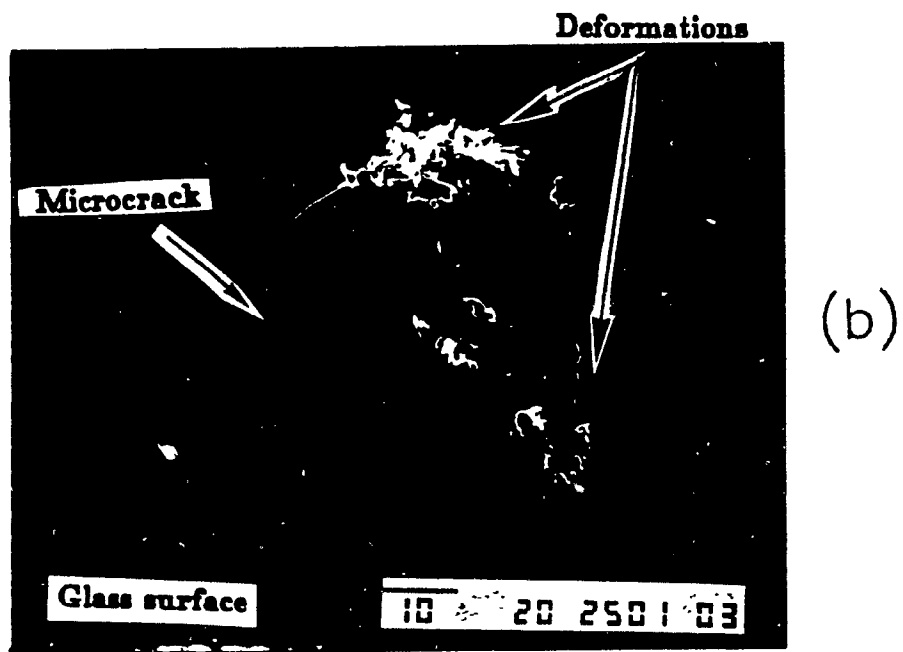
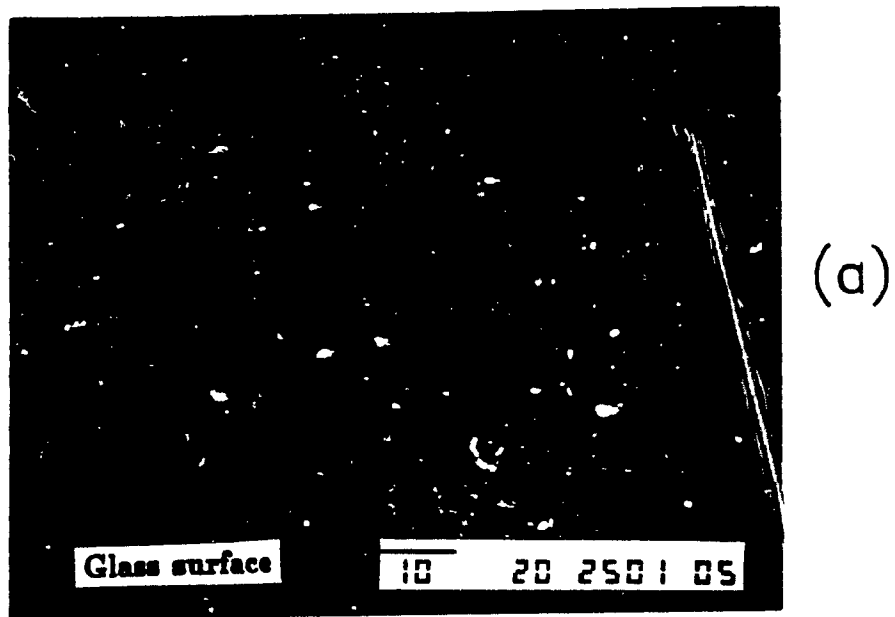


Figure 5.12: SEM photos of microdeformations in  $K^+$ -ion exchanged glass surfaces after backdiffusion in  $NaNO_3$  ( $t_1 = 4$  hr.) : (a)  $t_2 = 0$  min. (b)  $t_2 = 45$  min.

# Chapter 6

## Field-assisted surface waveguide characterization

### 6.1 Introduction

In this chapter, the theoretical modeling and experimental characterization of the electric field-assisted surface waveguides are presented. The propagation characteristics, such as the refractive index profile and dispersion curves, are determined and compared to the effective mode index measurements. Parallel to this, the diffusion characteristics, such as the  $K^+$ -ion mobility and concentration profile, are correlated to the experimental SEM data.

### 6.2 Propagation characteristics

#### 6.2.1 Background

The electric field-assisted ion-exchange has been shown to have advantages over the thermal exchange owing to the drastic reduction in the diffusion time. It is also possible to obtain various refractive index profiles [16], including the step profile [15,30], in planar waveguides. Furthermore, this exchange has been used in a two-step process for the fabrication of deep, buried waveguides made by  $Ag^+$ -ion exchange [72,73] which are attractive in the design of passive devices optimized for efficient coupling with optical fibers. The field-assisted  $K^+$ -ion exchange was previously studied for chemical strengthening in commercial glass [56]. This process

has led to low-loss planar and channel buried waveguides in soda-lime and BK7 glass [9] and reproducible directional couplers [74]. Recently, this technique has also shown promise in the demonstration of integrated optic lasers on neodymium doped soda-lime glass [75].

However, a detailed characterization of the planar waveguide properties such as the effective field-dependent diffusion coefficient, guide depth and index change in soda-lime glass is lacking. Here, we report our experimental results of these characteristics for TE and TM modes and establish simple formulas for this coefficient and waveguide depth [21]. These relations would be useful in the design of passive devices which use field-assisted  $K^+$ -ion exchange waveguides as basic structures.

The characterizations of the purely thermal migration of  $Ag^+$  ions [60] and  $K^+$  ions [11] in glass yielded a square root dependence between the waveguide depth  $d$  and the diffusion time  $t$ , as given by

$$d = \sqrt{D_e t}, \quad (6.1)$$

where  $D_e$  is the effective diffusion coefficient dependent on temperature  $T$ . For example at  $T = 385^\circ C$ ,  $D_e(TE) = 0.0649 \mu m^2/min.$  and  $D_e(TM) = 0.0637 \mu m^2/min.$  for  $K^+$  ions in soda-lime glass [11]. However, for the electromigration of silver [42,45] and potassium ions [9,30], several researchers have found a linear relationship between  $d$  and  $t$ . In particular, for low values of the total applied electric field  $E_a^T$ , the diffusion term can not be ignored. For  $Ag^+$  ions, Ramaswamy *et al.* found that a linear combination of the diffusive and electromigrative terms [Eq. (12) of [42]] was more suitable for expressing the guide depth. Here, a similar approach is taken for the case of constant electric field-assisted  $K^+$ -ion exchange. Therefore,

$$d = \sqrt{D_e t} + F_e t + K_o, \quad (6.2)$$

where  $F_e$  is defined as the effective field-dependent coefficient and  $K_o$  is a constant depth value. This coefficient is linearly proportional to applied field  $E_a^T$  so that

$$F_e = A_1 E_a^T \quad (6.3)$$

and  $A_1$  is a constant which is related to the mobility of  $K^+$  ions in the glass. The importance of establishing relations (6.2) and (6.3) is that, given the fabrication conditions  $(E_a^T, t, T)$  for a waveguide, one can easily determine the guide depth without the need for further measurements.

### 6.2.2 Experimental observations

To fabricate the waveguides, the glass substrates were placed between symmetrical stainless steel half-cells isolated by Teflon seals in a container, as shown in Fig. 4.4. Potassium nitrate crystals were placed in small steel containers suspended just over the half-cells. Once the furnace reached equilibrium at  $T = 385^\circ C$ , the melt was then poured into the anode and cathode cells and a constant voltage was applied across the sample. Electric fields  $E_a$  and diffusion times ranged from 5.3 to 52.1  $V/mm$  and 2 to 20 minutes, respectively. To overcome the preliminary difficulties of substrate cracking, the samples remained in the furnace for an additional 10 minutes before cooling in air. We observed that the ionic current decreased sharply to about one-half its initial value in the first minute of diffusion and then decayed exponentially with diffusion time, as reported by Urnes and more recently by Miliou *et al.* Furthermore, when the applied voltage was removed and the two half-cells short-circuited through a voltage meter, an average value of 1.3V was measured for all the samples. This battery effect was also observed by previous researchers [76] suggesting that space charge effects are present in the glass. This potential drop across the sample was included in the analysis as a local field  $E_o$  which should be considered in the total applied field  $E_a^T = E_a - E_o$ , especially for waveguides fabricated with low field strengths.

### 6.2.3 Data reduction and dispersion curves

From the measured effective mode indices, presented in Tables 6.1 (a) and (b), the refractive index profile can be deduced. We have chosen a direct, statistical

approach that involves *a priori* knowledge of this profile [11]. The crux of the method lies in finding a suitable refractive index profile for which a solution to the dispersion relations (3.16) yields effective indices that fit as closely as possible to the measured ones. The choice of the profile is based on ion-exchange theory and is justified by the successful reproduction of the measured data in comparison to the theoretical curves. Another popular approach is an inverse method, known as the Inverse WKB method [77], which involves reconstruction of the index profile from the modal measurements. This method is only accurate when many modes are measurable.

The refractive index (concentration) profile of constant applied current [30] and constant applied electric [9,56] field-assisted  $K^+$ -ion exchange planar waveguides was found to be step-like and in the former case, this step-index model was used to generate dispersion curves. Although this may be suitable for waveguides fabricated by either high current or electric field exchange, it may not yield accurate results for the lower field strengths used in our experiments. For reasons discussed in Chapter 2, we used a modified Fermi index distribution [78] which was previously used to model glass waveguides made by  $Tl_2SO_4$  ion-exchange. The profile is modified to accommodate the fact that  $f(0) = 1$  for surface waveguides. The index profile

$$n(x) = n_b + \Delta n_s \left[ 1 - \exp\left(-\frac{d}{a}\right) + \exp\left(\frac{x-d}{a}\right) \right]^{-1}, \quad (6.4)$$

where  $\Delta n_s = n_s - n_b$ ,  $n_s$  is the surface index and  $a$  is a fitting parameter associated with the shape of the profile. This shape is illustrated in Fig. 6.1 for typical values of  $a$ . The effective guide depth  $d$  is such that  $n(d) = n_b + \Delta n_s / [2 - \exp(-d/a)]$ . In our experiments, it was found that  $d/a$  ranged from about 4 to 23 and  $\exp(-d/a) \ll 1$ , so that the guide depth occurs close to the half-point of the profile.

The WKB dispersion relation for graded-index profiles (3.16) was used with the characteristic equation for the  $m$ th mode being

$$k_0 \int_0^{z_1} \sqrt{n^2(x) - N_e^2} dx = \left(m + \frac{1}{4}\right) \pi + \phi_s, \quad m = 0, 1, 2, \dots \quad (6.5)$$

Letting  $\varepsilon = \exp(-d/a)$ , so that  $a = -d/\ln(\varepsilon)$ , in (6.4), the profile becomes

$$n(x) = n_b + \Delta n_s [1 - \varepsilon + \varepsilon \exp\left(-\frac{x}{d} \ln(\varepsilon)\right)]^{-1},$$

which, upon defining the normalized variable  $\xi = x/d$ , it becomes

$$n(\xi) = n_b + \Delta n_s [1 - \varepsilon + \varepsilon \exp(-\xi \ln(\varepsilon))]^{-1}. \quad (6.6)$$

At the normalized turning point,  $n(\xi_t) = N_e$  and after some manipulations, we obtain

$$\xi_t = -\ln \left\{ 1 + \frac{n_s - N_e}{\varepsilon(N_e - n_b)} \right\} / \ln(\varepsilon).$$

Also, the depth  $d$  can now be expressed with the help of (6.5) as

$$d = \frac{(m + 1/4)\pi + \phi_0}{k_0 \int_0^{\xi_t} \sqrt{n^2(\xi) - N_e^2} d\xi}. \quad (6.7)$$

To find the unknowns  $n_s$ ,  $d$ , and  $a$ , we started with multimode ( $m > 2$ ) waveguides. This is necessary because this three parameter system needs at least 3 modes to be solved deterministically. Equation (6.7) involves the unknowns  $n_s$  and  $\varepsilon$ . Thus, given any pair of measured mode indices for a waveguide, one can eliminate  $d$  using (6.7) and, for a given value of  $\varepsilon$ ,  $n_s$  can be determined by a root-searching technique in the resulting equation. After this,  $n_s$  and  $\varepsilon$  can be substituted into (6.7) to obtain  $d$ . Applying this procedure repeatedly to all the possible pairs of the mode indices for a particular waveguide sample, one can determine the average values of  $n_s$  and  $d$  of that sample. The best value of  $\varepsilon$  which minimized the deviations of  $n_s$  and  $d$  from their average values was chosen for each waveguide. The profile parameter  $a$  is then determined from  $a = -d/\ln(\varepsilon)$ . For single and two mode waveguides, we used the average values of  $n_s$  and  $a$  from the multimode samples to determine the depth  $d$  using (6.7).

We have observed that the value of the surface index,  $n_s$ , is affected only by the temperature and applied field but is independent of the diffusion time. In addition,  $n_s$  was found to be higher in comparison to that of the purely thermal  $K^+$  exchange

[11]. This index increase may be due to the fact that the electric field induces an increase in the concentration at the surface, as observed for field-assisted  $Ag^+$ -ion exchange [42]. Further investigation of this point is required, but is beyond the scope of this thesis.

For each chosen field, waveguides were prepared with various diffusion times and the average values of  $n_s$  and  $a$  for all the samples was then used to compute the theoretical dispersion curves from the WKB dispersion relation. In Fig. 6.2, these curves are presented together with the experimentally measured data for both polarizations in the samples prepared at  $E_a = 21.1 V/mm$ , respectively. The values of  $n_s$ ,  $d$  and  $a$  for each waveguide are listed in Tables 6.3 and 6.4. Furthermore, these dispersion curves were modeled using a step profile for comparison. Using the exact dispersion relation (3.14), the unknowns  $n_f$  and  $d$  were determined in a similar fashion as  $(n_s, d, a)$ . Table 6.5 and 6.6 lists these values for every applied field.

#### 6.2.4 Modeling $(E_a^T, t)$ vs. $(\Delta n_s, d, a)$

From the previous section, we found that the relation between  $n_s$ ,  $d$ , and  $a$  can be modeled accurately using the dispersion curves. However, a deterministic relation between the applied field and time duration  $(E_a^T, t)$  and the refractive index change, guide depth and profile parameter  $(\Delta n_s, d, a)$  needs to be established so that necessary waveguide parameters can be specified from arbitrary fabrication conditions.

As described earlier, the effective depth  $d$  can be expressed by (6.7) for each chosen applied field. The validity of this relation can be verified by plotting  $d$  against  $t$  for all the measured guides (TE and TM), as shown in Figs. 6.3 (a) and (b). The constant depth values  $K_o$  and the coefficient  $F_c$  are obtained by using a least square fit [38] for every  $E_a^T$ . We note that the value  $K_o$  arises from the extra ten minutes of cooling in our process. In Fig. 6.4 (a) and (b), these coefficients are plotted against

$E_a^T$  with the help of linear regression yielding the constant  $A_1(TE) = 21.33 \mu\text{m}^2/V$  min. and  $A_1(TM) = 20.52 \mu\text{m}^2/V$  min.

Thus, to characterize a planar waveguide accurately, given fabrication conditions  $(E_a, t)$ , its guide depth can be determined using (6.2) with the coefficient  $F_c$  as obtained from (6.3). These coefficients and the refractive index change for every applied field are summarized in Tables 6.7 and 6.8. The effective indices  $N_c$  can be obtained by using the dispersion curves generated by the WKB relation involving the parameters  $(n_s, d, a)$ .

### 6.2.5 Number of guided modes

The number of guided modes in a planar waveguide with a modified Fermi profile  $f(x)$  can be predicted accurately by using (6.4). Letting  $\xi = x/d$  and the dummy variable  $u = \xi - 1$ , then the integral term of (6.5) reduces to

$$\int_{-1}^{\infty} \frac{du}{\sqrt{1 - \exp(-d/a) + \exp(du/a)}}.$$

This integral can be evaluated from a convenient table of integrals [70]

$$= \frac{a}{d\sqrt{1 - \exp(-d/a)}} \ln \left\{ \frac{\sqrt{1 - \exp(-d/a) + \exp(du/a)} - \sqrt{1 - \exp(-d/a)}}{\sqrt{1 - \exp(-d/a) + \exp(du/a)} + \sqrt{1 - \exp(-d/a)}} \right\} \Bigg|_{-1}^{\infty}$$

and upon using l'Hopital's rule, we obtain

$$\int_0^{\infty} f(x)dx = \frac{a}{\sqrt{1 - \exp(-d/a)}} \ln \left\{ \frac{1 + \sqrt{1 - \exp(-d/a)}}{1 - \sqrt{1 - \exp(-d/a)}} \right\}. \quad (6.8)$$

Hence, using (6.5) and (6.8), the number of guided modes can be determined by taking the next largest integer of the following expression

$$\frac{2a\sqrt{2n_b\Delta n_s}}{\lambda_0\sqrt{1 - \exp(-d/a)}} \ln \left[ \frac{1 + \sqrt{1 - \exp(-d/a)}}{1 - \sqrt{1 - \exp(-d/a)}} \right] - \frac{1}{\pi} \tan^{-1} \left[ \chi \sqrt{\frac{n_b^2 - 1}{n_s^2 - n_b^2}} \right] - \frac{1}{4}.$$

This analytical expression is quite useful for the design of single and multimode waveguide devices. To evaluate its accuracy, the number of guided modes predicted by the above expression is compared to the actual number of measured modes in the planar field-assisted waveguides. The comparisons are tabulated in Tables 6.9 and 6.10 and the agreement is excellent

## 6.2.6 Discussion of errors

From the dispersion curves of Fig. 6.2, the agreement between the experimentally measured mode indices and the theoretical curves seems quite good. The discrepancies between theory and experiment was calculated for each of the 153 measured indices and the average of these was found to be:

$$|N_e(\text{meas.}) - N_e(\text{theo.})| = (1.1 \pm 1.2) \times 10^{-4}$$

with the largest single deviation being  $6 \times 10^{-4}$ . In our initial analysis using a step-index profile, these average discrepancies were  $(3.4 \pm 2.9) \times 10^{-4}$  with the largest deviations being of the order of  $1 \times 10^{-3}$ . These large errors suggested that the step model was not suitable for these waveguides. For comparison, a set of TE mode dispersion curves with a modified Fermi function show significant improvement over the step model for  $E_a = 21.1 \text{ V/mm}$  (see Fig. 6.5).

Another key factor in this characterization involves the reproducibility of such waveguides under given fabrication conditions. To evaluate this property, two waveguides were fabricated one week apart under identical fabrication conditions. It was found that the differences in the measured mode indices were within measurement error (see Table 6.11). Although short diffusion times were used, we were able to control the fabrication process quite accurately with the estimated error in the time measurements being 10 to 15 seconds.

## 6.3 Diffusion characteristics

### 6.3.1 Introduction

The diffusion characteristics of field-assisted ion-exchange waveguides can be theoretically modeled by numerical and analytical methods, as discussed in Chapter 2. Experimentally, these characteristics can be determined using electron probe microanalysis [60,67] and scanning electron microscopy [57]. Both have been used successfully to measure  $Ag^+$ -ion concentration in soda-lime glass waveguides. For

the case of  $K^+$  ions, the electron microprobe was used to determine the dopant profile of surface and buried channel waveguides in soda-lime and BK7 glass [9]. In addition, ionic current measurements were performed to calculate the ion mobility. Here, we used a SEM-BSE technique to measure the  $K^+$ -ion profile and studied the ionic current data to determine the value of  $\alpha = 1 - \mu_K/\mu_{Na}$  which is needed for modeling.

### 6.3.2 Determination of $\alpha$

The mobility ratio of the potassium and sodium ions is an important parameter in the numerical modeling of the concentration (refractive index) profile. For the case of purely thermal  $K^+ - Na^+$  in soda-lime glass at a temperature of  $374^\circ C$ , it has been established that the much smaller  $Na^+$  ions have a higher mobility than the  $K^+$  ions yielding a ratio ( $M = \mu_K/\mu_{Na} = D_K/D_{Na}$ ) of 1/500, corresponding to  $\alpha = 0.998$  [31]. We were interested to see whether this was also true for field-assisted waveguides. To determine this ratio experimentally, the equation relating the applied field to the flux density (2.12)

$$J_o = \mu_{Na} c_o E_a^T (1 - \alpha \hat{c}_K) \quad (6.9)$$

was modified to include the total applied field. At time  $t = 0$ ,  $\hat{c}_K(x, 0) = 0$  and hence,

$$J_o(t = 0) = \mu_{Na} c_o E_a^T$$

so that

$$\mu_{Na} = \frac{J_o(t = 0) \times 60 \frac{\mu m^2}{sec}}{c_o E_a^T \text{ Vmin}}$$

with the factor of 60 used to convert from seconds to minutes. Since the initial current flux  $J_o(\text{mole}/\mu m^2/\text{sec})$  and applied field  $E_a(\text{V}/\mu m)$  are known, the only unknown constant is the initial concentration of  $Na^+$  ions in the glass,  $c_o(\text{mole}/\mu m^3)$ . This value can be calculated directly from the chemical composition of the glass. The number of moles of the  $Na^+$  ion contributed by the molecular component

$Na_2O$  is [79]

$$N_{Na} = m_{Na} \times wf_{Na_2O} / W_{Na_2O}$$

where  $m_{Na}$  is the number of  $Na^+$  ions contributed by  $Na_2O$ ,  $wf_{Na_2O}$  is its weight fraction in the glass and  $W_{Na_2O}$  is its molar molecular weight. For soda-lime glass,  $m_{Na} = 2$ ,  $wf_{Na_2O} = 0.1433$  (see Table 5.1),  $W_{Na_2O} = 62.0 \text{ g/mole}$ , and the density is  $2.4667 \text{ g/cm}^3$ . Defining the concentration  $c_o$  as the number of moles per  $\mu\text{m}^3$ , then

$$c_o = \frac{2 \times 0.1433 \times 2.4667 \times 10^{-12}}{62.0} = 1.139 \times 10^{-14} \left( \frac{\text{mole}}{\mu\text{m}^3} \right)$$

with the  $10^{-12}$  factor used to convert from  $\text{cm}^3$  to  $\mu\text{m}^3$ . The mobility  $\mu_{Na}$  was calculated for 14 good samples with the results shown in Table 6.12. The average value of all the samples yields:  $\mu_{Na} = 119.1 \pm 14.3 \mu\text{m}^2/\text{V min}$ .

To calculate  $M$ , one must also know the correlation factor  $f$  (see (2.5)) for soda-lime glass. Doremus reported that  $f = 1$  for soda-lime glass [31], even though there are conflicting results from other researchers [29]. As examples, Ohta [32] reported  $f = 0.3$  for  $K^+$ -ion exchange in soda-lime glass using applied fields and temperatures ranging from  $5.3$  to  $16.7 \text{ V/mm}$  and from  $400$  to  $500^\circ\text{C}$ , respectively. Recently, Miliou [9] reported  $f = 0.1$  for  $90\%$   $K^+$ -ion exchange using  $E_a = 100 \text{ V/mm}$  and  $T = 330^\circ\text{C}$ . In this thesis, we used  $f = 0.2$ , halfway between these results. Hence, using  $\mu_{Na} = eD_{Na}/fkT$ , then the sodium self-diffusion coefficient becomes:

$$D_{Na} = \frac{fkT\mu_{Na}}{e} = 0.6708 \left( \frac{\mu\text{m}^2}{\text{min.}} \right)$$

and with  $D_K = 0.01186 \mu\text{m}^2/\text{min.}$ , at  $T = 385^\circ\text{C}$ ,  $M = 0.0177$ , finally resulting in  $\alpha = 0.991$ . This is in excellent agreement with  $\alpha = 0.998$  discussed earlier. Also, we assumed  $c_l = 0.9$ , as before, resulting in  $\hat{\alpha} = 0.892$ .

### 6.3.3 Ionic current-time variation

The solutions of the concentration profile, discussed in Chapter 2, refer to a constant ionic flux for a constant electric field applied across the sample. However, since  $\alpha \neq$

0, a constant applied electric field will not result in a constant ionic flux. This can be deduced from (6.9). Since the concentration of  $K^+$  ions is increasing with time and  $E_a^T$  is fixed, then the term  $(1 - \alpha \hat{c}_K)$ , which is proportional to the ionic current, is decreasing with time. We have observed this in our experiments with a typical example shown in Fig. 6.6. As stated correctly by Abou-el-Liel [26], a steady-state solution does not exist for this case. However, since the exchange thickness (typically  $3 - 15 \mu m$ ) is very small compared to the total thickness ( $\sim 1 mm$ ), the numerical model may be accurate enough. The accuracy of this model compared to the experimental SEM results is presented in the next section.

### 6.3.4 Concentration profiles

As discussed in Chapter 2, the diffusion depth  $d$  is defined as the  $x$  value at the half-point of the concentration profile, so that

$$d \simeq \nu^* \mu_K E_a^T t$$

is linearly proportional to the diffusion time,  $t$ . From the propagation characteristics in the previous section, we also found that the depth varied linearly with time, as  $d \sim F_e t = A_1 E_a^T t$ . Hence, we deduce that

$$\mu_K = \frac{A_1}{\nu^*}$$

so that for TE modes,  $A_1 = 21.33 \mu m^2/V \text{ min.}$ ,  $\nu^* = 2.495$ , and thus,  $\mu_K = 8.549 \mu m^2/V \text{ min.}$  This mobility value was used to model a field-assisted ion-exchange profile. We have included the effect of the additional ten minutes of cooling at  $T = 379^\circ C$  ( $D_K = 0.01018 \mu m^2/\text{min.}$ ) [11] in the modeling. This was accomplished by using the first exchange concentration as the initial condition with  $E_a^T = E_0 = 1.3 V/mm$ . The normalized boundary conditions remained unchanged.

A surface waveguide was fabricated at ( $E_a = 21.1 V/mm : t = 20 \text{ min.}$ ) with its BSE-SEM signature shown in Fig. 6.7. For comparison, the numerical solution of the ion-exchange equation with scaled SEM data is shown in Fig. 6.8.

Before concluding this chapter, it is worth mentioning that the diffusion depth  $d$  is slightly different for TE and TM modes due to the polarization dependence of  $F_e$ . This was observed by other researchers for the corresponding value of  $D_e$ , in the case of purely thermal  $K^+$ -ion exchange [9,11]. Ideally, these depth values should be equal because the  $K^+$ -ion concentration is assumed to be the same as the index profile. At this point, it is not known if this assumption is fully correct for the  $K^+$  concentration. Further investigation of this polarization-dependence of  $D_e$  and  $F_e$  is needed.

	17	39	41	<i>Wvg.#</i> 37	14	38	29	22
$TE_0$	1.5196	1.5215	1.5217	1.5206	1.5223	1.5230	1.5204	1.5221
$TE_1$	1.5140	1.5169	1.5178	1.5156	1.5192	1.5210	1.5154	1.5190
$TE_2$		1.5125	1.5136		1.5155	1.5181		1.5153
$TE_3$						1.5148		

	15	21	8	<i>Wvg.#</i> 32	33	2	30	5
$TE_0$	1.5232	1.5235	1.5236	1.5222	1.5232	1.5235	1.5227	1.5235
$TE_1$	1.5219	1.5227	1.5229	1.5180	1.5214	1.5225	1.5204	1.5230
$TE_2$	1.5199	1.5213	1.5218	1.5137	1.5189	1.5212	1.5174	1.5224
$TE_3$	1.5176	1.5197	1.5207		1.5163	1.5194	1.5141	1.5214
$TE_4$	1.5149	1.5178	1.5190		1.5131	1.5175		1.5204
$TE_5$	1.5125	1.5156	1.5172			1.5145		1.5191
$TE_6$		1.5133	1.5154			1.5129		1.5176
$TE_7$			1.5133					1.5161
$TE_8$								1.5145
$TE_9$								1.5129

Table 6.1: Measured effective TE mode indices

	17	39	41	<i>Wvg.#</i> 37	14	38	29	22
$TM_0$	1.5214	1.5241	1.5243	1.5228	1.5247	1.5253	1.5224	1.5255
$TM_1$	1.5151	1.5191	1.5200	1.5173	1.5213	1.5229	1.5171	1.5224
$TM_2$		1.5137	1.5155		1.5173	1.5200		1.5183
$TM_3$					1.5132	1.5164		1.5141
$TM_4$						1.5128		

	15	21	8	<i>Wvg.#</i> 32	33	2	30	5
$TM_0$	1.5257	1.5257	1.5258	1.5242	1.5255	1.5260	1.5250	1.5260
$TM_1$	1.5243	1.5248	1.5252	1.5198	1.5240	1.5250	1.5226	1.5255
$TM_2$	1.5222	1.5235	1.5241	1.5150	1.5210	1.5236	1.5194	1.5249
$TM_3$	1.5197	1.5218	1.5228		1.5180	1.5217	1.5159	1.5238
$TM_4$	1.5170	1.5197	1.5212		1.5148	1.5196	1.5125	1.5227
$TM_5$	1.5139	1.5174	1.5195			1.5174		1.5213
$TM_6$		1.5149	1.5174			1.5148		1.5198
$TM_7$		1.5125	1.5152			1.5125		1.5182
$TM_8$			1.5130					1.5164
$TM_9$								1.5144
$TM_{10}$								1.5129

Table 6.2: Measured effective TM mode indices

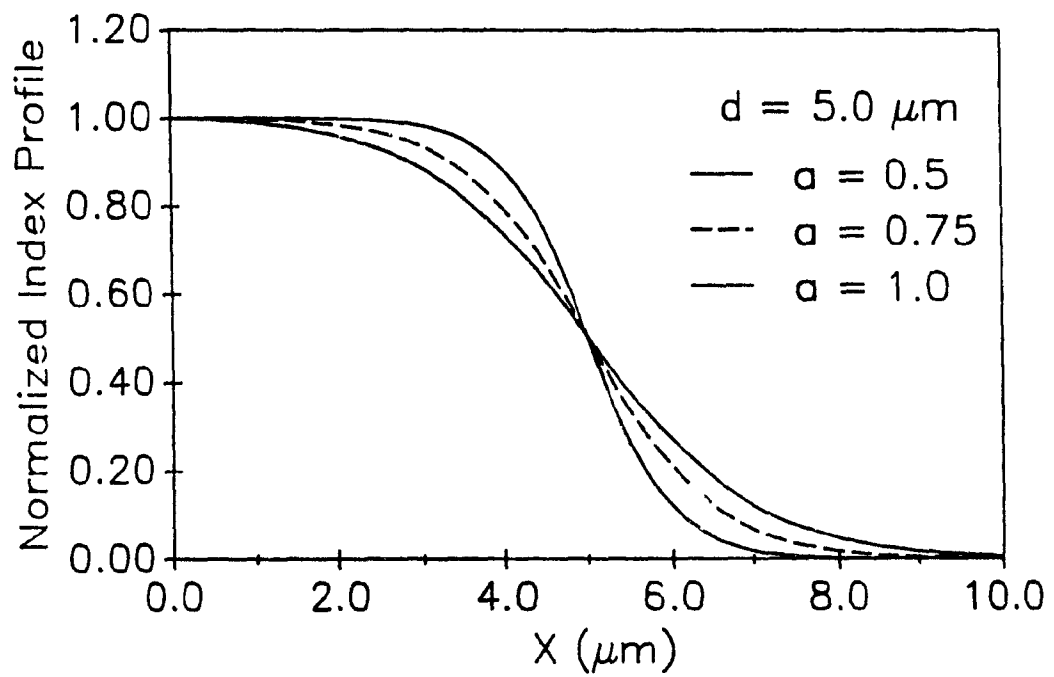


Figure 6.1: Dependence of the shape of the modified Fermi profile on  $a$

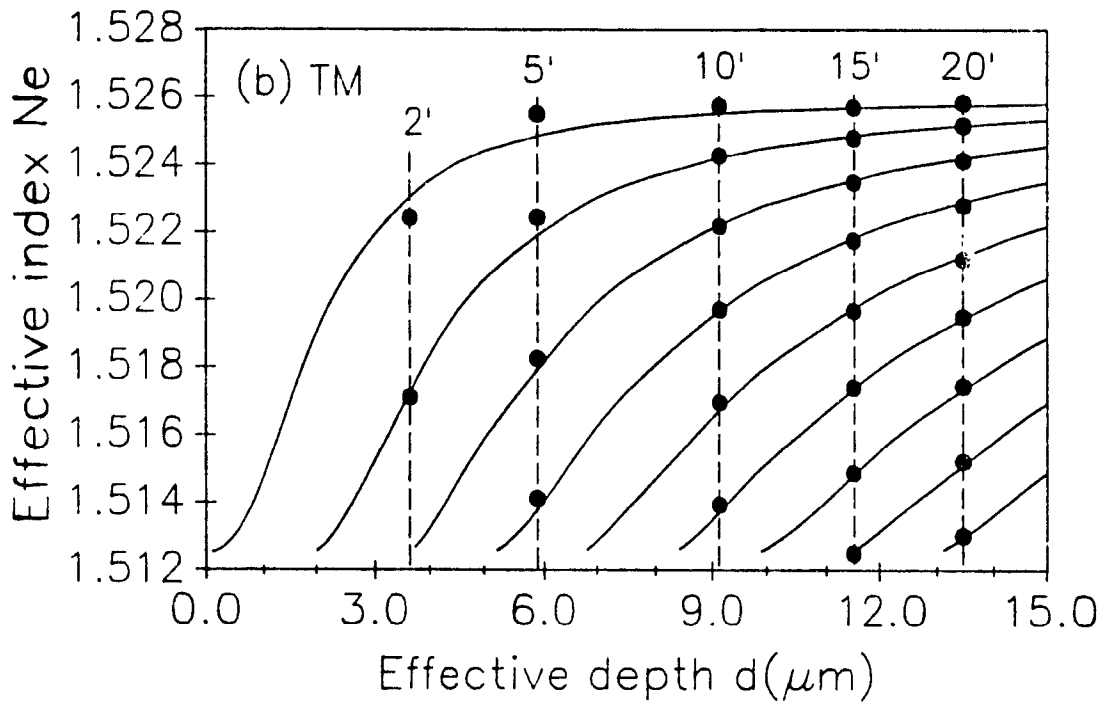
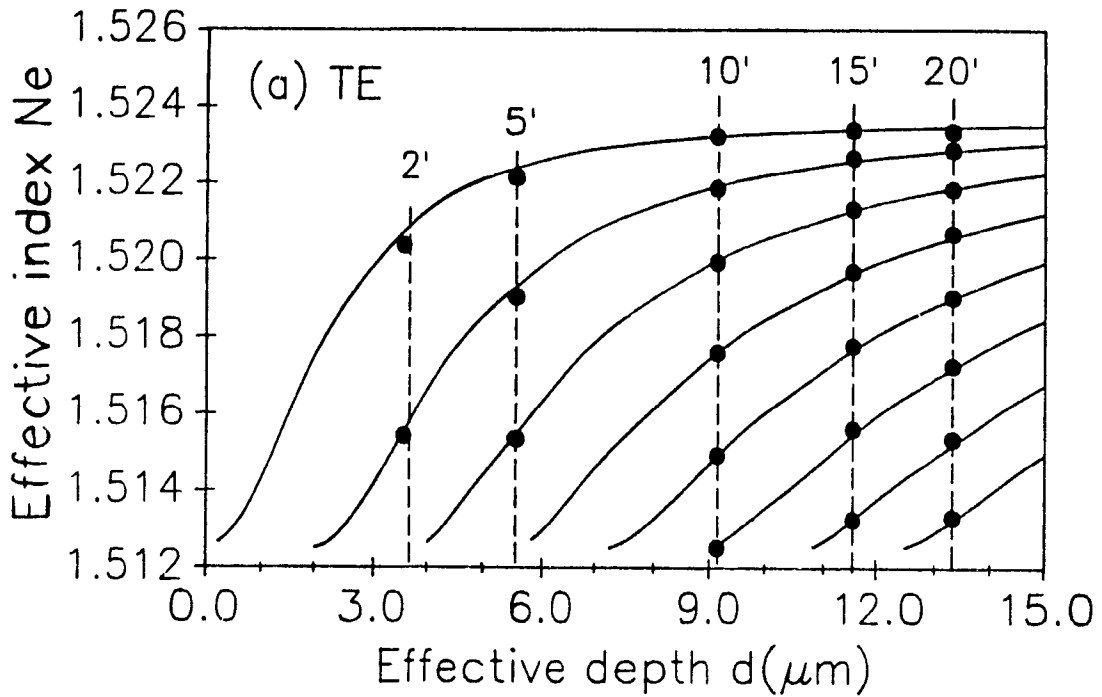


Figure 6.2: Theoretical dispersion curves (modified Fermi profile) compared with measured mode indices for waveguides prepared at  $E_a = 21.1 \text{ V/mm}$  (diffusion time in minutes) (a) TE modes (b) TM modes

<i>Wvg.#</i>	$E_a$ (V/mm)	<i>t</i> (min)	<i>d</i> ( $\mu m$ )	$n_s$	<i>a</i> ( $\mu m$ )
17	5.3	10	3.03	1.5233	0.60
39		15	4.16	1.5233	0.43
41		20	4.72	1.5232	0.61
37	10.6	5	3.72	1.5238	0.66
14		10	5.56	1.5237	0.76
38		15	7.06	1.5238	0.69
29	21.1	2	3.55	1.5234	0.75
22		5	5.54	1.5235	0.76
15		10	9.15	1.5235	0.57
21		15	11.56	1.5237	0.63
8		20	13.31	1.5237	0.67
32	32.1	2	4.54	1.5240	0.64
33		5	8.00	1.5235	0.50
2		10	11.08	1.5237	0.66
30	52.1	2	6.74	1.5235	0.68
5		10	16.38	1.5236	0.79

Table 6.3: Calculated TE mode modified Fermi profile parameters

<i>Wvg.#</i>	$E_a$ (V/mm)	<i>t</i> (min)	<i>d</i> ( $\mu m$ )	$n_s$	<i>a</i> ( $\mu m$ )
17	5.3	10	2.97	1.5254	0.64
39		15	4.10	1.5265	0.58
41		20	4.74	1.5261	0.70
37	10.6	5	3.72	1.5255	0.57
14		10	5.61	1.5258	0.55
38		15	7.05	1.5258	0.51
29	21.1	2	3.62	1.5260	0.75
22		5	5.88	1.5263	0.48
15		10	9.14	1.5260	0.65
21		15	11.51	1.5258	0.50
8		20	13.45	1.5259	0.58
32	32.1	2	4.60	1.5261	0.66
33		5	7.90	1.5264	0.80
2		10	11.29	1.5260	0.53
30	52.1	2	6.87	1.5255	0.47
5		10	16.17	1.5261	0.85

Table 6.4: Calculated TM mode modified Fermi profile parameters

<i>Wvg.#</i>	$E_a$ (V/mm)	<i>t</i> (min)	<i>d</i> ( $\mu m$ )	$n_f$	$\Delta n_f$ ( $\times 10^{-3}$ )
17	5.3	10	3.3	1.5217	$9.8 \pm 0.8$
39		15	4.4	1.5223	
41		20	4.8	1.5224	
37	10.6	5	3.6	1.5223	$10.6 \pm 0.6$
14		10	5.4	1.5229	
38		15	6.9	1.5233	
29	21.1	2	3.7	1.5221	$10.8 \pm 0.6$
22		5	5.4	1.5228	
15		10	9.2	1.5230	
21		15	11.4	1.5234	
8		20	13.1	1.5236	
32	32.1	2	4.7	1.5229	$10.8 \pm 0.5$
33		5	7.9	1.5231	
2		10	10.9	1.5234	
30	52.1	2	6.7	1.5229	$10.7 \pm 0.5$
5		10	16.3	1.5232	

Table 6.5: Calculated TE mode step profile parameters

<i>Wvg.#</i>	$E_a$ (V/mm)	<i>t</i> (min)	<i>d</i> ( $\mu m$ )	$n_f$	$\Delta n_f$ ( $\times 10^{-3}$ )
17	5.3	10	3.2	1.5236	$12.3 \pm 1.0$
39		15	4.3	1.5251	
41		20	4.8	1.5250	
37	10.6	5	3.6	1.5248	$12.5 \pm 0.9$
14		10	5.7	1.5249	
38		15	7.1	1.5251	
29	21.1	2	3.6	1.5243	$13.0 \pm 0.6$
22		5	5.8	1.5256	
15		10	9.0	1.5255	
21		15	11.5	1.5254	
8		20	13.4	1.5255	
32	32.1	2	4.6	1.5250	$13.0 \pm 0.8$
33		5	7.8	1.5256	
2		10	10.9	1.5255	
30	52.1	2	7.0	1.5248	$13.1 \pm 0.7$
5		10	16.0	1.5257	

Table 6.6: Calculated TM mode step profile parameters

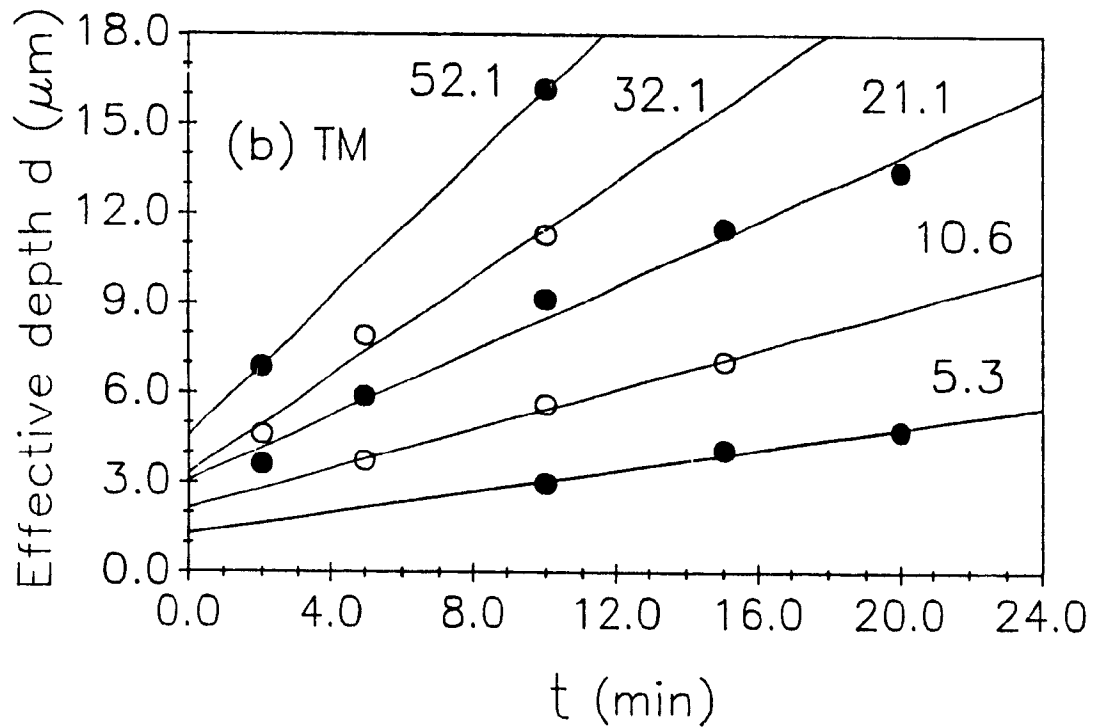
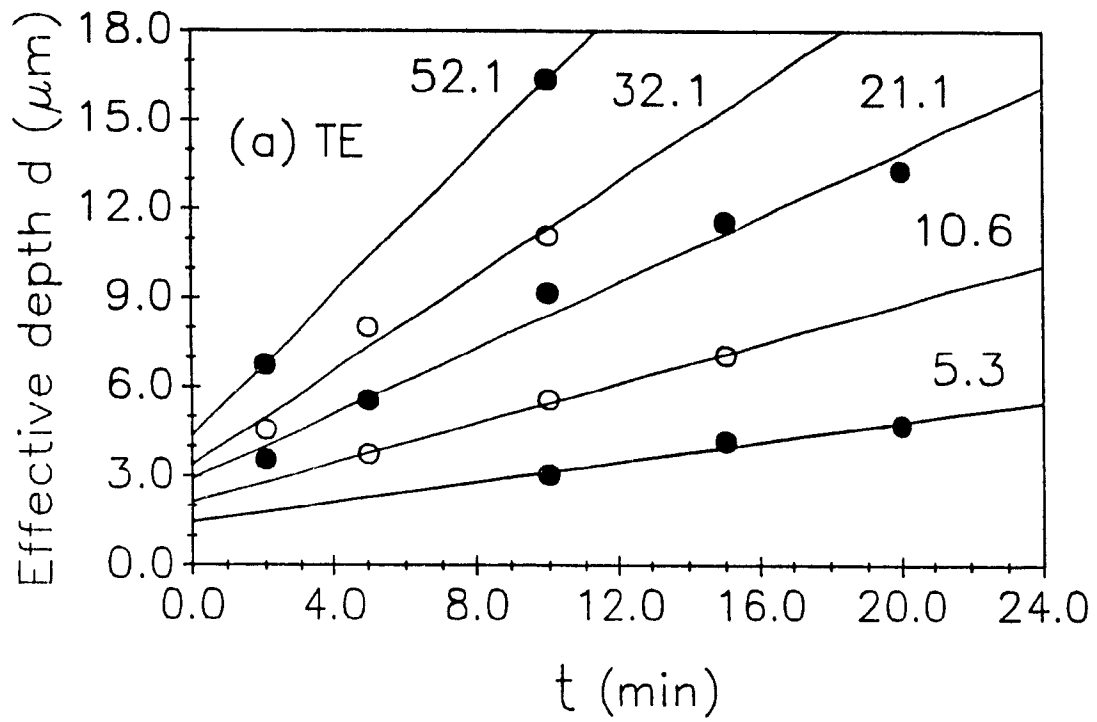


Figure 6.3: Effective guide depths vs. the diffusion time (applied field in  $V/mm$ ) for (a) TE modes (b) TM modes

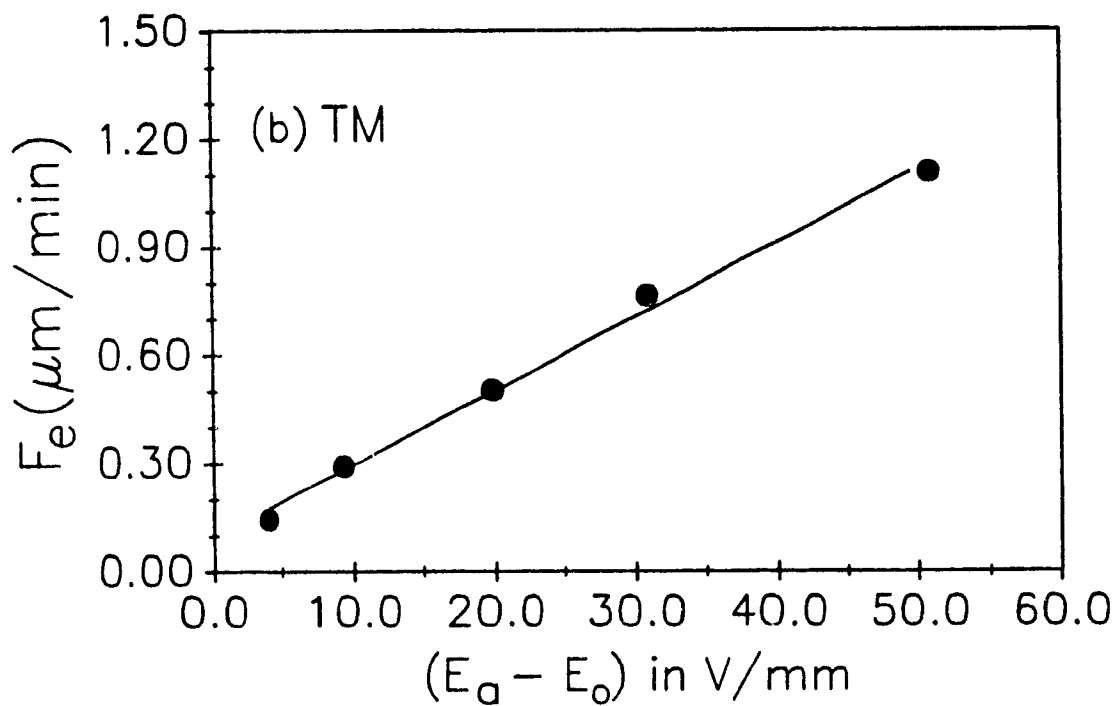
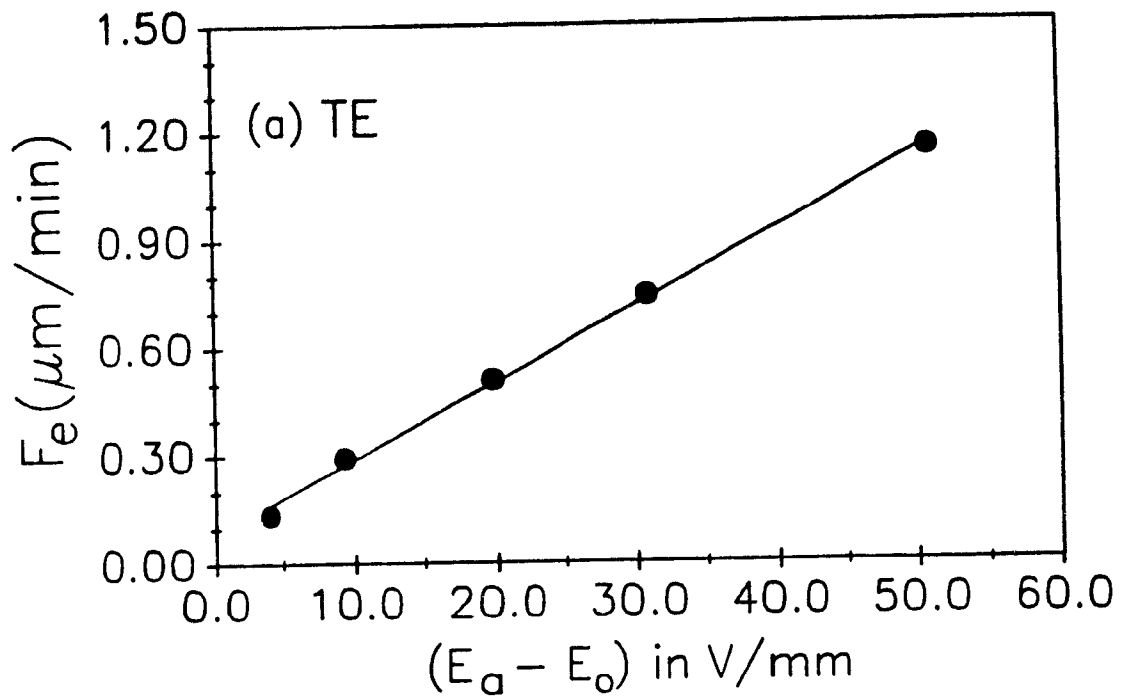


Figure 6.4: Variation of coefficient  $F_e$  with applied field  $E_a$  for (a) TE modes and (b) TM modes

$E_a$ (V/mm)	$\Delta n_s(TE)$ ( $\times 10^{-3}$ )	$\Delta n_s(TM)$ ( $\times 10^{-3}$ )	$a(TE)$ ( $\mu m$ )	$a(TM)$ ( $\mu m$ )
5.3	$10.8 \pm 0.0$	$13.7 \pm 0.3$	0.53	0.64
10.6	$11.2 \pm 0.2$	$13.3 \pm 0.1$	0.69	0.52
21.1	$11.1 \pm 0.1$	$13.4 \pm 0.2$	0.65	0.57
32.1	$11.2 \pm 0.1$	$13.6 \pm 0.2$	0.61	0.60
52.1	$11.1 \pm 0.0$	$13.5 \pm 0.2$	0.78	0.79

Table 6.7: Measured  $\Delta n_s$  and profile parameters for various  $E_a$

$E_a$ (V/mm)	$F_c(TE)$ ( $\mu m/min$ )	$F_c(TM)$ ( $\mu m/min$ )	$K_o(TE)$ ( $\mu m$ )	$K_o(TM)$ ( $\mu m$ )
5.3	0.136	0.144	0.96	0.81
10.6	0.292	0.291	1.74	1.76
21.1	0.509	0.503	2.56	2.72
32.1	0.742	0.765	3.09	3.01
52.1	1.149	1.107	4.08	4.30

Table 6.8: Diffusion coefficients and depth parameters for various applied fields

<i>Wvg.#</i>	$E_a$ (V/mm)	<i>t</i> (min)	<i>m</i> (exp.)	arg.	$m =$ INT(arg.)
17	5.3	10	2	1.45	2
39		15	3	2.10	3
41		20	3	2.42	3
37	10.6	5	2	2.03	3
14		10	3	3.09	4
38		15	4	3.97	4
29	21.1	2	2	1.88	2
22		5	3	3.03	4
15		10	6	5.12	6
21		15	7	6.52	7
8		20	8	7.53	8
32	32.1	2	3	2.44	3
33		5	5	4.45	5
2		10	7	6.24	7
30	52.1	2	4	3.83	4
5		10	10	9.41	10

Table 6.9: Comparison between the calculated and actual number of TE modes

<i>Wvg.#</i>	$E_a$ (V/mm)	<i>t</i> (min)	<i>m</i> (exp.)	arg.	$m =$ INT(arg.)
17	5.3	10	2	1.77	2
39		15	3	2.49	3
41		20	4	2.90	3
37	10.6	5	2	2.09	3
14		10	4	3.29	4
38		15	5	4.20	5
29	21.1	2	2	2.08	3
22		5	4	3.52	4
15		10	6	5.59	6
21		15	8	7.10	8
8		20	9	8.34	9
32	32.1	2	3	2.76	3
33		5	5	4.87	5
2		10	8	7.05	8
30	52.1	2	4	4.36	5
5		10	11	10.30	11

Table 6.10: Comparison between the calculated and actual number of TM modes

Wvg.#15	Wvg.#11	$\Delta (\times 10^{-4})$
1.5231	1.5233	2
1.5218	1.5219	1
1.5199	1.5200	1
1.5175	1.5177	2
1.5149	1.5150	1
1.5125	1.5125	0

Table 6.11: Comparison of two waveguides fabricated under identical conditions

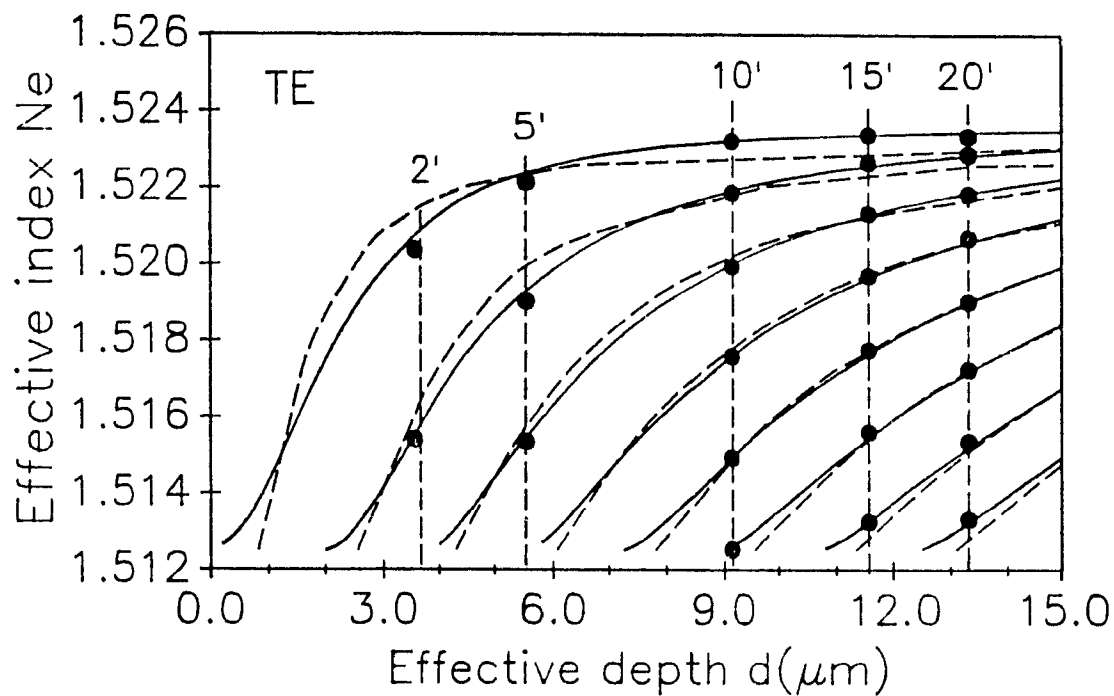


Figure 6.5: Comparison of the theoretical dispersion curves of a modified Fermi profile (solid curve) with the step profile (dashed curve) together with the experimental data of Fig. 6.1(a)

Wvg #	Fabrication condition	$i$ (mA)	Area (mm) <sup>2</sup>	$\mu_{Na}$
5	52.1 V/mm : 10 min.	63.0	659.1	102.7
30	52.1 V/mm : 2 min.	90.5	894.0	108.8
2	32.1 V/mm : 10 min.	45.0	714.0	111.7
33	32.1 V/mm : 5 min.	49.0	792.0	109.7
32	32.1 V/mm : 2 min.	53.0	832.0	112.9
8	21.1 V/mm : 20 min.	31.0	800.0	106.8
21	21.1 V/mm : 15 min.	34.0	816.5	114.8
15	21.1 V/mm : 10 min.	27.0	621.8	119.7
22	21.1 V/mm : 5 min.	32.0	833.5	105.8
29	21.1 V/mm : 2 min.	38.5	840.0	126.4
38	10.6 V/mm : 15 min.	14.7	683.5	126.2
14	10.6 V/mm : 10 min.	21.0	964.3	127.8
41	5.3 V/mm : 20 min.	8.3	765.8	147.4
39	5.3 V/mm : 15 min.	9.3	869.0	146.7

Table 6.12: Mobility measurements and other process parameters

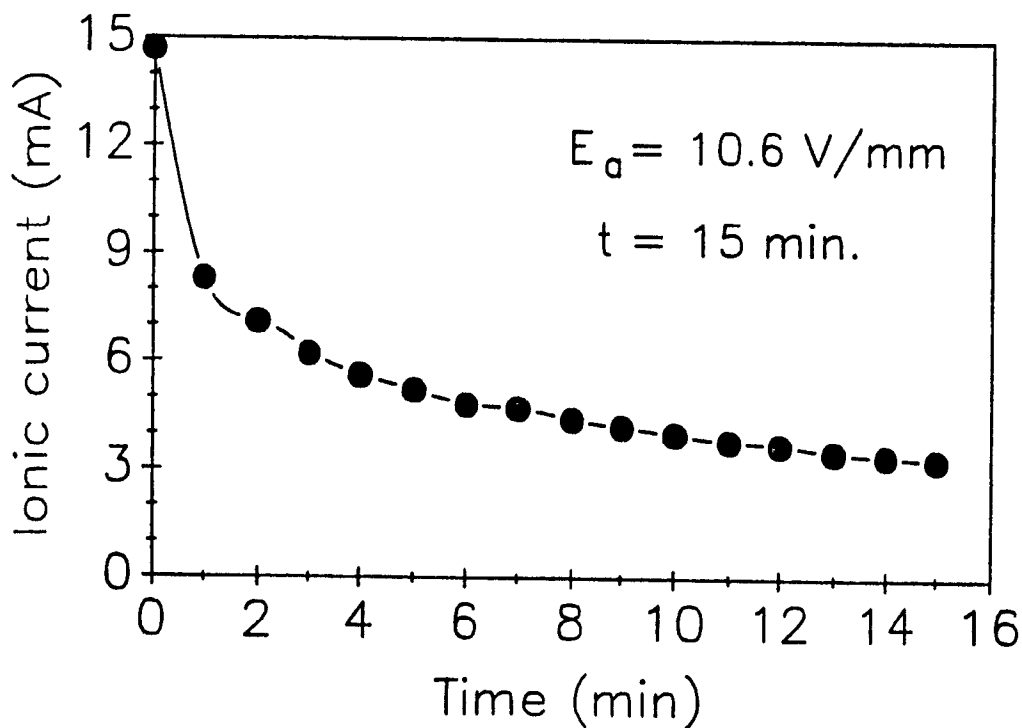


Figure 6.6: Typical example of ionic current-time variation

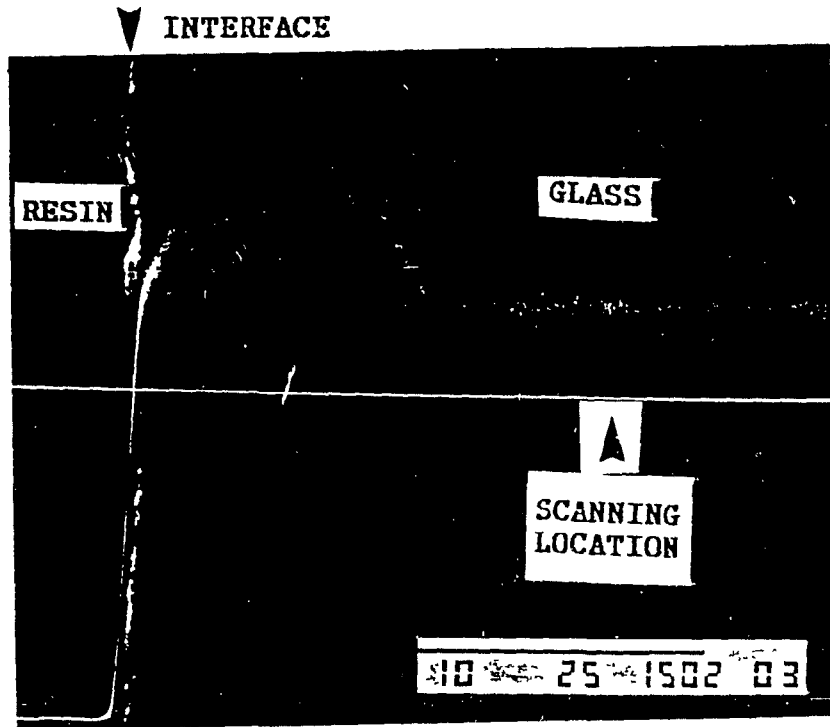


Figure 6.7: SEM photograph of a surface waveguide (3500 $\times$ ) fabricated at  $E_a = 21.1 V/mm$ ,  $t = 20min.$  and  $T = 385^\circ C$

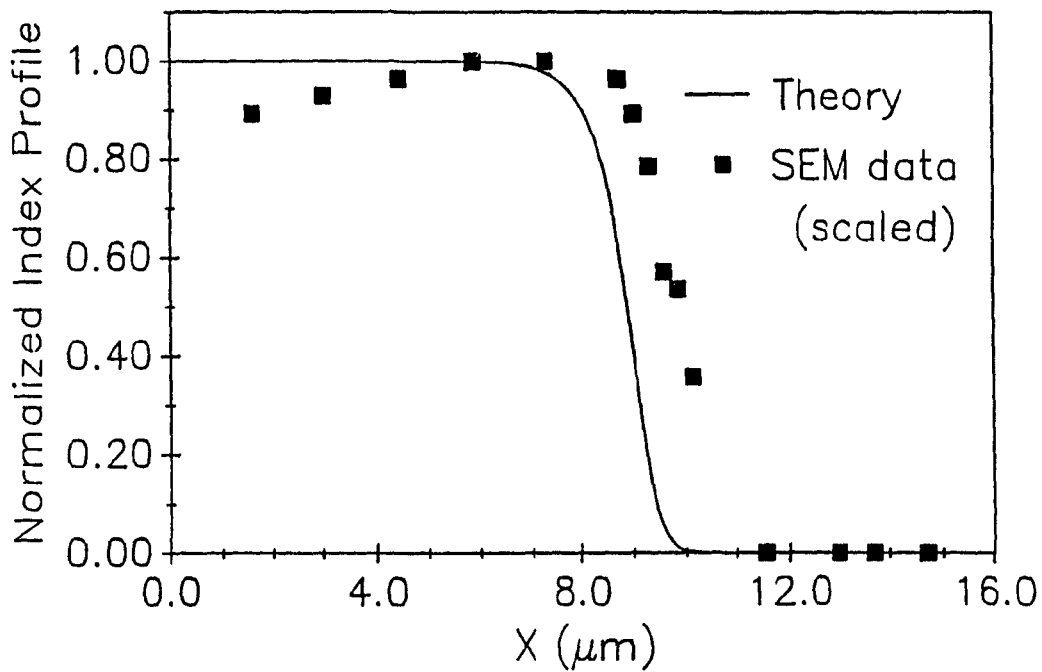


Figure 6.8: Comparison of the numerical solution to the scaled SEM data of the surface waveguide in Fig. 6.5

# Chapter 7

## Discussion and conclusion

The goal of this thesis was to study the  $K^+ - Na^+$  ion-exchange procedure for the fabrication and design of low loss planar glass waveguides. A quantitative correlation of the ion-exchange diffusion properties to the waveguide propagation characteristics was established by theoretical modeling and experimentation. This characterization would provide useful information for the design and fabrication of passive integrated optical devices optimized for efficient coupling with single-mode optical fibers.

The modeling of the fabrication process was realized by numerically solving the non-linear ion-exchange equations, as described in Chapter 2. This modeling provided an accurate description of the dopant concentration profile, which is assumed to be a replica of the refractive index distribution. This profile was then expressed as a simple analytical function for easy implementation in further design stages. The propagation characteristics were determined theoretically, as discussed in Chapter 3. The analytical index profile and subsequent dispersion curves were used in simple formulas to determine the necessary single-mode design parameters. The flowcharts of the characterization methodologies for the purely thermal buried and electric field-assisted surface waveguides are shown in Figs. 7.1 and 7.2, respectively.

For purely thermal buried waveguides, we have demonstrated a novel fabrication procedure. The dopant  $K^+$ -ion profile was numerically modeled and agrees

well with that determined by a BSE-SEM technique. The concentration profile was then fitted by a convenient Rayleigh function whose parameters are dependent on the fabrication conditions such as temperature and diffusion time. This function is then used as the refractive index profile in a simple Runge-Kutta method to solve the Helmholtz equation whose solution provides us with the dispersion characteristics and field profiles of the single-mode waveguides. Measurements of the  $TE_0$  and  $TM_0$  effective mode indices, using a standard prism coupler method, agree well with the calculated dispersion curves. These index measurements begin to equalize as the backdiffusion time increases, indicating a decrease in the birefringence of the waveguides. The modal field widths,  $W_f$ , were calculated for various fabrication conditions and found to increase with  $\sqrt{t_2}$ , indicating a broadening of the guided field. Furthermore, the propagation losses of the buried waveguides were measured and were found to increase with an increasing  $t_2$ . Finally, measured propagation losses were found to increase with increasing backdiffusion time, but, they remained low ( $< 1.0 \text{ dB/cm}$ ) for short diffusion times (less than 20 minutes) at the wavelength  $\lambda_0 = 0.633 \mu\text{m}$ . It is believed that these characterization results will provide useful information to design passive single-mode buried  $K^+$  waveguide devices in optical integrated circuits with improved fiber-waveguide coupling performance and polarization insensitivity.

For the electric field-assisted surface waveguides, we have established simple formulas for the depth and the effective diffusion coefficient of planar optical waveguides fabricated by an electric field-assisted  $K^+$ -ion exchange process. We have verified the linear relation between the diffusion depth and time and between the field-dependent diffusion coefficient and applied electric field. These are consistent with the existing theoretical treatment of electromigration. The surface index change for both polarizations was also determined. Parallel to this, the numerical and analytical modeling of the ion-exchange process led to the accurate prediction of a modified Fermi profile, which shows significant improvement over the step-

index model quoted in the literature. The dopant  $K^+$  profile was correlated to the BSE-SEM data with good agreement. These results are valid for the ranges from about 5 to 50  $V/mm$  and 2 to 20 minutes which, we believe, cover most of the practical conditions under which passive channel waveguide based devices can be fabricated.

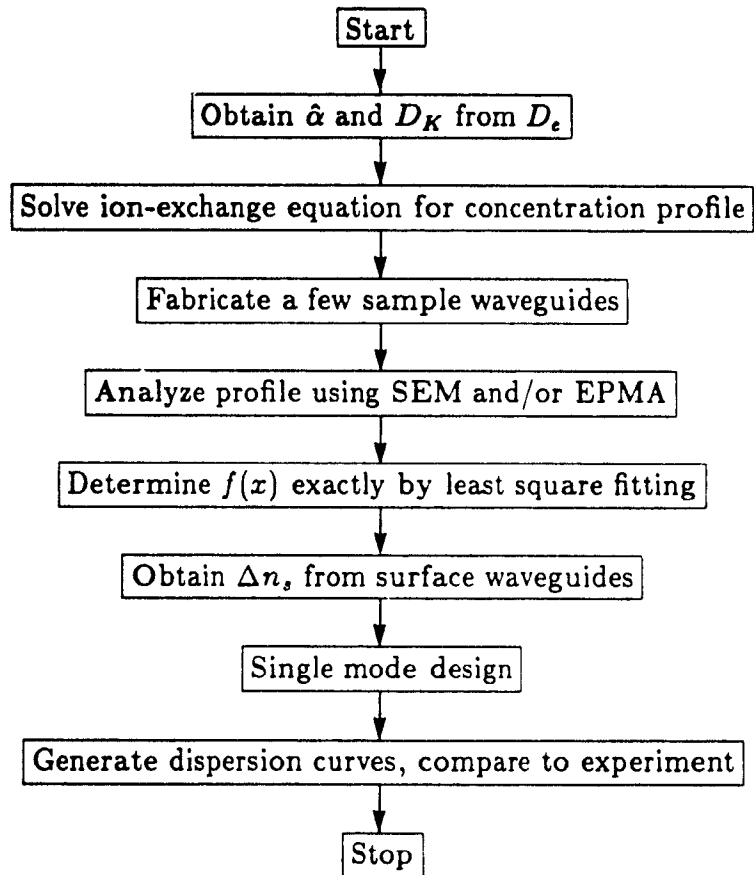


Figure 7.1: A flowchart of the characterization procedure for buried waveguides made by purely thermal migration

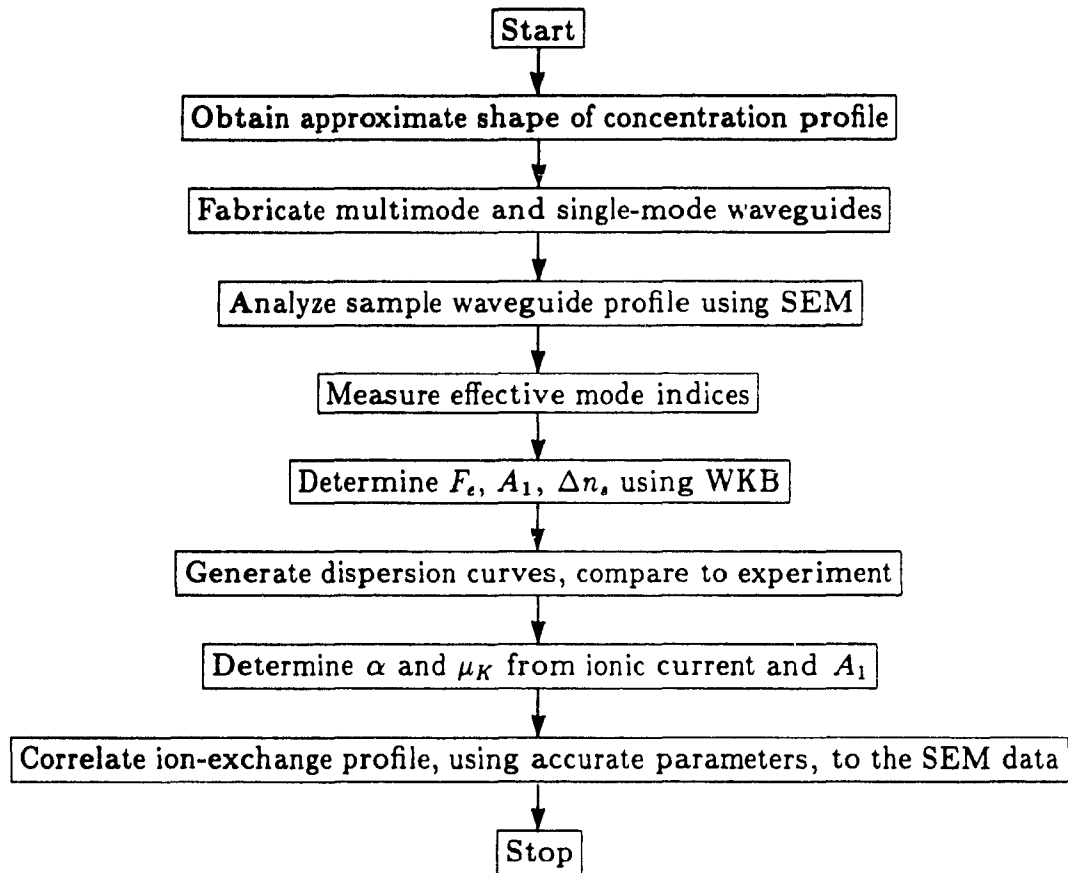


Figure 7.2: A flowchart of the characterization procedure for surface waveguides made by electromigration

# Bibliography

- [1] S.E. Miller, 'Integrated Optics: an introduction', Bell Sys. Tech. Journ., 48, pp. 2059, 1969
- [2] M. Bélanger and G.L. Yip, 'Novel  $Ti : LiNbO_3$  linear mode confinement modulator', Electron. Lett., 22, No. 5, pp. 252-253, 1986
- [3] A. Selvarajan and J.E. Midwinter, 'Photonic switches and switch arrays on  $LiNbO_3$ ', Opt. Quant. Electron., 21, pp. 1-15, 1989
- [4] J. Albert and G. L. Yip, 'Wide single-mode channels and directional couplers by two-step ion-exchange in glass', IEEE J. Lightwave Tech., 6, No. 4, pp. 552-563, 1988
- [5] R.V. Ramaswamy and S. Srivastava, 'Ion-exchange Glass Waveguides: A Review', IEEE J. Lightwave Tech., 6, No. 6, pp. 984-1002, 1988
- [6] J. Guttman, O. Krumpholz, and E. Pfeiffer, 'Optical fiber stripline coupler', Appl. Opt., 14, pp. 1225-1227, 1975
- [7] E.J. Murphy, 'Fiber attachment for guided wave devices', IEEE J. Lightwave Tech., 6, No. 6, pp. 862-871, 1988
- [8] J. Albert and G.L. Yip, 'Insertion loss reduction between single-mode fibers and diffused channel waveguides', Appl. Opt. 27, No. 23, pp. 4837-4843, 1988
- [9] A. Miliou, H. Zhenguang, H.C. Cheng, R. Srivastava, and R.V. Ramaswamy, 'Fiber-Compatible  $K^+ - Na^+$  Ion-Exchanged Channel Waveguides: Fabrica-

- tion and Characterization', IEEE J. Quant. Electron. QE-25, No. 8, pp. 1889-1897, 1989
- [10] T. Findakly and B. Chen, 'Single-mode integrated optical  $1 \times N$  star-coupler', Appl. Phys. Lett. 40, pp. 549-550, 1982
- [11] G.L. Yip and J. Albert, 'Characterization of planar optical waveguides by  $K^+$ -ion exchange in glass', Opt. Lett. 10, No. 3, pp. 151-153, 1985
- [12] J. Albert and G.L. Yip, 'Refractive index profiles of planar waveguides made by ion-exchange in glass', Appl. Opt. 24, No. 22, pp. 3692-3693, 1985
- [13] J. Albert and G.L. Yip, 'Stress-induced index change for  $K^+ - Na^+$  ion exchange in glass', Elect. Lett., 23, No. 14, pp. 737-738, 1987
- [14] J.E. Gortych and D.G. Hall, 'Fabrication of planar optical waveguides by  $K^+$ -ion exchange in BK7 and Pyrex glass', IEEE J. Quant. Electron., 22, No. 6, pp. 892-895, 1986
- [15] T. Izawa and H. Nakagome, 'Optical waveguide formed by electrically induced migration of ions in glass plates', Appl. Phys. Lett., 21, No. 12, pp. 584-586, 1972
- [16] G.H. Chartier, P. Jaussaud, A.D. De Oliveira, and O. Parriaux, 'Optical waveguides fabricated by electric field controlled ion-exchange in glass', Electron. Lett., 14, No. 5, pp. 132-134, 1978
- [17] M. McCourt, R. Rimet, and C. Nissim, 'Multiplexing characteristics of  $K^+$  and  $Ag^+$  ion-exchanged directional couplers', in Proceedings of the European Fiber-Optic Conference (EFOC/LAN '87), Basel, Switzerland, pp. 111-114, 1987
- [18] P.C. Noutsios and G.L. Yip, 'Shallow buried waveguides made by purely thermal migration of  $K^+$  ions in glass', Opt. Lett., 15, No. 4, pp. 212-214, 1990

- [19] P.C. Noutsios and G.L. Yip, 'Shallow buried waveguides made by purely thermal migration of  $K^+$  ions in glass', presented at SPIE OE/FIBERS '89 Integrated Optics and Optoelectronics, Vol. 1177, pp. 2-6, Boston, Mass., Sept. 1989
- [20] P.C. Noutsios and G.L. Yip, 'Theoretical model and experimental characterization of buried, single-mode waveguides in glass', in Technical Digest on Integrated Photonics Research 1990, Hilton Head, S.C., Vol. 5, pp. 13, 1990
- [21] G.L. Yip, P.C. Noutsios, and K. Kishioka, 'Characteristics of optical waveguides made by electric-field-assisted  $K^+$ -ion exchange', Opt. Lett., 15, No. 14, pp. 789-791, 1990
- [22] P.C. Noutsios, G.L. Yip, and K. Kishioka, 'Propagation and diffusion characteristics of optical waveguides made by electric field-assisted  $K^+$ -ion exchange in glass', to be presented at SPIE OE/FIBERS '90 Integrated Optics and Optoelectronics, Vol. 1374, San Jose, Calif., Sept. 16-21 1990
- [23] R.H. Doremus, *Glass Science*, Wiley, New York, 1973
- [24] E.B. Shand, *Glass Engineering Handbook*, McGraw-Hill, New York, 2nd ed., 1958
- [25] H. Rawson, 'Glass and its history of service', IEE Proc. 135, No. 6A, pp. 325-330, 1988
- [26] M. Abou-el-Liel, A.R. Cooper, 'Analysis of Field-Assisted Binary Ion Exchange', Journ. of Amer. Cer. Soc., 62, No. 7, pp. 390-395, 1979
- [27] D.R. Uhlmann and N. J. Kreidl ed , *Glass: Science and Technology* Vol. 5 *Elasticity and Strength in Glasses*, Academic Press, New York, 1980

- [28] J. Albert, 'Characterizations and Design of Planar Optical Waveguides and Directional Couplers by Two-step  $K^+ - Na^+$  Ion-Exchange in Glass', Ph.D. Thesis, McGill University, Montreal, Quebec, Canada, Oct. 1987
- [29] R. Terai and R. Hayami, 'Ionic diffusion in glasses', *Journ. Noncryst. Solids*, 18, pp. 217-230, 1975.
- [30] M. Abou-el-Liel and F. Leonberger, 'Model for ion-exchanged waveguides in glass', *J. Amer. Cer. Soc.* 71, No. 6, pp. 497-502, 1988
- [31] R.H. Doremus, *Ion exchange in glasses* in *Ion-Exchange*, vol. 2, J. A. Marinsky, Ed. New York. Dekker, 1969
- [32] H. Ohta and M. Hara, *Yogyo-Kyokai-Shi* 78 (1970) 158 'Ion Exchange in Sheet Glass by Electrolysis,' *Asahi Garasu Kenkyu Hokoku* (Reports of Res.Lab. Asahi Glass Co. Ltd.), 20, No. 1, pp. 15-32, 1970
- [33] J. Crank, *The Mathematics of Diffusion*, 2nd. ed., Clarendon Press, London, 1975
- [34] V.E. Wood, 'Diffusion profiles in ion-exchanged waveguides', *J. Appl. Phys.* 47, No. 7, pp. 3370, 1976
- [35] R.G. Walker, C.D.W. Wilkinson and J.A.H. Wilkinson, 'Integrated optical waveguiding structures made by silver ion-exchange in glass 1: The propagation characteristics of stripe ion-exchanged waveguides: a theoretical and experimental investigation', *Appl. Opt.*, 22, No 12, pp. 1923-1928, 1983
- [36] W.F. Ames, *Nonlinear Partial Differential Equations in Engineering*, Academic Press, New York, 1965
- [37] A.R. Mitchell, *Computational Methods in Partial Differential Equations*, John Wiley & Sons, 1969

- [38] G.G. Bach, Course notes on Numerical Analysis, Mechanical Engineering Department, McGill University, 1982
- [39] M. Lees, 'A linear three level difference scheme for quasilinear parabolic equations', *Maths. of Comp.* 20, pp. 516-522, 1966
- [40] K.S. Spiegler, C.D. Coryell, 'Electromigration in a Cation-Exchange Resin: II', *J. Phys. Chem.*, 56, pp. 106-113, 1952
- [41] F. Helfferich and M.S. Plesset, 'Ion-exchange kinetics: a nonlinear problem', *J. Chem. Phys.*, 28, No. 1, pp. 418-424, 1957
- [42] R.V. Ramaswamy and S.I. Najafi, 'Planar, buried, ion-exchanged glass waveguides: Diffusion characteristics', *IEEE J. Quant. Electron.*, 22, No. 6, pp. 883-891, 1986
- [43] M.S. Sodha and A.K. Ghatak, *Inhomogeneous Optical Waveguides* New York: Plenum Press, 1977
- [44] D. Marcuse, *Light Transmission Optics*, 2nd ed. New York: Van Nostrand Reinhold, 1982
- [45] H.J. Lilienhof, E. Voges, D. Ritter, and B. Pantschew, 'Field-induced index profiles multimode ion-exchanged strip waveguides', *IEEE J. Quant. Electron.*, 18, No. 11, pp. 1877-1883, 1982
- [46] T. Tamir *Integrated Optics*, Berlin Springer-Verlag, 1975
- [47] G.L. Yip and Y. H. Ahmew, 'Propagation characteristics of radially inhomogeneous optical fiber', *Electron. Lett.*, 10, No. 4, pp. 37-38, 1974
- [48] G.L. Yip and H. H. Yao, 'Numerical study of inhomogeneous optical waveguide problems using predictor-corrector method', *Electron. Lett.*, 17, No. 6, pp. 229-230, 1981

- [49] A. Gedeon, 'Comparison between rigorous theory and WKB analysis of modes in graded-index waveguides', *Opt. Comm.*, 12, No. 3, pp. 329-332, 1974
- [50] A.N. Kaul, S.I. Hosain, and K. Thyagarajan, 'A simple numerical method for studying the propagation characteristics of single-mode graded-index planar optical waveguides', *IEEE Trans. Microwave Theory and Tech.* MTT-34, No. 2, pp. 288-292, 1986
- [51] P.K. Mishra and A. Sharma, 'Analysis of single mode inhomogeneous planar waveguides', *IEEE J. Lightwave Tech.*, 4, No. 2, pp. 204-211, 1986
- [52] M.J. Adams, *An Introduction to Optical Waveguides*, John Wiley & Sons, Chichester, 1981
- [53] H. Nishihara, M. Haruna, T. Suhara, *Optical Integrated Circuits*, New York: McGraw-Hill, 1989.
- [54] L. Ross, H.-J. Lilienhof, and H.W. Holscher, 'Buried waveguides for passive integrated optics by  $Cs^+$ -ion exchange', in *SPIE Proc. Integrated Optical Circuit Engineering III*, 651, pp. 32-34, 1986
- [55] T. Findakly, 'Glass waveguides by ion-exchange: a review', *Opt. Eng.*, 24, No. 2, pp. 244-250, 1985
- [56] S. Urnes, 'Na-K Exchange in Silicate Glasses', *Journ. Amer. Cer. Soc.*, 56, No. 10, pg. 514-519, 1973
- [57] R.K. Lagu and R.V. Ramaswamy, 'Silver ion-exchanged, buried, glass optical waveguides with symmetric index profile', *Appl. Phys. Lett.*, 48, No. 1, pp. 19-20, 1986
- [58] J. Goldstein, D. Newbury, P. Echlin, D. Joy, C. Fiori, and E. Lifschin, *Scanning Electron Microscopy and X-ray Microanalysis*, Plenum Press, 1st ed., New York, 1981

- [59] B.L. Gabriel, *SEM: A User's Manual For Materials Science* (American Society For Metals Press, Metals Park, Ohio) 1985
- [60] G. Stewart, C.A. Miller, P.J.R. Laybourn, C.D W. Wilkinson, and R.M. De LaRue, 'Planar optical waveguides formed by silver-ion migration in glass', *IEEE J. Quant. Electron.*, 13, No. 4, pp. 192-200, 1977
- [61] J.C. Rucklidge, *Electron microprobe instrumentation, A Short Course in Microbeam techniques*, The Mineralogical Association of Canada, Ed. D.G.W. Smith, Edmonton, 1976
- [62] P.K. Tien and R. Ulrich, 'Theory of prism-film coupler and thin-film light guides', *J. Opt. Soc. Amer.*, 60, No. 8, pp. 1007-1015, 1970
- [63] I.P. Kaminow and L.W. Stulz, 'Loss in cleaved  $Ti$ -diffused  $LiNbO_3$  waveguides', *Appl. Phys. Lett.*, 33, No. 1, pp. 62-63, 1978
- [64] Y. Okamura, S. Yoshinaka, and S. Yamamoto, 'Measuring mode propagation losses of integrated optical waveguides: a simple method', *Appl. Opt.*, 22, No. 23, pp. 3892-3894, 1983.
- [65] H.P. Weber, F.A. Dunn and W.N. Leibolt, 'Loss measurements in thin film optical waveguides', *Appl. Opt.*, 12, No. 4, pp. 755-760, 1973
- [66] R.V. Ramaswamy, H.C. Cheng, and R. Srivastava, 'Process optimization of buried  $Ag^+ - Na^+$  ion-exchanged waveguides: theory and experiment', *Appl. Opt.*, 27, No. 9, pp. 1814-1819, 1988
- [67] T.G. Giallorenzi, E.J. West, R. Kirk, R. Ginther, and R.A. Andrews, 'Optical waveguides formed by thermal migration of ions in glass', *Appl. Opt.*, 12, No. 6, pp. 1240-1245, 1973

- [68] M. Seki, H. Hashizume, and R. Sugawara, 'Two-step purely thermal ion-exchange for single-mode waveguide devices in glass', *Electron. Lett.*, 24, No. 20, pp. 1258-1259, 1988
- [69] H. Hashizume, M. Seki, and K. Nakama, 'Polarization-insensitive planar waveguides 1 × 4 branching device with good wavelength flattened characteristics', *Proceedings of OFC'89, WM1*, pp. 90, Houston, Texas, Feb. 1989
- [70] J.J. Tuma *Engineering Mathematics Handbook*, 2nd. ed., McGraw-Hill, 1978
- [71] A. Brandenburg, 'Stress in ion-exchanged glass waveguides', *IEEE/OSA J. Lightwave Tech.*, 4, No. 2, pp. 1580-1593, 1986
- [72] G. Chartier, P. Collier, A. Guez, P. Jaussaud and Y. Won, 'Graded-index surface or buried waveguides by ion-exchange in glass', *Appl. Opt.*, 19, pp. 1092-1095, 1980
- [73] B.G. Pantchev, 'One-step field-assisted ion exchange for fabrication of buried multimode optical strip waveguides', *Electron. Lett.*, 23, No. 22, pp. 1188-1190, 1987
- [74] R. Klein, D. Jestel, H.-J. Lilienhof and E. Voges, 'Reproducible fabrication of integrated optical components by charge controlled ion exchange in glass', in *SPIE Proc. Integrated Optical Circuit Engineering VI*, 993, pp. 7-12, 1988
- [75] N.A. Sanford, K.J. Malone, and D.R. Larson, 'Integrated optic laser fabricated by field-assisted ion-exchange in neodymium-doped soda-lime silicate glass', *Opt. Lett.*, 15, No. 7, pp. 366-368, 1990
- [76] S.N. Houde-Walter and D.T. Moore, 'Gradient-index profile control by field-assisted ion exchange in glass', *Appl. Opt.*, 24, No. 24, pp. 4326-4333, 1985

- [77] J.M. White and P.F. Heidrich, 'Optical waveguide refractive index profiles determined from measurement of mode indices: a simple analysis', *Appl. Opt.*, 15, pp. 151-155, 1976
- [78] T.R. Chen and Z.L. Yang, 'Modes of a planar waveguide with Fermi index profile', *Appl. Opt.*, 24, No. 17, pp. 2809-2812, 1985
- [79] M.L. Huggins, 'The refractive index of silicate glasses as a function of composition', *J. Opt. Soc. Am.*, 30, pp. 495-504, 1940